

NONISOCHRONOUS OSCILLATIONS
IN PIEZOELECTRIC
NANOMECHANICAL RESONATORS

Thesis by

Matthew Matheny

In Partial Fulfillment of the Requirements for the

Degree of

Doctor of Philosophy

CALIFORNIA INSTITUTE OF TECHNOLOGY

Pasadena, California

2012

(Defended February 15, 2012)

© 2012

Matthew Matheny

All Rights Reserved

To my wife and teacher

ACKNOWLEDGEMENTS

Appreciation, first and foremost, goes to my wife, Serena, whose support made this thesis possible. I would also like to thank Chun Man Sit for the encouragement to proceed with my graduate study.

I give warm thanks to my co-conspirators in the nonlinear dynamics subgroup. Special thanks goes to Guillermo Villeneuve for help with experimental planning, device modeling, data fitting, and figure creation. His input was invaluable to the nonlinear dynamics team in the Roukes group. Thanks also go to Philip Feng and Rassul Karabalin for teaching me the “nano” ropes of fabrication and detection of small signals. I would especially like to thank Dr. Karabalin for his excellent management. Some of the data from chapters 2 and 4 were taken with Dr. Villeneuve and Dr. Karabalin. Thanks goes to the halftime member of the fabrication team for the nonlinear dynamics subgroup, Derrick Chi, who helped with the ebeam lithography toward the end of the thesis work.

Important dialogues were conducted with Junho Suh, Trevor Fowler, Akshay Naik, Selim Hanay, and Dalziel Wilson.

I would like to extend gratitude to the rest of my Roukes group colleagues for tolerating my equipment borrowing and generally acerbic disposition during group meetings.

Much of the theoretical work in this thesis was done in collaboration with John Sader (chapter 3), Michael Cross (chapter 5), Eyal Kenig (chapter 4), Guillermo Villeneuve (chapter 2), and Matt Grau (chapter 5), so appreciation is in order.

Finally, I would like to thank my advisor Professor Michael Roukes for providing me with the encouragement and support to pursue the less trodden path.

ABSTRACT

Nanoelectromechanical systems (NEMS) have proven an excellent test bed for exploring nonlinear dynamics due to short decay times, weak nonlinearities, and large quality factors. In contrast to previous research in nonlinear dynamics involving driven or *phase fixed* NEMS, where time is referenced by an external source, we describe phenomena classified by *phase free* phenomena. Here we describe NEMS embedded into feedback oscillators with weak nonlinearities.

We make measurements of this mechanical nonlinearity by developing a transduction scheme, the piezoelectric/piezoresistive (PZE/PZR) transduction, which emphasizes the detector dynamic range over absolute sensitivity. Using these measurements, projections on quantum nondemolition schemes involving the mechanical nonlinearity as a detector are made. These measurements also are important for understanding the detection limits of NEMS sensor technology, which uses a mechanical resonator as a frequency reference in a phase locked loop (PLL).

This work identifies ways to reduce noise within ‘nonlinear’ feedback oscillators, and these results have implications for sensing systems using nonlinear mechanical resonators embedded in PLLs. Since the mechanical nonlinearity of PZE/PZR resonators can be accurately calibrated, we make predictions for the behavior of these dynamical systems based on the given mechanical and electrical parameters. We show, theoretically, that local isochronicity above critical nonlinear amplitudes can create special operating points in feedback oscillators at which parametric fluctuations may cause less phase noise in the oscillator than in feedback oscillators driven below critical amplitudes. For these predictions, we present data that show quantitative agreement for the amplitude and frequency, and qualitative agreement for the phase noise.

Finally, we show synchronization, assisted by nonisochronicity, between two feedback NEMS oscillators. We develop a general theoretical framework for two saturated feedback oscillators which use resonators with nonlinear stiffness. In the limit of small coupling, we show that the system obeys the Adler equation with analytical predictions for the oscillators' individual amplitudes and net frequency difference. We develop an experiment in which the three important parameters of the system (detuning, nonisochronicity, and coupling) can be tuned, and show data that agrees with the predictions for a large range of coupling. We include data on phase slipping between two oscillators in which the aperiodic frequency difference is clearly observed. Finally, we present data on phase noise in synchronized oscillators.

TABLE OF CONTENTS

List of Figures	viii
Chapter 1 Introduction	1
1.1 Background and Motivation	2
1.2 Definition of an Oscillator	3
1.3 Feedback Oscillators	5
1.4 Phase Noise in Oscillators	8
1.5 Isochrones and AM-PM conversion	9
1.6 Thesis Layout.....	12
Bibliography.....	13
Chapter 2 Piezoelectric and Piezoresistive Transduction	16
2.1 Introduction.....	17
2.2 Requirements for Nonlinear NEMS Studies	17
2.3 Derivation of Piezoelectric Actuation Efficiency	20
2.4 Choice of Piezoelectric Material.....	27
2.5 Piezoelectric Actuation Experimental Results	28
2.6 Derivation of Piezoresistive Detection Efficiency	32
2.7 Calibration of Piezoresistive Detection Efficiency	39
2.8 Piezoelectric-Piezoresistive Motional Resistance	42
2.9 All Piezoelectric Transduction Theory	47
2.10 All Piezoelectric Transduction Results	50
2.11 Choosing Piezoresistive Detection.....	53
2.12 Future Work.....	53
Bibliography.....	54

Chapter 3 Nonlinear Mechanics.....	59
3.1 Introduction.....	60
3.2 Analytical Prediction for Nonlinear Stiffness in a Doubly Clamped Beam.....	60
3.3 Transduction Nonlinearity	63
3.4 Measurement of the Nonlinear Stiffness Tensor.....	69
3.5 Quantum Nondemolition Predictions.....	72
3.6 Nonlinearity Tuning through Beam Deflection	74
3.7 Future Work.....	79
Bibliography.....	80
Chapter 4 Feedback Oscillators	83
4.1 Introduction.....	84
4.2 Oscillators with Nonlinear Stiffness	85
4.3 Feedback Oscillators with the Rapp Saturation Model.....	87
4.4 Experimental Validation of Feedback Loop Modeling.....	89
4.5 Unsaturated and Saturated Oscillators	95
4.6 Noise in Saturated Oscillators.....	96
4.7 Isochrones and Noise Diffusion Constants	101
4.8 Phase Noise Due to Fluctuating Phase Shift	105
4.9 Phase Noise Due to Thermomechanical Noise	106
4.10 Optimizing Phase Noise for Both Phase Shift and Thermomechanical Fluctuations	107
4.11 Experimental Results for Noise in a Saturated Oscillator.....	111
4.12 Future Work.....	113
Bibliography.....	115
Chapter 5 Synchronization.....	118
5.1 Introduction.....	119
5.2 Feedback Oscillators with Multiple Feedback Loops	121

5.3	Synchronization Equations for Two Oscillators	122
5.4	Synchronization in the Limit of Small Coupling	125
5.5	Amplitude Limitations	131
5.6	Simulations of Synchronization with Large Coupling	134
5.7	Realization of Two Coupled Oscillators	136
5.8	Calibration of Parameters	139
5.9	Experimental Resonator Parameters	145
5.10	Frequency Sweeps in the Limit of Weak Coupling	146
5.11	Phase Slipping on the Border of Synchronization	150
5.12	Frequency Sweeps at Larger Coupling	152
5.13	Synchronized States at Fixed Detuning	155
5.14	Phase Noise in Two Synchronized Oscillators	156
5.15	Future Work.....	162
	Bibliography.....	164
Appendix I Secular Perturbation Theory		167
Appendix II Fabrication Methods		172
AI.1	Introduction.....	172
AI.2	Piezoelectric Wafer Stacks	172
AI.3	Fabrication of Piezoelectric AlN.....	173

LIST OF FIGURES

Figure 1.1: Feedback oscillator diagram	5
Figure 1.2: Simulation of the van der Pol oscillator	7
Figure 1.3: Isochrones for different values of nonisochrony	11
Figure 2.1: Piezoelectric actuation	21
Figure 2.2: Calibration of the piezoelectric constant	31
Figure 2.3: Deflection of a beam near the clamp	35
Figure 2.4: Mode shapes and piezoresistive detection efficiencies for the first three modes of a cantilever and doubly clamped beam	38
Figure 2.5: Thermomechanical noise from a 10 μ m x 0.4 μ m PZE/PZR beam	40
Figure 2.6: Prediction of the thermomechanical noise in a PZE/PZR beam	42
Figure 2.7: Circuit setup and electromechanical model for a piezoelectric resonator	44
Figure 2.8: Different types of piezoelectric/piezoresistive resonators made from Mo/AlN stacks	45
Figure 2.9: The effect of piezoresistive bias on a beam.	46
Figure 2.10: All-piezoelectric transduction.	51
Figure 3.1: Noise paradigm for nonlinear measurement	64
Figure 3.2: Comparison of amplitude sweeps of optical detection and piezoresistive detection	65
Figure 3.3: Dynamic range of the beam	67
Figure 3.4: Measurement of the nonlinear stiffness coefficients.	71
Figure 3.5: Diagram of the softening effect due to a static deflection	75
Figure 3.6: Two 30 μ m long beams showing static deflection	76
Figure 3.7: Temperature dependence on applied piezoresistive bias voltage	77
Figure 3.8: Nonlinearity changes under changing temperature and deflection	78
Figure 3.9: Frequency amplitude sweeps for three different values of temperature	79
Figure 4.1: Amplifier saturation function using Rapp formula	88

Figure 4.2: Feedback oscillator diagram using piezoelectric/piezoresistive device.	90
Figure 4.3: Saturation curve for a given oscillator feedback function.....	91
Figure 4.4: Raw data for the frequency of oscillation versus phase shifter voltage.	93
Figure 4.5: Measured amplitude and frequency against the predicted results	94
Figure 4.6: Phase space for the saturated oscillator.....	105
Figure 4.7: Isochrones for two different phase shift values.....	107
Figure 4.8: Isochronous and Greywall-Yurke points in frequency-phase shift-amplitude space	110
Figure 4.9: Simulations of the phase noise against loop phase shift for different values of saturation	111
Figure 4.10: Experimental results for the phase noise as a function of the feedback phase for the saturated oscillator	112
Figure 5.1: Approximate dynamics of two synchronized oscillators in the limit of small couplin	128
Figure 5.2: Fixed point analysis of the small coupling dynamics.....	129
Figure 5.3: Amplitude space for the two oscillators.....	133
Figure 5.4: Eigenvalues for the Jacobian of the synchronization equations	133
Figure 5.5: Simulation of the frequency difference of the two oscillators as detuning is swept.	135
Figure 5.6: Detuning sweep with a resonator Q difference of 10%	136
Figure 5.7: Experimental setup for oscillator synchronization using a feedback loop.....	138
Figure 5.8: Amplitude for nearly isochronous oscillator as loop phase being tuned	140
Figure 5.9: Raw data of the detuning sweeps	142
Figure 5.10: Coupling calibration curve for the two oscillators	144
Figure 5.11: Frequency difference in the low coupling limit from a detuning sweep.....	147
Figure 5.12: The amplitudes of the two oscillators in the low coupling limit from a detuning sweep.....	149
Figure 5.13: Phase slip data and associated Adler curve.....	152
Figure 5.14: Frequency difference and amplitude of one oscillator in the limit of large coupling.....	153
Figure 5.15: Synchronization region in detuning-coupling space.....	155
Figure 5.16: Synchronization region in coupling-shear space.....	156
Figure 5.17: Topology for the phase variables of the two oscillators.....	159

Figure 5.18: Phase noise plot for oscillator A at three different values of coupling. 160

Figure 5.19: Phase noise at 1kHz offset as a function of coupling for both oscillators. 162

Chapter 1

Introduction

In this chapter, we introduce the basic concepts and conventions for the thesis. These will include background and motivation for doing experiments in the nonlinear dynamics of oscillators, by themselves and coupled together. We introduce the concept of isochrones and how they are related to amplitude-modulation to phase-modulation (AM-PM) conversion in oscillators.

1.1 Background and Motivation

The modern history of mechanical timekeeping can be traced from gravity pendula, to spring-driven mechanical clocks, to quartz-crystal oscillators [1], and finally, to present day MEMS oscillators. There are many figures of merit for mechanical oscillators that have improved through the last century (such as power consumption, cost, temperature stability, *et cetera*), but of special importance are phase noise and size [2]. Miniaturization is especially important for modern mobile applications [3, 4]. This miniaturization includes not only the resonant element, but the energy source. Oscillators must consist of a resonator and energy source (amplifier, spring, gravity, *et cetera*). This can be traced to the fact that attracting limit cycles cannot exist in conservative systems [5] (more on limit cycles in section 1.3). As the resonating elements have shrunk, so have the energy sources (and thus power consumption).

However, a completely different paradigm for timekeeping arose which utilizes an even smaller object, the atom. Timekeeping has been revolutionized by atomic clocks, which have recently shown total frequency uncertainty at levels of 10^{-17} [6]. Also, in order to reduce size and power, within the last decade, great efforts have been expended to push towards *chip scale atomic clocks* [7] (CSACs). For chip scale atomic clocks, a separate oscillator [8] is typically locked to the transition frequency of an atom, usually rubidium, so that long term drifts in a VCO (voltage controlled oscillator) are nulled by the atomic standard. This essentially means that short term phase noise is set by the VCO and long term phase noise by the atomic standard. In other words, point-to-point ‘frequency sources’ are still constructed using electromechanical resonators. Any receiver whose operation employs heterodyne detection (e.g. radio or GPS receivers) must have low phase noise at short timescales, and thus have an excellent low phase noise oscillator. Even for typical CSACs, the phase noise is set by the VCO at timescales shorter than 0.01 s (this specification will be important for looking at noise later in chapters 4 and 5). The timing

community hopes for smaller stable oscillators due to restrictions on power requirements for receivers [2].

To date, most research into low noise oscillators has focused on improvement of quality factors and insertion losses [4]. Phenomenological modeling of *isochronous* oscillators (no frequency-amplitude coupling) has been successful since additional phase noise due to amplitude fluctuations converting to phase fluctuations were not considered since these, in general, increase phase noise. Understanding the phase noise of a *nonisochronous* oscillators (frequency-amplitude coupled) [9] gives hints [10] that mechanical feedback oscillators might give lower phase noise than their isochronous counterparts. Here we explore the effects that mechanical nonlinearity (which couples frequency and amplitude together) has on oscillators.

Besides the noise of a single oscillator, the interaction between two weakly coupled oscillators is explored in terms of their mutual entrainment (synchronization). The two oscillators' frequency-amplitude coupling will act to shift frequencies to assist in the synchronization. We show that even though the noise increases in two oscillators when resonator frequency and amplitude are coupled (chapter 4), their chance of synchronization also increases, which can reduce the phase noise (chapter 5).

1.2 Definition of an Oscillator

Oscillators form a class of nonlinear dynamical systems which has a phase variable θ which is neutrally stable, or “free”[11]. Neutrally stable dynamical variables neither grow nor decay with perturbations, and thus retain a history of perturbations. Simply put an oscillator with frequency fluctuations obeys the equation

$$\frac{d\theta}{dt} = \omega_0 + \xi(t), \quad (1.1)$$

where ω_0 is a constant angular frequency, and ξ is a random variable in frequency. Thus,

$$\theta(t) = \omega_0 t + \int_0^t \xi(t') dt' + \theta_0, \quad (1.2)$$

and so the phase retains the history of ξ . At this point, this might seem like equation (1.2) is obviously true for all ‘simple harmonic oscillators’. Note that a spring-mass system with external resonant forcing has the form

$$m\ddot{x} + kx + \gamma\dot{x} = F\cos(\omega_d t), \quad (1.3)$$

where m is the mass, k the stiffness, γ the damping, F the forcing amplitude, and ω_d the frequency of excitation. This equation exhibits no phase freedom, in contrast with the oscillator. Here the phase of the resonator has a fixed relationship with the drive,

$$\theta(t) = \tan^{-1}\left(\frac{k/m - \omega_d^2}{2\gamma\omega_d}\right) + \omega_d t. \quad (1.4)$$

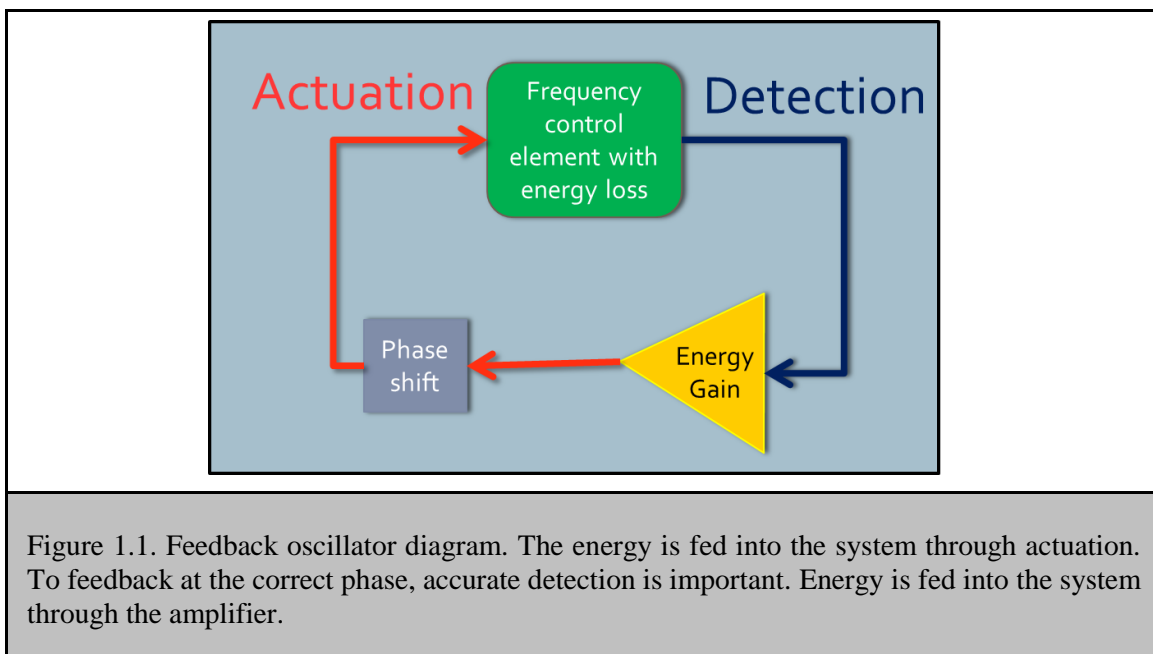
As long as the driving frequency is constant, the spring-mass system cannot be perturbed away from this phase relationship, i.e. changes in phase do not grow in time. The phase is not free, it is completely determined by the external forcing.

There is much confusion for the physics community between oscillators and these driven ‘simple harmonic oscillators.’ Although this language is used between physicists, to avoid

confusion, in this document, *resonator* will be used to refer to a system that exhibits resonance such as the spring-mass system above, and *oscillator* specifically to oscillations with a free phase.

1.3 Feedback Oscillators

Of course there must be a way to create oscillations without an external frequency source, otherwise we are left with an infinite regression of driven systems. To understand how this is done in crystal oscillators, we will now focus on a particular class of oscillators known as *feedback oscillators*. The basic design flow of a feedback oscillator is shown in Figure 1.1.



The frequency control element is essentially the timekeeper here, with the amplitude being sustained by energy being fed back into the system through amplification. Since the energy must be fed back in so as to have constructive interference with the frequency control element (this is

the Barkhausen criterion), sometimes a phase shifting element is used. Note that an oscillator consists of more than just a resonator, and so its properties depend on every component of the system. This type of system will create ‘spontaneous’ oscillations. In the dynamics community, these are called *limit cycle oscillations*. A limit cycle is a periodic path in the phase diagram of a dynamical system. If surrounding points in phase space are attracted to the limit cycle, it is known as an attracting limit cycle. Another way of thinking about this is that the oscillator energy grows due to some positive energy input (from electrical gain in electrical oscillators, gravitational potential energy in weight-driven pendulum clocks), but cannot grow *ad infinitum* due to either a damping nonlinearity or saturation of supply from the energy source.

A simple example of a limit cycle oscillation is a spring-mass system with linear gain and nonlinear dissipation. This model (also known as the van der Pol oscillator) is expressed mathematically

$$m\ddot{x} + kx + \gamma\dot{x} + \eta x^2\dot{x} - g\dot{x} = 0 \quad (1.5)$$

where we have added a gain term g and a nonlinear damping term η to the damped harmonic oscillator. In Figure 1.2, the van der Pol oscillator has been simulated for long times with different initial conditions and parameter values. When $g > \gamma$, a stable limit cycle arises out of the stable fixed point. The growth of the amplitude is bounded from below by the gain, and from above by the nonlinear dissipation η .

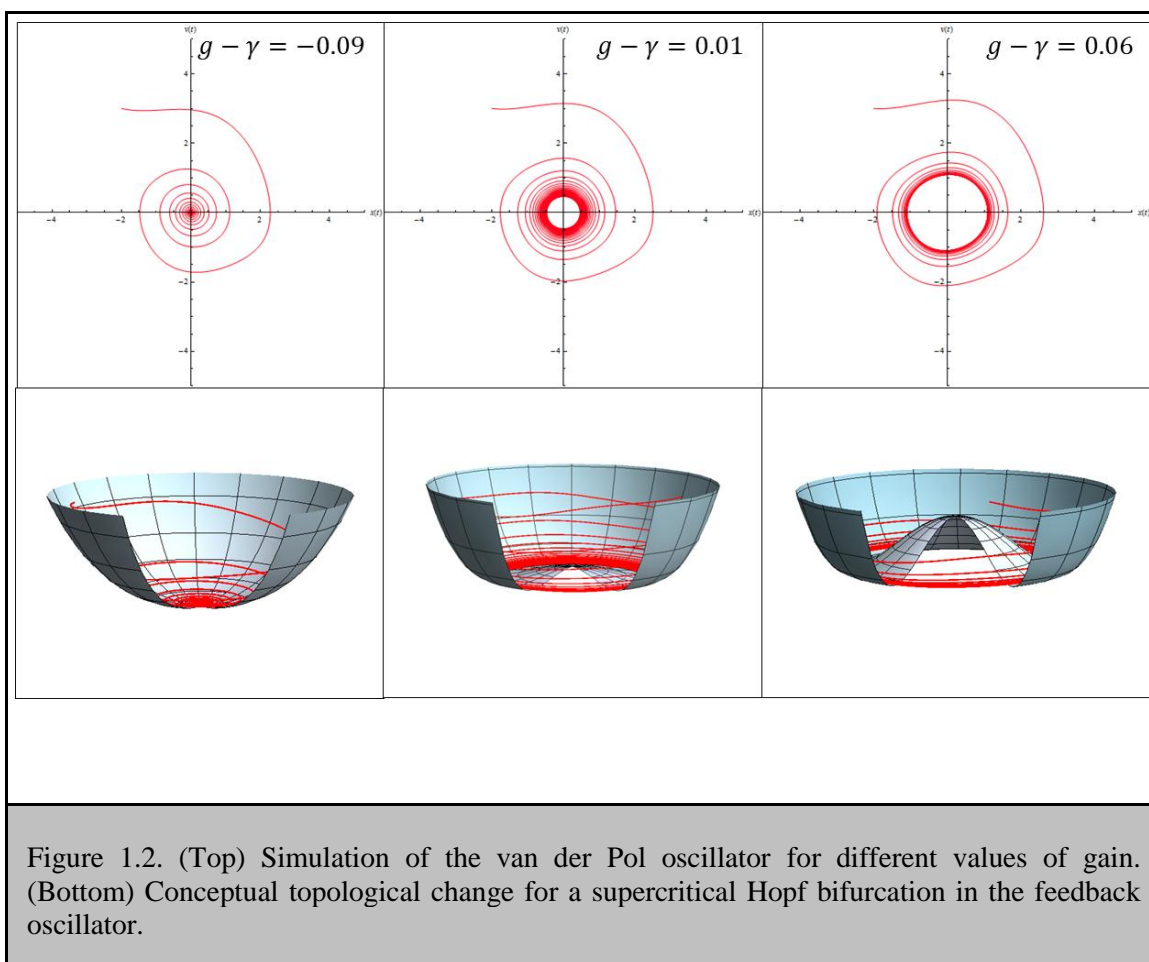


Figure 1.2. (Top) Simulation of the van der Pol oscillator for different values of gain. (Bottom) Conceptual topological change for a supercritical Hopf bifurcation in the feedback oscillator.

This phenomenon of a stable fixed point transitioning into a stable limit cycle is known as a supercritical Hopf bifurcation. This bifurcation can be thought of as a heavily damped (in the radial direction) particle under constant torque (in the direction with angular symmetry) in a higher order paraboloid of the form $y(r) = ar^2 + br^4$. As a changes sign from positive to negative, the minimum of the paraboloid switches from being a point in the center to a circle and the particle starts moving in the θ direction at a constant rate. In Figure 1.2, it is easy to see that perturbations in the radial direction will decay back to the minimum of the paraboloid and keep circling around. Bifurcations represent a fundamental change in the topology of a dynamical

system as a parameter is varied, which, in the case of the van der Pol oscillator, is the gain/dissipation.

1.4 Phase Noise in Oscillators

As previously mentioned, oscillators have become ever smaller since their introduction. Quartz has been no exception, and recently academia and industry have moved past quartz into the realm of micromechanical resonators (MEMS). This has been due to increased availability and reliability of microfabrication equipment. Concurrently, solid state amplifiers have been decreasing in size and cost, so that the whole resonator/amplifier package can be miniaturized (for more information see reference [1]).

Obviously, this miniaturization can be extended further into the realm of nanoelectromechanical systems (NEMS). However, there are challenges to maintaining low frequency noise (or phase noise) as mechanical systems shrink down to the nanoscale. Most NEMS devices have only been operated using flexural vibrations, thus causing the dynamic range of operating amplitudes to shrink significantly [12] (we will return to this point later in Chapter 3).

The phase noise of an oscillator is conventionally quantified by an expression due to Leeson [13]

$$\mathcal{L}_\phi(\Delta\omega) = 10\log\left[\frac{P_{sideband}(\omega_c + \Delta\omega)}{P_{carrier}}\right] \quad (1.6)$$

where ω_c is the carrier frequency, $P_{sideband}$ is the noise in the sideband at a frequency $\Delta\omega$ away from the carrier frequency, and $P_{carrier}$ is the carrier power. Equation (1.6) does not elucidate

sources of phase noise, only phenomenologically how it is measured, much like how current and voltage do not elucidate the source of resistance.

One way to understand Equation (1.6) is by applying the Ergodic theorem to the oscillator system [14]. That is, the average phase of one oscillator is equivalent to an average measure of phase of many oscillators started at the same phase at $t = 0$, and measured at a later time after noise has diffused the ensemble. Phase fluctuations will shift each member of the ensemble of oscillators into different phases, a process known as dephasing.

With no amplitude-frequency coupling (which will cause amplitude modulation to couple to frequency modulation, i.e., AM-PM conversion) amplitude fluctuations will not cause phase fluctuations. One of the goals of this thesis is to explore the effects of AM-PM conversion on phase noise in NEMS oscillators.

1.5 Isochrones and AM-PM conversion

We define an isochrone as the set of points on in phase space which decay to the same phase on the limit cycle. We show the isochrones evolution under a changing nonlinearity using the example of the van der Pol oscillator (equation (1.5)) with nonlinear stiffness. The slow time dynamics (Appendix I) can be described by an amplitude a (with g and η scaled from equation (1.5)),

$$\frac{da}{dT} = \frac{g}{2}(1 - \eta a^2)a, \quad (1.7)$$

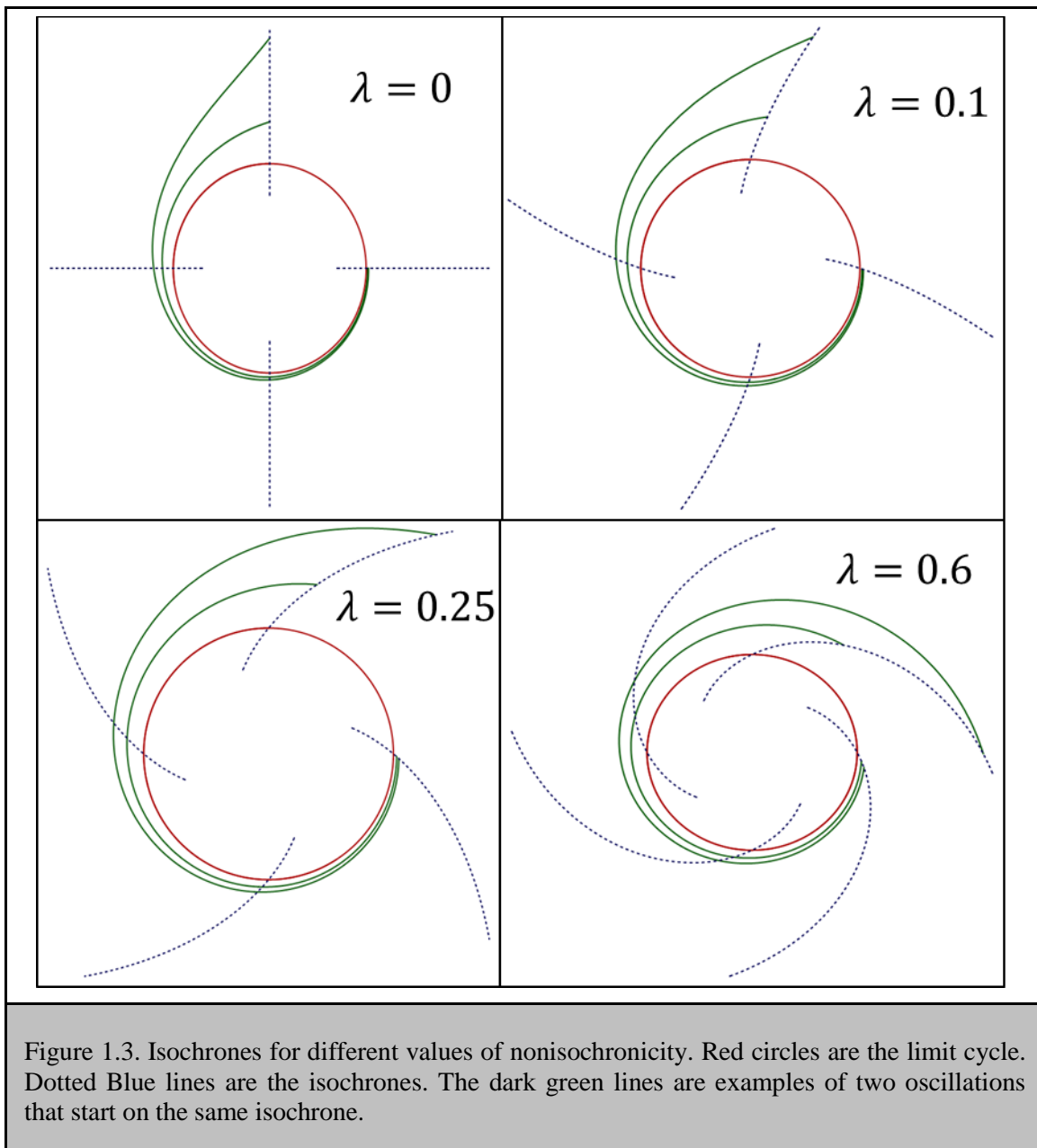
and with frequency (in the rotating frame) Ω defined by,

$$\Omega = \frac{d\varphi}{dT} = \frac{\delta}{2} + \lambda a^2, \quad (1.8)$$

where δ is the frequency at low amplitudes in the rotating frame, and λ is the nonlinear stiffness.

We diagram the solution to the amplitude and phase of this oscillator in the red circles of Figure

1.3.



In Figure 1.3, the isochrones are the dotted blue lines. The green lines represent the oscillator phase trajectory under two different initial amplitudes, but starting on the same isochrone. As time progresses, they evolve to an isochrone different from the one they started on. However,

they share that isochrone. As time progresses further (but not shown) they evolve to the same point on the limit cycle. Thus, in the ensemble picture, different amplitude perturbations along the isochrones lead to no dephasing. Notice that only for the case when the nonlinear parameter $\lambda = 0$, there is dependence of the frequency on amplitude.

As can be seen for these sets of isochrones, they become less orthogonal to the limit cycle as the parameter λ is increased. This is the definition of isochronicity for oscillators. If the isochrones are perpendicular to the limit cycle, then it is isochronous, otherwise it is nonisochronous. And the amount of nonisochronicity is given by the parameter λ . Chapter 3 is dedicated to calibrating this parameter in nonlinear mechanical systems.

From Figure 1.3, it is clear that if we take our ensemble (with only two being shown) picture and apply it to oscillators with $\lambda \neq 0$ and perturbed in the radial direction (and hence not along the isochrones), this will lead to the dephasing that grows as the nonisochronicity increases.

1.6 Thesis Layout

The thesis is divided as follows.

In chapter 2, transduction techniques are discussed, since the choice of transduction turns out to be extremely important for the type of measurement performed. In particular two types of electromechanical transduction are discussed: piezoelectricity and piezoresistivity. Comparison of the theoretical responsivity of these mechanisms is compared to experiment. Noise analyses are carried out for both types of detection, with results from piezoresistive detection.

Next, chapter 3, we are discuss how to calibrate and quantify amplitude, and therefore, nonlinearity, in driven nonlinear piezoelectric/piezoresistive NEMS resonators. In particular, a

nonlinear stiffness tensor is extracted for a nearly ideal nanomechanical doubly clamped beam in order to show the agreement of the calibration technique with nonlinear Euler-Bernoulli theory. Non-ideal beams with an asymmetric potential are explored, with the asymmetry achieved by generating a static deflection.

In chapter 4, oscillators with nonlinear nanomechanical resonators are explored. This includes prediction of the frequency and amplitude of such oscillations given the properties of a nanomechanical doubly clamped beam with a feedback function based on measurements of the feedback network. Phase noise for the heavily saturated oscillator will be closely examined theoretically and compared to experimental data taken using a piezoelectric-piezoresistive oscillator.

Finally in chapter 5, an experiment on the synchronization of two nearly identical oscillators is presented. Quantitative calibration of system parameters is discussed in detail. Dynamical parameters, such as coupling and nonlinear stiffness, are varied, and their synchronized states discussed. Phase noise is compared between locked and unlocked states. Sign of the coupling is reversed, from repulsive to attractive, and differences are explored.

Bibliography

1. F.G. Major, *The quantum beat : the physical principles of atomic clocks*. 1998, New York: Springer. xiv, 475 p.
2. ***A history of the development of CMOS oscillators: The dark horse in frequency control***
M.S. McCorquodale and V. Gupta
in Frequency Control and the European Frequency and Time Forum (FCS), 2011 Joint Conference of the IEEE International, 2011.
3. ***A review of the recent development of MEMS and crystal oscillators and their impacts on the frequency control products industry***
C.S. Lam
in Ultrasonics Symposium, 2008. IUS 2008. IEEE, 2008.
4. ***A review of MEMS oscillators for frequency reference and timing applications***
J.T.M.v. Beek and R. Puers
Journal of Micromechanics and Microengineering, 2012, 22(1), 013001.
5. S.H. Strogatz, *Nonlinear dynamics and Chaos : with applications to physics, biology, chemistry, and engineering*. Studies in nonlinearity. 1994, Reading, Mass.: Addison-Wesley Pub. xi, 498 p.
6. ***Frequency Comparison of Two High-Accuracy Al⁺ Optical Clocks***
C.W. Chou, D.B. Hume, J.C.J. Koelemeij, D.J. Wineland and T. Rosenband
Physical Review Letters, 2010, 104(7), 070802.
7. ***Microfabricated atomic clocks and magnetometers***
S. Knappe, P.D.D. Schwindt, V. Gerginov, V. Shah, L. Liew, J. Moreland, H.G. Robinson, L. Hollberg and J. Kitching
Journal of Optics A: Pure and Applied Optics, 2006, 8(7), S318.
8. ***Oscillator-free atomic clock using a multimode laser***
S.H. Yim and D. Cho
Applied Physics Letters, 2010, 96(21), 211119.
9. ***Phase noise in oscillators: a unifying theory and numerical methods for characterization***
A. Demir, A. Mehrotra and J. Roychowdhury
Circuits and Systems I: Fundamental Theory and Applications, IEEE Transactions on, 2000, 47(5), 655-674.
10. ***Evading amplifier noise in nonlinear oscillators***
D.S. Greywall, B. Yurke, P.A. Busch, A.N. Pargellis and R.L. Willett
Physical Review Letters, 1994, 72(19), 2992-2995.

11. A. Pikovsky, M. Rosenblum and J. Kurths, *Synchronization : a universal concept in nonlinear sciences*. The Cambridge nonlinear science series. 2001, Cambridge: Cambridge University Press. xix, 411 p.
12. H.W.C. Postma, I. Kozinsky, A. Husain and M.L. Roukes, *Dynamic range of nanotube- and nanowire-based electromechanical systems*. Vol. 86. 2005: AIP. 223105.
13. ***A simple model of feedback oscillator noise spectrum***
D.B. Leeson
Proceedings of the IEEE, 1966, 54(2), 329-330.
14. ***Virtual damping and Einstein relation in oscillators***
D. Ham and A. Hajimiri
Solid-State Circuits, IEEE Journal of, 2003, 38(3), 407-418.

Chapter 2

Piezoelectric and Piezoresistive

Transduction

In this chapter we develop a basic understanding of the mechanisms by which we translate signals between the electrical and mechanical domains. We calibrate mechanical nonlinearity in later chapters through precise calibration of device amplitudes coupled with a linear electronic output. We argue that with two examples of strain transduction, piezoelectricity (PZE) and piezoresistivity (PZR), we can perform such calibration. For piezoelectrically and piezoresistively transduced nanoelectromechanical systems (NEMS), we develop theoretical models relating the currents to displacements, and verify them through experiments which use devices made from aluminum nitride and molybdenum. After presenting a noise analysis for both piezoelectric and piezoresistive detection, we compare the two detection schemes for use in the later parts of the thesis. *The theory for the transduction mechanism was developed by Guillermo Villanueva. The piezoelectric material was deposited by collaborators at CEA-Leti, Grenoble, France.*

2.1 Introduction

The realization of transduction between mechanical displacement and velocities into electrical voltages and currents remains a broad area of research within the MEMS and NEMS community [1-4]. Much of the impetus for the NEMS community to find ever more sensitive transducers was to increase operating frequencies of resonant devices. These efforts have led to the realization of room temperature detection of mechanical motion at very high frequencies [3] with transducer amplitude noise being much lower than mechanical domain amplitude noise, thereby reaching the ultimate in signal-to-noise for mechanical systems in equilibrium. These developments are not only important for the quantum physics community [5-9], but for the technological community as well [10-13], since more sensitive electromechanical transducers allow one to make more sensitive mechanical sensors [14]. However, for characterizing nonlinearities of mechanical systems, requirements other than signal-to-noise ratio (SNR) turn out to be important, and hence the need to develop a transduction technique not yet explored at the scale of NEMS devices, the piezoelectric/piezoresistive scheme.

2.2 Requirements for Nonlinear NEMS Studies

There is a large field of candidate transduction mechanisms from which to choose to do experiments in NEMS. The choice will depend on which properties of the NEMS are important for a particular experiment: these properties include large-scale integrability, sensitivity, linearity, actuation and detection bandwidth, mode/device flexibility, and ease of implementation. We now step through each of these properties and eliminate the transduction mechanisms which do not satisfy the criteria for testing the nonlinear dynamics (at least the ones of interest to us) of nanomechanical systems.

We begin with large-scale integration. One of the goals of this research was to develop a system in which the nonlinear dynamics of large arrays of devices could eventually be experimentally tested. Current technology allows for multiplexing large numbers of electronic signals; however, we must first translate the mechanical displacements into electronic signals. Also, full CMOS integration with controlled processes provides reproducibility of devices, which is desirable [15]. Therefore, it is not practical to develop a system with non-electronic transduction which is not easily to implement at large scales, e.g., using optical or magnetic transducers. Thus, we wish to use a system with all-electronic transduction. This narrows down our field of actuation methods to capacitive [16, 17], thermoelastic [18], and piezoelectric (on-chip [19]) mechanisms, and detection methods to capacitive [16], piezoresistive [11, 20, 21], and tunneling [22, 23] mechanisms.

Transduction nonlinearity can complicate tests of nonlinear mechanics when actuating the device. When strongly coupling to the mechanics, it is important that the electromechanical actuation is linear. To give an example, when using capacitive actuation with a static voltage bias, the overall electromechanical nonlinearity is now dominated by the electrical nonlinearity [17]. Therefore, we eliminate capacitive actuation from our field of potential transduction mechanisms.

The electronic detection does not need to couple strongly to the mechanics to give a nonlinear output response. There are three possible mechanisms for the detected electrical signal to be nonlinear with linear drive: mechanical nonlinearity, electromechanical transduction nonlinearity, and purely electronic nonlinearity between the transducer and output port. If linearly increasing the power in the mechanics does not create a linear increase in the electrical output, this implies detector nonlinearity, which can be confused with mechanical nonlinearity. From our possible list of candidate transduction mechanisms, we can therefore eliminate detection mechanisms based on capacitive forces and electron tunneling.

In order to explore nonlinearity more generally, the transduction should allow for the exploration of a number of modes and devices in a wide range of frequencies. An example where this is not possible is magnetomotive transduction, which requires a closed current loop [4]. This method has been primarily limited to odd modes of doubly clamped beams. Although this requirement eliminates no candidates from our list, we point out that thermoelastic actuation, piezoelectric actuation, piezoresistive detection, and piezoelectric detection all satisfy this requirement.

We must now choose between thermoelastic and piezoelectric actuation. The work on driven nonlinear NEMS (chapter 3) can be done with thermoelastic actuation; however, thermal currents travel through the device and reduce the signal-to-background ratio. This is detrimental to the construction of self-sustaining oscillators (chapters 4 and 5) since the background can interfere with the device output when fed back to the input. The usual method to eliminate background signals is to mix the mechanical signal [24] into an electronic frequency band far from the input signal's frequency. This, however, introduces additional nonlinear electrical components, making it more difficult to model. Therefore, we are left with piezoelectric actuation as the only mechanism which can be used in our studies of nonlinear NEMS.

So far, in terms of detection, both piezoelectric and piezoresistive satisfy all the requirements listed above. To choose between them, we theoretically and experimentally explore these two possibilities.

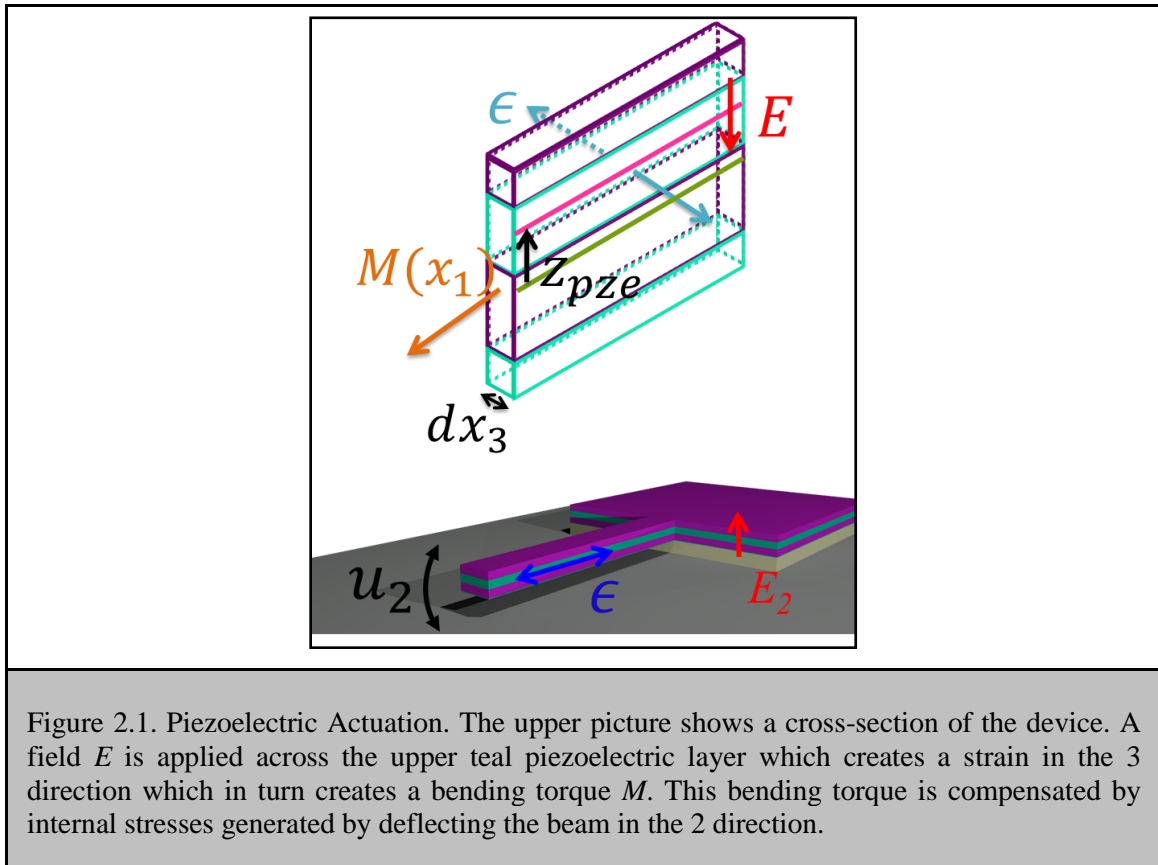
To begin, if we are to predict the detection efficiency of piezoelectric detection, we want to find the piezoelectric coupling constant, d_{23} , which converts between out-of-plane electric fields, and in-plane strain. We do this by measuring the piezoelectric actuation efficiency.

2.3 Derivation of Piezoelectric Actuation Efficiency

Piezoelectric transducers convert energy between the electrical domain and the mechanical domain through strain fields. Actuation with a local piezoelectric transducer makes use of a material ‘sandwich’ in the device (the beam in this case) where top and bottom layers act as electrodes, and the middle layer, which is offset asymmetrically from the center of the material stack, acts as the active piezoelectric layer. This layer is a material which has an inherent asymmetry in the crystal unit cell’s dipole moment, and thus has an intrinsic dipole moment which can be excited electrically to cause strain excitations in the material. This effect is known as the converse piezoelectric effect.

We wish to derive the equation for dynamic piezoelectric actuation in NEMS cantilevers and doubly clamped beams. We will use the result for static piezoelectric actuation (equation (2.4)) to derive the dynamic root-mean-square actuation (equation (2.14)).

It should be noted that there are two types of piezoelectricity. The type of piezoelectric material described above is known as an intrinsic piezoelectric, common to III/V crystalline materials. These materials do not need to be polarized in order to exhibit piezoelectricity. The other class of piezoelectric materials is known as an extrinsic piezoelectrics (e.g., PZT ceramics), in which different crystalline domain walls are present and can be moved by an applied voltage. These materials must be polarized, and hence, are inherently nonlinear at saturated polarizations.



A diagram of the actuation is in Figure 2.1. Here E_2 is an electric field in the out of plane dimension. This causes strain to develop along the longitudinal dimension in the active piezoelectric layer. The teal layer is this active piezoelectric layer which must be offset from the central axis of the beam in order to cause deflection. This offset strain creates a torque, which deflects the beam. The piezoelectric static deflection can be found by noting that in the static case, the net torque through any differential cross-section must be zero,

$$M = \int_{-t/2}^{t/2} \int_{-w/2}^{-w/2} x_2 \sigma_3 dx_1 dx_2 = 0. \quad (2.1)$$

where x_2 is the axis of deflection perpendicular to the layering in the beam, x_1 is the axis of the width, and σ_3 is the stress in the axis of the length. The equation for piezoelectricity gives us an extra term to the stress

$$\sigma_3 = Y\epsilon_3 - Y \frac{d_{23}V}{t_{pze}}, \quad (2.2)$$

where d_{23} is the piezoelectric constant relating electric fields in the x_2 -axis and strain in the x_3 axis, Y is the Young's modulus, t_{pze} is the thickness of the piezoelectric layer in the x_2 -axis, and V is the voltage applied across the piezoelectric layer. We can combine these equations (2.1) and (2.2) for a balance of torques,

$$\begin{aligned} \langle YI \rangle_{beam} \frac{d^2 u_2}{dx_3^2} &= M_{beam} = -M_{pze} = Y_{pze} w \frac{-d_{31}V}{t_{pze}} \int_{h_l}^{h_u} x_2 dx_2 \\ &= Y_{pze} w \frac{-d_{23}V (h_u^2 - h_l^2)}{t_{pze}} = -Y_{pze} w d_{31} V \frac{(h_u + h_l)}{2} \\ &= -Y_{pze} w d_{23} V x_{pze,offset}, \end{aligned} \quad (2.3)$$

with M_{beam} being the normal result from beam theory [25], h_l and h_u are the distances from neutral axis to the bottom and top of the piezoelectric layer, and $x_{pze,offset}$ is the distance from the neutral axis to the center of the piezoelectric layer. Finally, we have the result that

$$\frac{d^2 u_2}{dx_3^2} = \frac{-Y_{pze} w d_{23} V x_{pze,offset}}{\langle YI \rangle_{beam}}. \quad (2.4)$$

For the dynamic case we look at the equation of motion for a flexural beam without drive or dissipation, which is

$$\rho A \ddot{u}_2 = YI \frac{d^4 u_2}{dx_3^4}, \quad (2.5)$$

and gives solutions

$$u_2(x_3, t) = \sum_n (a \cos(\kappa_n x_3) + b \sin(\kappa_n x_3) + c \cosh(\kappa_n x_3) + d \sinh(\kappa_n x_3)) e^{-i\omega_n t} = \sum_n \mathcal{A}_n \Phi_n(x_3) e^{-i\omega_n t}, \quad (2.6)$$

where a, b, c, d are dependent on boundary conditions of the beam in question, Φ_n are the normalized mode shapes, \mathcal{A}_n are the peak amplitude at a maximum of the mode shape, and

$$\kappa_n = \sqrt[4]{\frac{\rho A}{YI} \omega_n^2}. \quad (2.7)$$

The parameter κ_n (and thus the frequency ω_n) can be found numerically once the boundary conditions are in place.

The normalized mode shapes are functions that form a vector space so that the inner product of any two of these functions is the Kronecker delta,

$$\langle \Phi_n | \Phi_m \rangle = \frac{1}{l} \int_0^l \Phi_n \Phi_m dx_3 = \int_0^1 \Phi_n \Phi_m d\xi = \delta_{nm}, \quad (2.8)$$

where $\xi = \frac{x_3}{l}$. We now proceed to the solution for the dynamic amplitude of the piezoelectrically driven beam.

First, note that the static amplitude u_2 can be written as a linear combination of the basis functions $\Phi_n(x_3)$,

$$u_2(x_3) = \sum_n \mathcal{A}_n \Phi_n(x_3). \quad (2.9)$$

We try to find the coefficients \mathcal{A}_n for each mode. These are found by projecting the static deflection onto one of the modes,

$$\langle \Phi_n | u_2 \rangle = \sum_m \mathcal{A}_m \langle \Phi_n | \Phi_m \rangle = \mathcal{A}_n \langle \Phi_n | \Phi_n \rangle = \mathcal{A}_n. \quad (2.10)$$

Now, we know from Equation (2.5) that

$$\Phi_n = (l \kappa_n)^{-1} \Phi_n^{IV}. \quad (2.11)$$

We put Equation (2.11) into (2.10) to get

$$\begin{aligned} \mathcal{A}_n &= (l \kappa_n)^{-1} \int_0^l u_2 \Phi_n^{IV} dx_3 = (l \kappa_n)^{-1} \left[u_2 \Phi_n''' \Big|_0^l - u_2' \Phi_n'' \Big|_0^l + \int_0^l u_2'' \Phi_n'' dx_3 \right] \\ &= (l \kappa_n)^{-1} \int_0^l u_2'' \Phi_n'' dx_3 = \frac{(l \kappa_n)^{-1} M_{pze} l^2}{\langle YI \rangle} \int_0^{\lambda_{act}} \Phi_n'' d\xi, \end{aligned} \quad (2.12)$$

with $\lambda_{act} = l_{act}/l$ is the fractional length of the actuation area. We also have the result from equation (2.11),

$$\begin{aligned}
\Phi_n = (l \kappa_n)^{-1} \Phi_n^{IV} \Rightarrow 1 &= \int_0^1 (\Phi_n)^2 d\xi = (l \kappa_n)^{-1} \int_0^1 \Phi_n \Phi_n^{IV} d\xi \\
&= (l \kappa_n)^{-1} \left[\Phi_n \Phi_n''' \Big|_0^1 - \Phi_n' \Phi_n'' \Big|_0^1 + \int_0^1 (\Phi_n'')^2 d\xi \right] \\
&= (l \kappa_n)^{-1} \int_0^1 (\Phi_n'')^2 d\xi,
\end{aligned} \tag{2.13}$$

where we have used the fact that the first and third derivatives go to zero on the boundaries (for beams). We put equation (2.13) into the denominator of the result of equation (2.12) and use the explicit form of the piezoelectric static deflection in equation (2.4),

$$\begin{aligned}
\mathcal{A}_n &= \frac{M_{pze} l^2}{\langle YI \rangle \int_0^1 (\Phi_n'')^2 d\xi} \int_0^{\lambda_{act}} \Phi_n'' d\xi = \frac{-Y_{pze} w d_{23} V x_{pze,offset} l^2 \int_0^{\lambda_{act}} \Phi_n'' d\xi}{\langle YI \rangle \int_0^1 (\Phi_n'')^2 d\xi} \\
&= \frac{-Y_{pze} w d_{23} V x_{pze,offset} l^2 \Phi_n'(\lambda_{act})}{\langle YI \rangle_{beam} \mathcal{J}_{beam,n}} \\
&= \frac{-Y_{pze} w d_{23} V t \zeta_{pze,offset} l^2 \Phi_n'(\lambda_{act})}{\langle YI \rangle_{beam} \mathcal{J}_{beam,n}},
\end{aligned} \tag{2.14}$$

where $\mathcal{J}_{beam,n} = \int_0^1 (\Phi_n'')^2 d\xi$ and This gives the piezoelectric actuation efficiency for a driven beam. This derivation does not depend on the form of the curvature and so works for the cases of one or two clamps.

We can simulate some actuation efficiencies for some beams given the material stacks (see Appendix II) used in this work. In Table 2.1, offset is defined as in Appendix II, and $\lambda_{act} = 0.3$.

Dimensions ($l \times w \times t$) [nm]	stack	$\zeta_{pze,offset}$	Mode	$\Phi'_n(\lambda_{act})$	$J_{beam,n}$	$\mathcal{A}_n(@1V)/Q*d_{23}$ [unitless]
10000x1000x210 (beam)	II	0.19	1	2.78	198	72.6
8000x1000x210 (beam)	II	0.19	1	2.78	198	46.5
10000x1000x210 (beam)	II	0.19	2	0.51	1670	1.60
6000x1000x210 (cantilever)	II	0.19	1	1.37	3.09	831
6000x1000x320 (cantilever)	I	0.03	1	1.37	3.09	58.7

Table 2.1. Predictions for actuation efficiencies. The first three are doubly-clamped beams (with $\lambda_{act} = 0.3$), the second two are singly-clamped beams (with $\lambda_{act} = 1$). We will use the last to predict the piezoelectric coefficient d_{23} .

In these expected amplitudes one can clearly see the influence of the piezoelectric offset, mode number, and length of various devices. The first three geometries are used later in piezoelectric detection, and the last is used here to find the piezoelectric coupling constant.

2.4 Choice of Piezoelectric Material

Masmanidis and Karabalin [23] first showed the potential for local piezoelectric actuation with GaAs PIN semiconducting layer stacks. However, GaAs is not the best choice for a piezoelectric material. Since GaAs is semiconducting, and not insulating, the effective electric fields is reduced in the piezoelectric layer. Also, the substrate must heavily doped in order to make contact with the bottom layer used as an electrode. This is not desirable for actuation, since a highly conductive substrate layer creates a ground plane beneath all the bondpads, increasing the parasitic capacitance, and thus decreasing overall electrical impedance at high frequencies. With the ground plane $\sim 10^{-7}$ m beneath the bondpads which have an area of $\sim 10^{-8}$ m², this gives a capacitance ~ 10 pF. These effects become obvious as frequencies approach the VHF band. Besides the issue of delivering high voltage to the device, this also causes larger feedthrough between bondpads.

GaAs also makes a poor mechanical material. For sensing applications, large stiffness to mass ratios (sonic velocity) are desirable. GaAs has a Young's modulus of ~ 90 GPa, while having a bulk density of 5300 kg/m³.

Although epitaxial GaAs has poor material properties, there are other piezoelectric materials which mitigate the issues discussed above. For example, a very common material in use in the Roukes group [4] is silicon carbide (SiC), which has a large sonic velocity, but poor piezoelectric properties. Another interesting piezoelectric material with high sonic velocity is aluminum nitride (AlN) which, unlike SiC, also has the benefit of having one of the largest [26] intrinsic piezoelectric constants.

Since doping of AlN is not a well-known process, unlike the GaAs material stacks discussed above with doped semiconductor electrodes, metal electrodes were deposited. Only certain metals

are known to work well with AlN, and thus far these are platinum, aluminum, and molybdenum. The molybdenum process was chosen since LETI had success with it at larger scales. It also turns out to be much has a higher stiffness to mass ratio (sonic velocity) than aluminum or platinum.

2.5 Piezoelectric Actuation Experimental Results

In Table 2.2 we show some results for the first set of devices fabricated (Appendix II) from stack I. Here we note that we can actuate multiple modes, with the limit in frequency arising from the detection efficiency of the optical interferometric setup used to read out the NEMS. We also fabricated doubly clamped beams, with similar lengths, but only present the cantilever results.

Cantilever length (μm)	Mode number	Frequency (MHz)	Quality factor
10	1	3.156	1030
10	2	18.23	870
10	3	48.68	760
10	4	91.84	450
8	1	4.85	1030
8	2	27.59	910
8	3	73.52	720
6	1	9.161	960
6	2	48.25	790
6	3	121.2	600
4	1	20.84	640

4	2	94.72	650
2.5	1	40.38	390

Table 2.2. Optically measured piezoelectric cantilevers from Stack I.

Several different wafers with different material stacks were explored. In the beginning, for initial characterization of the new material, the piezoelectric stack was deposited on a silicon handle wafer (Appendix II, stack I). Later, in order to isolate the bondpads from each other by an insulator, the piezoelectric stack was deposited on a silicon oxide layer thermally grown on a high resistivity silicon handle wafer (Appendix II, stack II).

To calibrate the piezoelectric constant d_{23} for this material, we employed two different methods. First, we obtained the amplitude from cantilever beams and compare to the dynamic actuation efficiency. This method requires equation (2.14) and the estimation of the thermomechanical motion from the fluctuation-dissipation theorem to calibrate the amplitude from detected electrical signal [14].

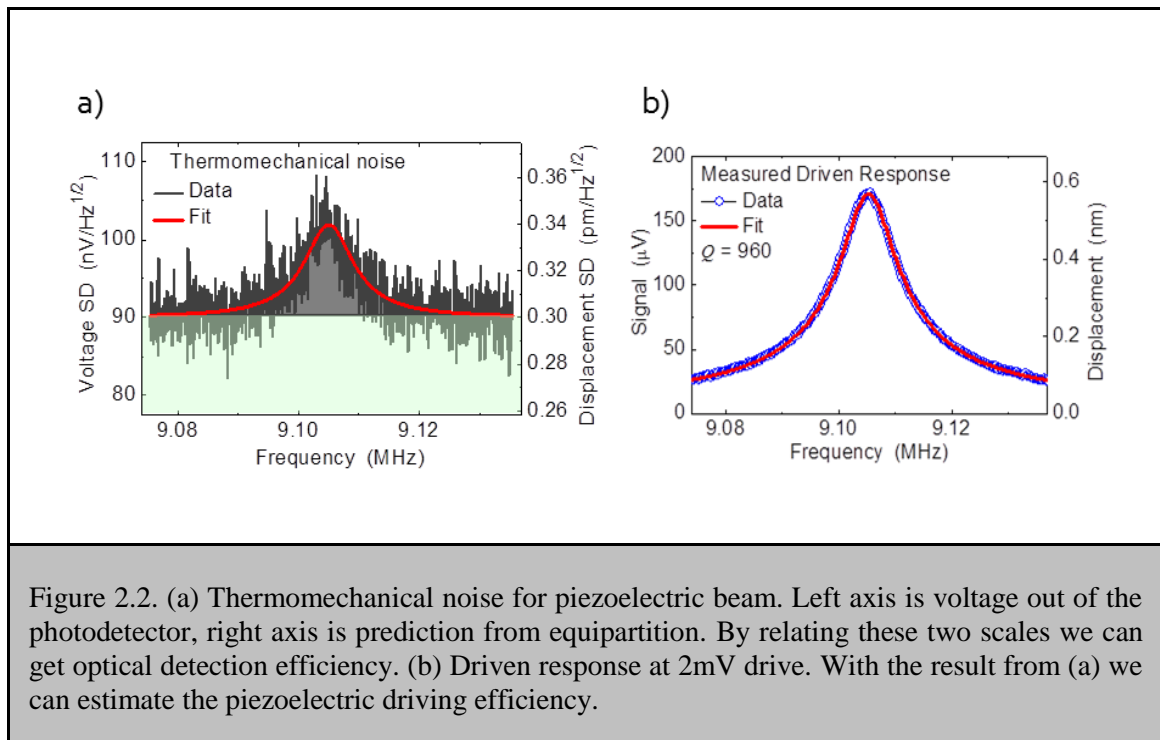
By equipartition, the power spectral density of the displacement noise is given as a function of the stiffness. On peak, we equate the stiffness to the effective mass times the square frequency to get

$$S_x = \frac{4k_b T Q}{m_{eff,n} \omega_n^3}. \quad (2.15)$$

Since the thermomechanical motion can be estimated by calculating the effective masses (which depend on densities and not Young's moduli), it turns out to be a good calibration for

motion at the nanoscale. The effective masses were found using finite element modeling, which agree well with naïve calculations using average density. See Figure 2.2 below.

In (Figure 2.2 (a)), the expected thermomechanical noise at the peak is $0.16\text{pm}/\text{Hz}^{1/2}$ and the voltage noise is $48\text{nV}/\text{Hz}^{1/2}$, so we obtain a detection efficiency of $300\mu\text{V}/\text{nm}$. In figure 2.3 (b), we give the driven response at 2mV drive. This gives a tip displacement of 0.54nm on resonance. Here we use the amplitude found in Table 2.2. For this stack, we get a piezoelectric coupling coefficient $d_{23} = 2.4\text{pm}/\text{V}$, which is only slightly different from the value obtained from centimeter scale cantilevers from the same wafer process using a different setup [27]. The value we calculated from experiment is also only slightly lower than the reported bulk value [28] of $2.6\text{pm}/\text{V}$.



2.6 Derivation of Piezoresistive Detection Efficiency

In mechanical sensing technology, an efficient means of measuring mechanical strain is through piezoresistivity. Although the principle that strain can alter resistance is very simple, the underlying physics is more complex. This change in resistance occurs through two general mechanisms: geometrical deformation and change in resistivity.

Piezoresistive detection can be useful for increasing resonator frequency, since detecting strain is more advantageous at higher frequencies than detecting displacements. To give an example, optical interferometric detection is a method based on measuring small displacements. As flexural resonator frequencies scale up, displacements scale down since resonator/mode size shrinks. Strain scales down as well, but not as fast as displacements. To get a sense of this we can use a simple example, that of a cantilever vibrating in its fundamental mode. We assume a long thin beam, but with finite thickness. Here the displacement of the neutral axis is essentially parabolic along the length of the cantilever. With the assumption of large aspect ratio ($l/t > 5$), it can also be shown that planes perpendicular to the neutral plane remains perpendicular throughout bending [29]. Assume the beam bends towards the top surface (out of plane). This gives a continuous change of strain through the beam from top to bottom, reaching zero strain at the neutral axis. Thus, strain on the top surface is proportional to the ratio of displacement to length. In comparing beams of two different lengths, the amplitude ratio of the beams is less than the strain ratio of the beams $\frac{A_1}{A_2} < \frac{\epsilon_1}{\epsilon_2}$, where beam 2 is longer than beam 1 (with $\frac{\omega_1}{\omega_2} > 1$).

We proceed to derive the equations describing the piezoresistive output signal of a beam under deflection (equation (2.26)). We use this equation to find the theoretical detection efficiency of a doubly clamped beam (Figure 2.4).

We start with the equation for resistance of thin straight wire with resistivity ρ , length l , and cross-sectional area A ,

$$R = \rho \frac{l}{A}. \quad (2.16)$$

Looking at a change in resistance,

$$\delta R = \frac{L}{tw} \delta \rho + \rho \frac{1}{tw} \delta l - \rho \frac{l}{t^2 w} \delta t - \rho \frac{l}{tw^2} \delta w, \quad (2.17)$$

and thus the fractional change in resistance is

$$\frac{\delta R}{R} = \frac{\delta \rho}{\rho} + \frac{\delta l}{l} - \frac{\delta w}{w} - \frac{\delta t}{t} = \frac{\delta \rho}{\rho} + \langle \epsilon_3 \rangle - \langle \epsilon_1 \rangle - \langle \epsilon_2 \rangle. \quad (2.18)$$

Equation (2.18) is the sum of the fractional change of resistivity and the strain in different dimensions. If we use Poisson's ratio ν we get

$$\langle \epsilon_1 \rangle + \langle \epsilon_2 \rangle = -2\nu \langle \epsilon_3 \rangle, \quad (2.19)$$

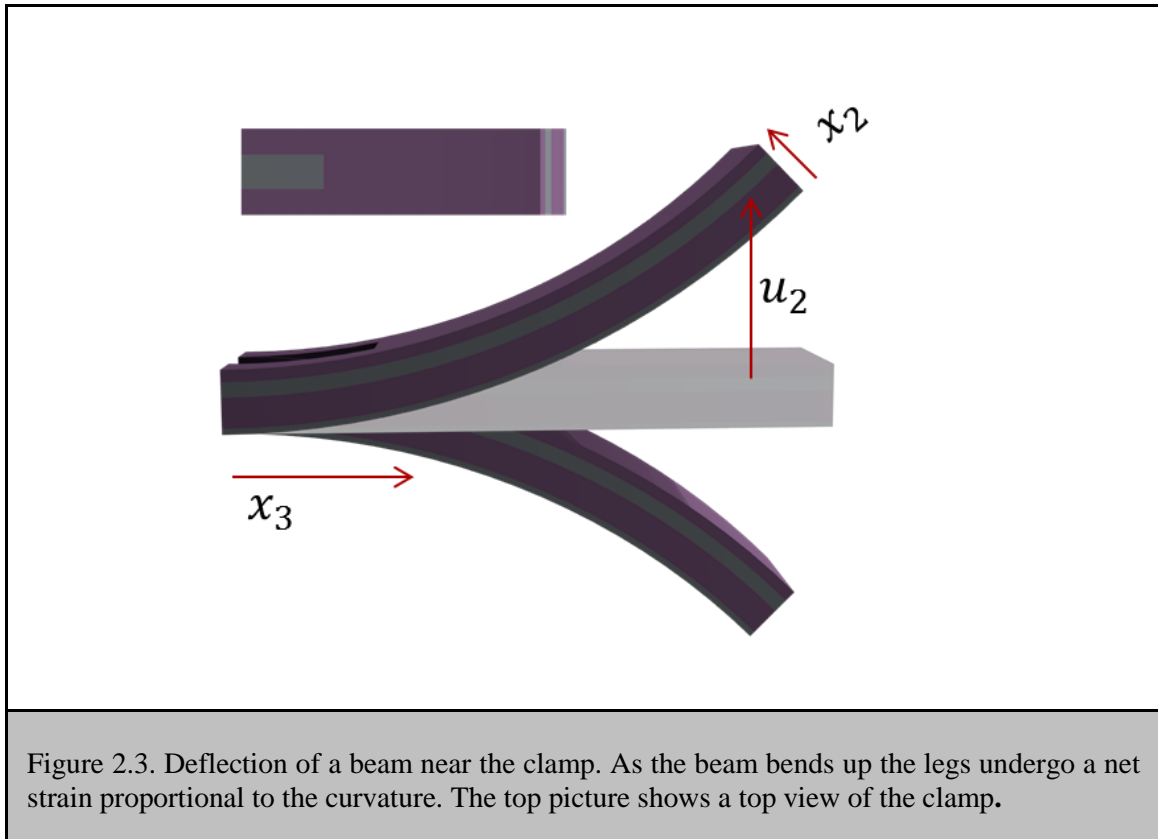
and so with equation (2.18) we define,

$$\left(1 + 2\nu + \frac{\delta\rho/\rho}{\langle\epsilon_3\rangle}\right)\langle\epsilon_3\rangle = G\langle\epsilon_3\rangle. \quad (2.20)$$

where the term in parentheses is known as the gauge factor G . There are two contributions to the gauge factor. One is the geometric contribution, which contains Poisson's ratio, and the other is the fractional change in resistivity. The second contribution is dominant in semiconducting materials, and depends on the change in carrier mobility[30].

The change in resistivity of materials under strain is a complicated subject, which depends heavily on band structure. In this thesis all of the piezoresistive materials are metallic and we assume no change in fractional resistivity. By using the Poisson's ratio for molybdenum we expect $G \cong 1.6$.

In the Roukes group, both semiconducting [20, 21] and metallic [11, 31] piezoresistors have been explored for NEMS. Semiconducting piezoresistors have much larger gauge factors than their metallic counterparts [32]. There are four disadvantages to semiconducting piezoresistors that are relevant to this thesis. The first is that the resistivity (and thus resistance) of these gauges are $\sim 10^4$ times higher. Therefore, it is more difficult to get signals out at high frequencies without impedance matching close to the device. The second disadvantage is the larger $1/f$ noise in semiconductors [33] associated with the smaller density of charge carriers. The third is that piezoresistors based on resistivity changes lead to detected signals which are more nonlinear than signals from piezoresistors based on purely geometric changes. The fourth disadvantage is the large variations in resistance and piezoresistance associated with temperature fluctuations [34]. Thus, metallic strain gauges were chosen. Even though they are not as sensitive, they are shown to be sensitive enough to detect thermomechanical fluctuations, as will be shown later.



The previous derivation for an ‘ideal’ wire (equation (2.20)) can be used to help understand our piezoresistors. From Figure 2.3, the piezoresistor is a current loop with ‘legs’ (the area on top and bottom of the grey section when looking from the top) much longer than the ‘head’ (the rest of the piezoresistor), and assume all the change in resistance is due to the narrow ‘legs’. In the case of a bent Euler beam, the strain in the length dimension (3) has a linear relationship with the thickness dimension (2), $\epsilon_3 \propto x_2$, where x_2 is the offset from the neutral axis of the beam. The neutral plane is defined as the plane passing through length-width dimensions (1-3) which does not undergo longitudinal strain to first order, when subject to flexure. In the case of a beam with uniform Young’s modulus, the neutral axis is in the center of the beam. For the piezoresistor to undergo net strain when the total beam is bent, the central axis of the piezoresistive layer must

offset from the neutral axis. The aforementioned proportionality between strain and offset is related by the curvature of the neutral axis along the beam,

$$\epsilon_3(x_2, x_3) = x_2 * \frac{du_2^2(x_3)}{dx_3^2}, \quad (2.21)$$

where averaging along the thickness x_2 gives

$$\langle \epsilon_3 \rangle = \langle x_2 \rangle * \left\langle \frac{du_2^2(x_3)}{dx_3^2} \right\rangle = \langle x_2 \rangle * \langle u_2'' \rangle = x_{pZR,offset} \langle u_2'' \rangle. \quad (2.22)$$

The separation of the averages in equation (2.22) can only be done if the neutral axis remains perpendicular to the cross-section throughout flexure, since shear displacements can create dependencies in the curvature of the neutral axis on the thickness dimension. Choosing a mode n we have,

$$u_2(x_3, t) = \mathcal{A}_n \Phi_n(x_3) \cos(\omega_n t), \quad (2.23)$$

where \mathcal{A}_n is the peak amplitude of the antinodes of the beam, Φ_n is the mode shape. Equation (2.23) yields

$$\langle u_2'' \rangle = \frac{\mathcal{A}_n}{l^2} \cos(\omega t) \frac{\int_0^{\lambda_{pZr}} \Phi_n'' d\xi}{\lambda_{pZr}} = \frac{\mathcal{A}_n}{l^2} \cos(\omega_n t) * \frac{\Phi_n'(\lambda_{pZr})}{\lambda_{pZr}}, \quad (2.24)$$

where we have normalized along the length of the beam. Here λ_{pzt} is the length of the piezoresistor relative to the beam length. By averaging in the length dimension (3), parts of the piezoresistor which have little to no strain can be detrimental to detector responsivity.

Thus, we get

$$\frac{\delta R_{pzt}(t)}{R_{pzt}} = G \frac{x_{pzt,offset}}{l^2} \mathcal{A}_n \cos(\omega_n t) \frac{\Phi'_n(\lambda_{pzt})}{\lambda_{pzt}}. \quad (2.25)$$

We include the voltage bias and lead resistance to obtain the total signal

$$\begin{aligned} I_{out} &= \frac{V_{bias}}{R_{tot}} \frac{\delta R_{tot}}{R_{tot}} = V_{bias} \frac{\delta R_{pzt}}{R_{pzt}} \frac{R_{pzt}}{(R_{tot})^2} \\ &= V_{bias} G \frac{R_{pzt}}{(R_{tot})^2} \frac{x_{pzt,offset}}{l^2} \mathcal{A}_n \cos(\omega_n t) \frac{\Phi'_n(\lambda_{pzt})}{\lambda_{pzt}}, \end{aligned} \quad (2.26)$$

where the total resistance is the sum of the lead resistance and the resistance of the piezoresistive loop. We introduce the fractional offset for the piezoresistor

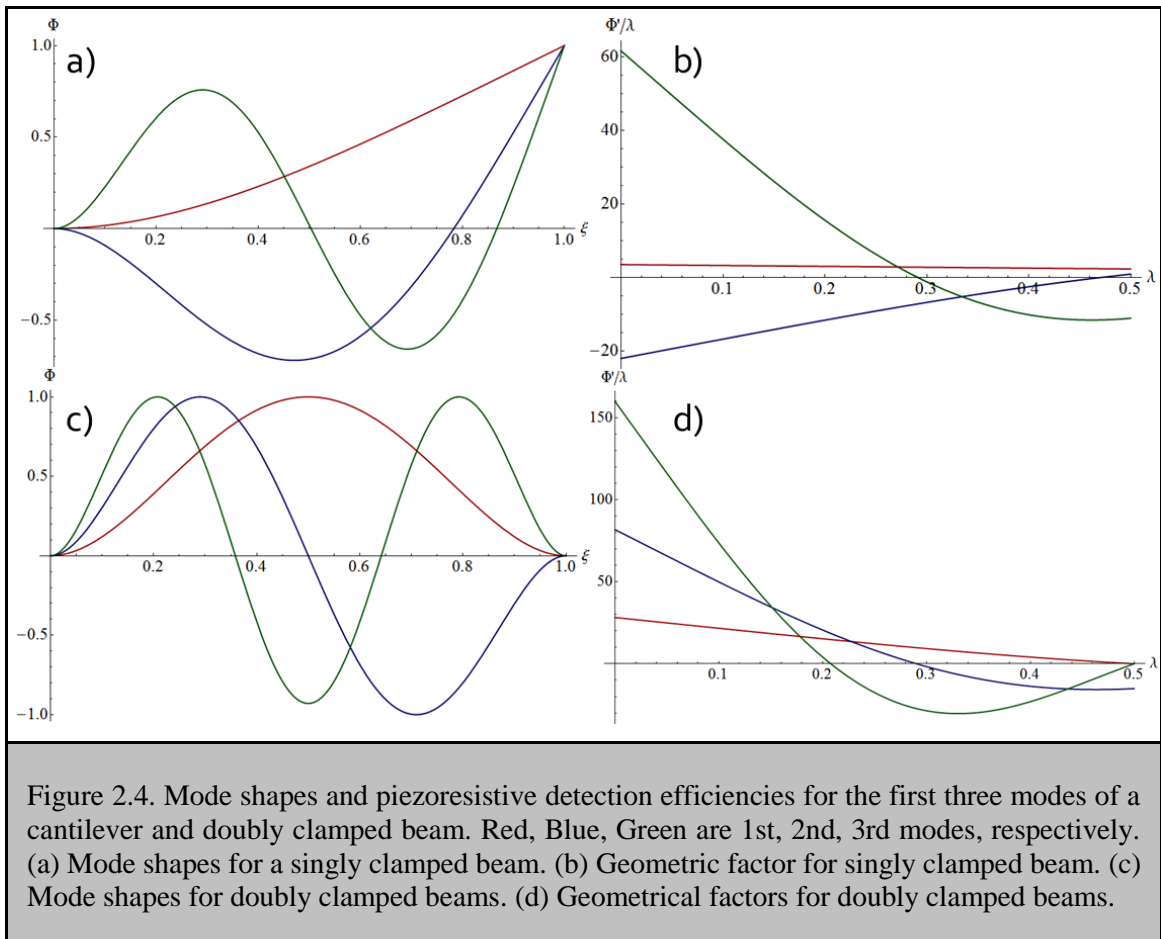
$$\zeta_{pzt,offset} = \frac{x_{pzt,offset}}{t} \quad (2.27)$$

Combining this with the square length in the denominator we can insert the frequency with a numerical constant q_n (found by solving for equation (2.7) with appropriate boundary conditions) we get

$$I_{out} = V_{bias} G \frac{R_{pzt}}{(R_{tot})^2} \zeta_{pzt,offset} q_n \frac{\omega_n}{c_{sonic}} \mathcal{A}_n \cos(\omega_n t) * \frac{\Phi'_n(\lambda_{pzt})}{\lambda_{pzt}} \quad (2.28)$$

We see that the signal is directly proportional to the frequency, which contrasts with displacement detection.

Here $\Phi'_n(\lambda_{pZR})/\lambda_{pZR}$ is a geometric factor related to the fractional length of the piezoresistor. We find that this quantity is maximized at a factor of around 25 for a doubly clamped beam driven in its first mode.



Note the effect that the ratio of the resistance of the piezoresistor (PZR) to the total resistance has on the output signal. If the PZR resistance is much smaller than the total resistance, then the

signal will be significantly reduced. Certainly, there are methods to make this ratio unity: by either making the piezoresistor resistance large compared to the leads, using differential signaling, or making a four terminal measurement.

2.7 Calibration of Piezoresistive Detection Efficiency

We can calibrate the detection efficiency by looking at the thermomechanical motion of a doubly clamped PZE/PZR beam. In Figure 2.5, we ground the driving electrode and measure the total noise coming out of the system. The noise offset (white) here is a combination of the Johnson noise of the resistance, and the amplifier noise referred to the input of the amplifier. The peak buried in the noise background is the thermomechanical noise. The right axis is found using equation (2.15).

The spectral density of the background noise (white) is $\sqrt{S_{v,bg,exp}} = 860pV/\sqrt{Hz}$. We measured the total resistance of the resistance from bondpad-to-bondpad to be $R_{tot} = 70\Omega$. The first stage amplifier voltage and current noise were measured such that $\sqrt{S_{v,amp}} = 150pV/\sqrt{Hz}$ and $\sqrt{S_{i,amp}} = 5.4pA/\sqrt{Hz}$. According to Leach [35], the spectral density for the background noise will be

$$S_{v,bg,the} = \left(\frac{R_{load}}{R_{tot} + R_{load}} \right)^2 * (4k_b T R_{tot} + S_{v,amp} + S_{i,amp} R_{tot}^2), \quad (2.29)$$

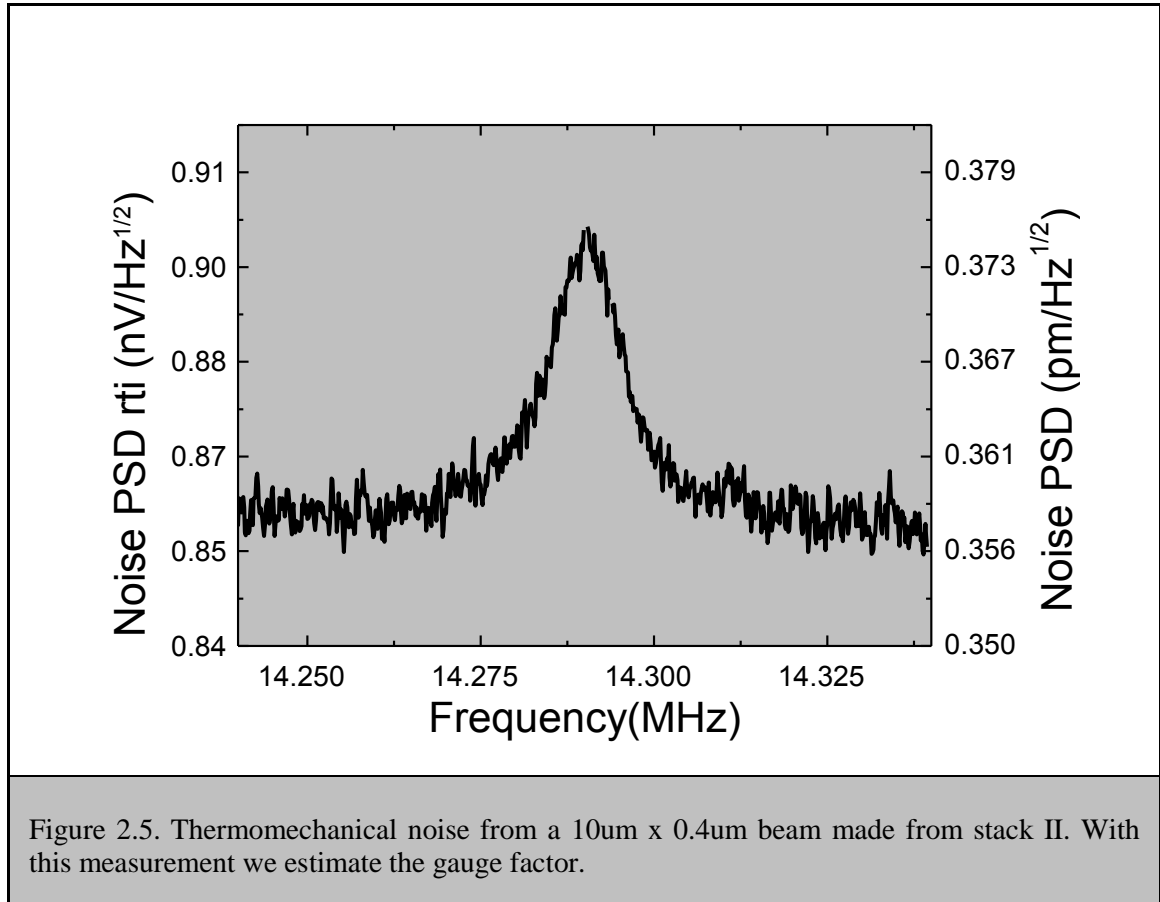
which for gives $\sqrt{S_{v,bg,the}} = 755pV/\sqrt{Hz}$ for $R_{load} = 50\Omega$. This is lower than from the experimental result by $\sim 14\%$. There may be additional noise in the system or a miscalibration of amplifier gain (which is used to get the noise referred to input).

The noise corresponding to the peak is fitted to a Lorentzian and gives a spectral density on peak $\sqrt{S_{v,thm,exp}} = 266pV/\sqrt{Hz}$. We compare the prediction for the thermomechanical noise transduced into electrical noise with this number.

Using equation (2.28) we can estimate the total noise coming from the beam into the first stage amplifier. This is given by

$$\sqrt{S_{i,th}} = I_{bias} \frac{R_{pZR}}{R_{tot}} G \frac{x_{pZR,offset}}{l^2} \frac{\Phi'_n(\lambda_{pZR})}{\lambda_{pZR}} \sqrt{\frac{4k_b T Q}{m_{eff} \omega_0^3}}, \quad (2.30)$$

where we have set $I_{bias} = \frac{V_{bias}}{R_{tot}}$.



The PZE/PZR beam has dimensions $l \times w = 10\mu m \times 400nm$ and is made from stack II (Appendix II). The beam has a measured frequency of $f_0 = 14.3 MHz$, quality factor $Q = 1200$, an estimated gauge factor $G = 1.6$, offset $x_{pzs,offset} = 85nm$, geometric factor $\frac{\Phi'_n(\lambda_{pzs})}{\lambda_{pzs}} \cong 27$, and effective mass $m_{eff} = 3.05 * 10^{-15}kg$. In Figure 2.6, we plot the spectral density on peak (equation (2.30)) against the resistance of the piezoresistor. For the experimental value of the noise, we get the resistance of the piezoresistor to be 60Ω , much higher than the simulated value of 5Ω (which uses the value for resistivity from bulk values and the dimensions of the piezoresistor from the design). This discrepancy arises since the dimensions of the piezoresistor in this beam were not as designed due to lithographic error. Also, bulk values for the resistivity are probably too high for the $40nm$ Molybdenum film.

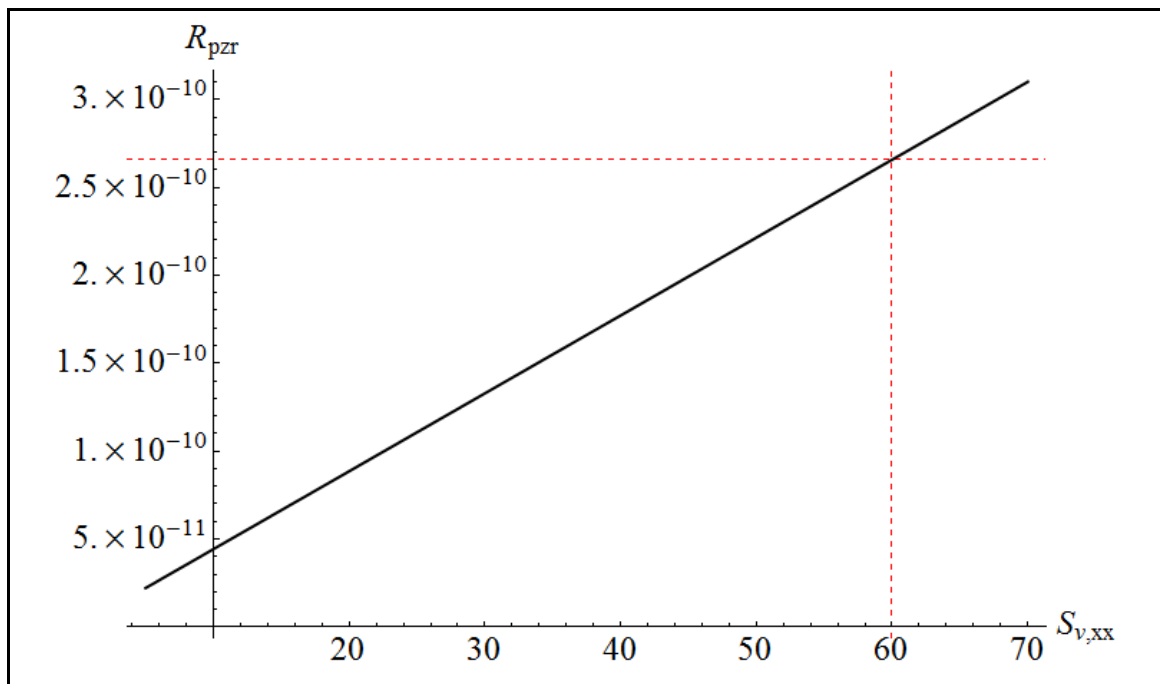


Figure 2.6. Prediction of the thermomechanical noise transduced into voltage noise at the input of the amplifier for the beam from Figure 2.5. The experiment predicts a resistance for the piezoresistor of 60Ω . Red dashed line gives the level of the thermomechanical noise transduced into voltage from Figure 2.5.

2.8 Piezoelectric-Piezoresistive Motional Resistance

We can now match up the piezoelectric actuation with the piezoresistive detection to give the overall *electromechanical (motional) resistance*. In an all-electrical transduction scheme, electromechanical resistance represents the conversion from input signal voltage to output current. That is

$$I_{out} = V_{bias}(t)G \frac{R_{pZR}}{R_{tot}^2} \zeta_{pZR,offset} \zeta_{pZE,offset} * \frac{t^2}{l^2} \cos(\omega_n t) \frac{\Phi'_n(\lambda_{pZR})}{\lambda_{pZR}} \frac{-Y_{pZE} l^2 w d_{23} V_{in}}{\langle YI \rangle_{beam}} \frac{\Phi'_n(\lambda_{act})}{J_{beam,n}} Q. \quad (2.31)$$

When we assume that the piezoelectric young's modulus is the same as the rest of the beam (which is a good approximation for our beams), and putting in a rectangular beam's areal moment of inertia,

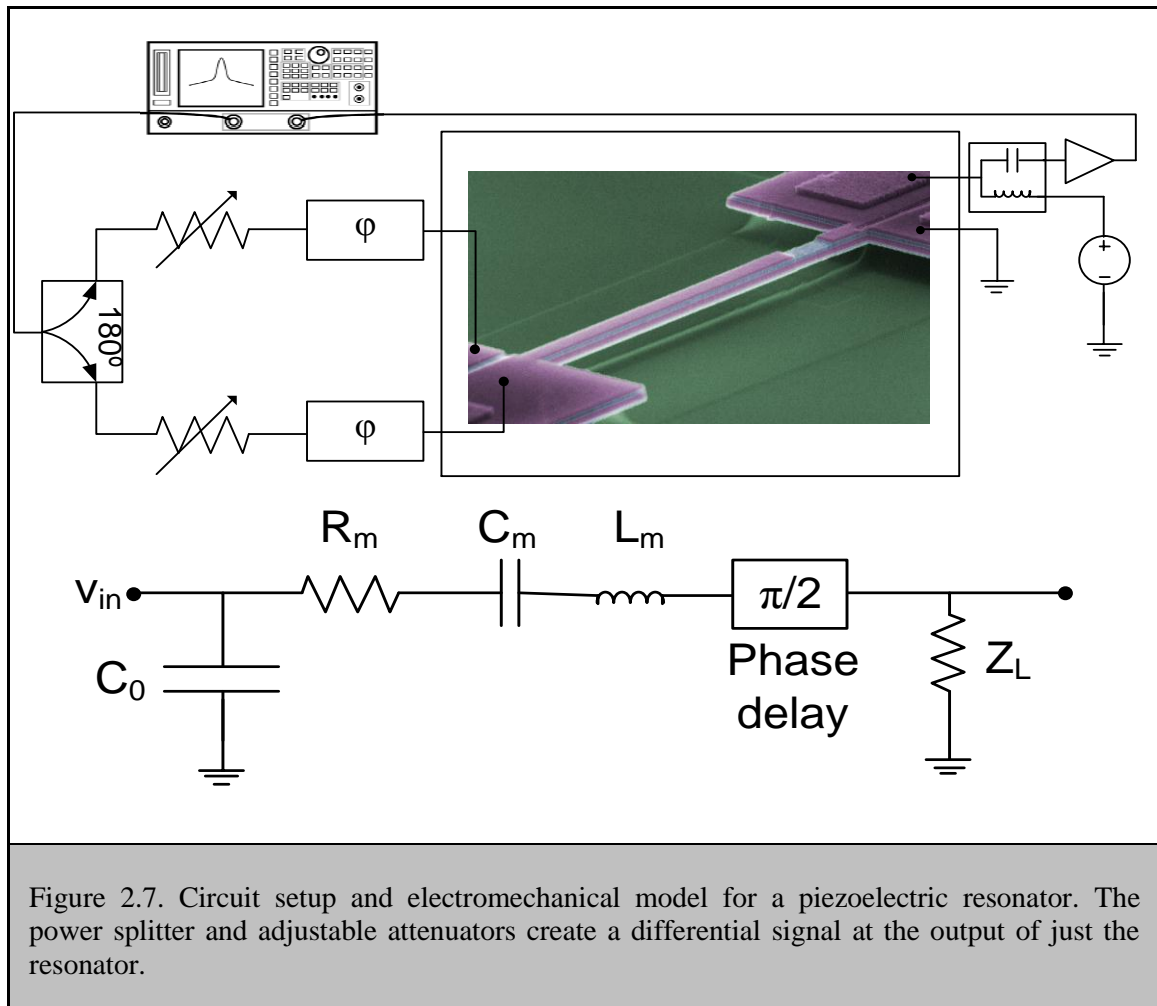
$$I_{out} = 6 V_{bias} G \frac{R_{pZR}}{R_{tot}^2} \frac{d_{23} V_{in}}{t} \frac{\Phi'_n(\lambda_{act}) \Phi'_n(\lambda_{pZR})}{J_{beam,n} \lambda_{pZR}} \zeta_{pZR,offset} \zeta_{pZE,offset} Q. \quad (2.32)$$

We divide the input voltage by equation (2.32) to get the motional resistance

$$R_m = \frac{V_{in}}{I_{out}} = \frac{1}{6 V_{bias} G Q} \frac{R_{tot}^2}{R_{pzt}} \frac{t}{d_{23}} \frac{\lambda_{pzt} J_{beam,n}}{\Phi'_n(\lambda_{act}) \Phi'_n(\lambda_{pzt}) \zeta_{pzt,offset} \zeta_{pze,offset}} \frac{1}{1}. \quad (2.33)$$

We make some observations about equation (2.33). The only parameters that can be changed by modifying the fabrication and materials are the offsets, thickness, and the resistance of the piezoresistor. This means that if thickness is fixed, the motional resistance of the device is constant against changing the length, and hence the frequency. However, if aspect ratio ($l : t : w$) is fixed, the resistance $R_m \propto l$. Thus, higher frequencies actually have *lower* motional resistance. This surprising result implies that the piezoelectric/piezoresistive transduction scheme is optimal for moving to higher frequencies.

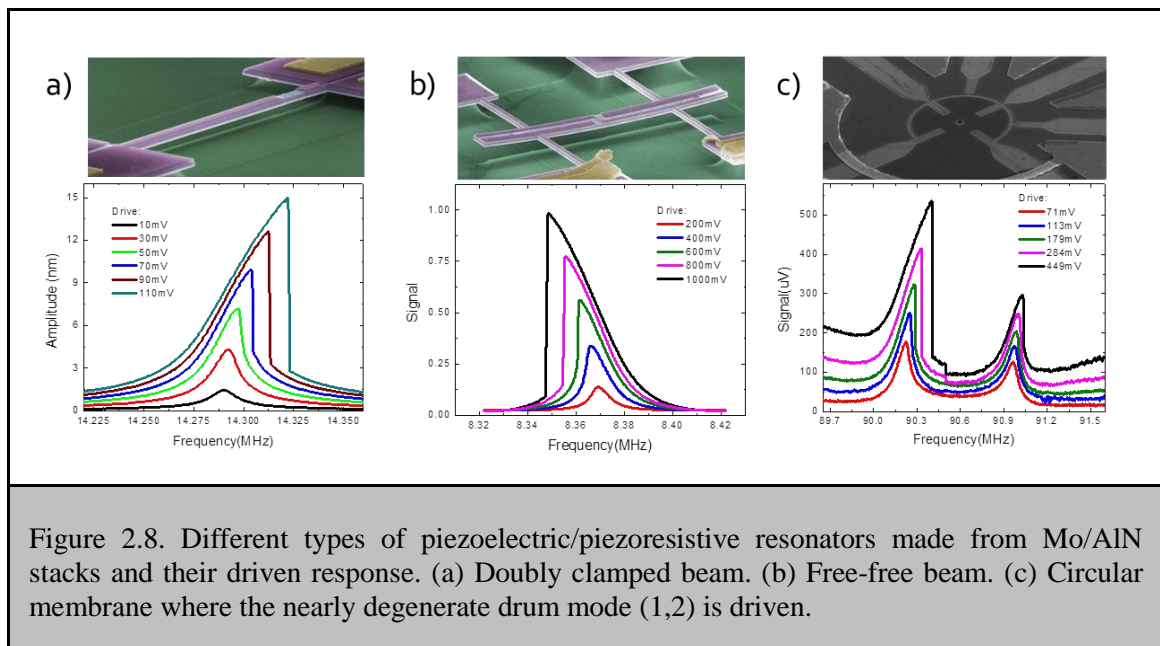
The model which describes the piezoelectric-piezoresistive transduction is really only valid in the small signal approximation since it assumes passive components. However, the piezoresistor is in fact an active device requiring a bias. A more accurate model for the transduction would use a three port active device (such as a transistor). Given a large gauge factor and a thin piezoelectric stack, it may be possible to create *negative* motional resistance, giving a circuit gain larger than 1.



To characterize these devices, we typically have a system setup shown in Figure 2.7. Here, a differential signaling technique (as opposed to applying a single ended voltage to the piezoelectric input) is used to reduce feedthrough signals. The bias tee is used to bias and detect the resonance. The beam can be viewed from an electrical perspective as a series LRC circuit (Figure 2.7), with the motional resistance determining the total output current. A typical sweep is shown in Figure 2.8 (a). The sweep with lowest drive (black line) is Lorentzian. The Duffing nonlinearity for a doubly clamped beam becomes appreciable at amplitudes $\sim 1\text{nm}$ as shown at higher values of drive. For the beam whose thermomechanical noise was shown in Figure 2.5,

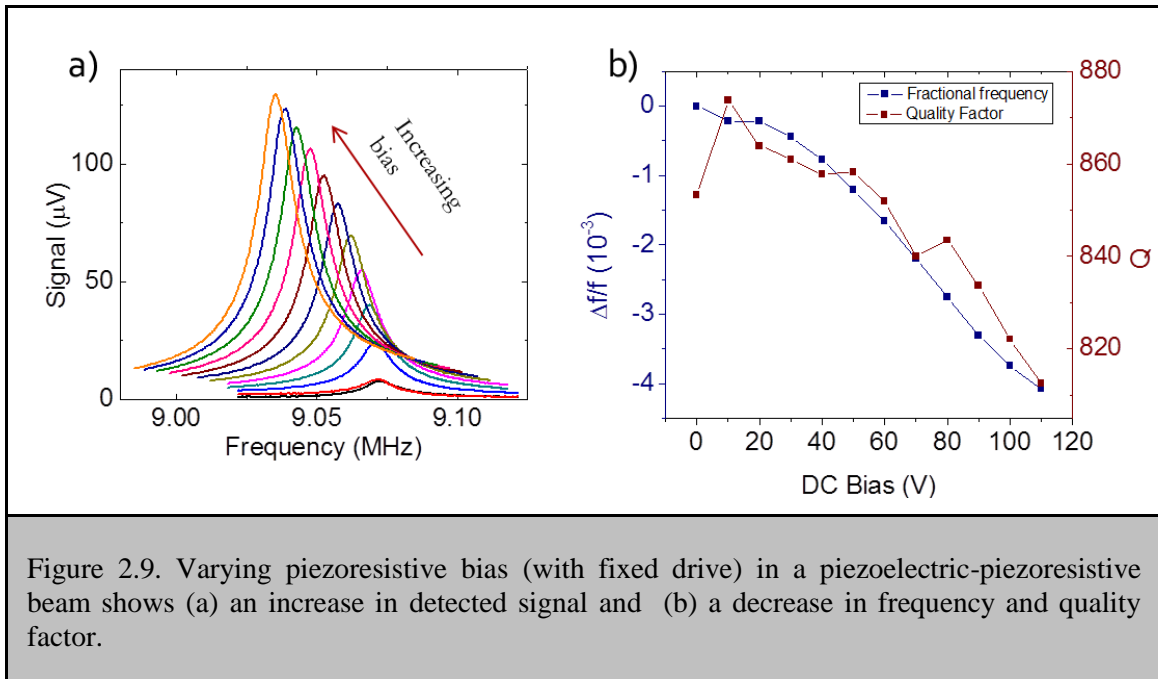
based on the voltage-in compared to the voltage-out, we estimate the motional resistance to be $150k\Omega$. The theoretical prediction of equation (2.33) gives $R_m \cong 160k\Omega$ using parameters found from sections 2.3, 2.5, and 2.7. Thus we see good agreement between experiment and theory.

The PZE-PZR detection scheme is not limited to doubly clamped beams or cantilevers. Two other structures were explored, including free-free beams and circular membranes (drumheads) shown in Figure 2.8 (b,c), respectively. This demonstrates the ability to explore multiple types of resonators and modes since the actuation and detection mechanisms are intrinsically local phenomena, which can be made smaller than the actual device.



The argument for the use of piezoresistive detection is buffeted when we consider the heating of the device. Even though use of a larger bias voltage would increase the output signal as shown in Figure 2.9 (a), there are restrictions. For example, we estimate that the piezoresistor in our beams may heat up as much as 100K at voltages $\sim 500mV$. This causes the frequency to shift and the quality factor to decrease. Since molybdenum and aluminum nitride are known to be

‘tough’ materials with high melting temperatures, the devices can survive, but frequencies and quality factors will decrease. Figure 2.9 (b) shows that for a doubly clamped beam, the frequency and quality factor decrease for an increasing bias.



Since the piezoresistive detection strongly tunes frequency, small temperature fluctuations can cause large frequency fluctuations. Mechanical sensors and oscillators depend on stable frequencies; parametric fluctuations arising from temperature variations in the devices are devastating to performance [36]. Joule heating is proportional to the square of the voltage, and hence, low frequency noise coming from the output port cause low frequency fluctuations in resonant frequency, which will not average out at long integration times.

2.9 All Piezoelectric Transduction Theory

Piezoelectric detection has several advantages over piezoresistive detection. It is a passive detection technique. Therefore, it does not inherently increase the amount of noise in the detection (in resistors, Johnson and $1/f$ noise appear due to motion of the charge carriers). Also, it does not cause heating of the device, which decreases both the quality factor and the resonant frequency.

The challenge for implementing piezoelectric detection is the high motional impedances. A beam of dimensions $10\mu\text{m} \times 1\mu\text{m}$ with a layer of aluminum nitride 50nm thick will have an electrical impedance $\sim 1/\omega C$. Assuming a parallel plate capacitor, this gives a capacitance of $\sim 10\text{fF}$. The beam (stack II) used in this section has a frequency of 12MHz . Thus we get an electrical impedance of $\sim 800\text{k}\Omega$ at this frequency. It turns out the motional resistance is $\sim 10\times$ this electrical impedance (equation (2.41)). Also, the electrical and motional impedances will be dominated by parasitic capacitances when using surface mount technology to amplify the signal, which are usually $\sim \text{pF}$, thus giving a $10\text{ k}\Omega$ shunt. Even using an isolating $2\mu\text{m SiO}_2$ buffer layer on the chip will give a capacitance of $\sim 1\text{pF}$ for a bondpad with dimensions $100\mu\text{m} \times 100\mu\text{m}$. In order to fully appreciate this detection technique, impedance matching, by either cancelling the parasitic capacitance off chip (through the use of an inductance which can eliminate both the device's electrical capacitance and parasitic capacitance of the chip) or amplifying on chip (which eliminates only the parasitic capacitance of the chip), is necessary. In our piezoelectric detection calibration, we do neither, but only compare input to output signal. In order to quickly calibrate the detection efficiency around multiple frequencies, we use a transformer in order to find the driven signal.

We start by calculating the piezoelectric detection efficiency for beams. The ability to produce a dipole moment under strain is known as the *direct* piezoelectric effect. Here we can relate the total current density out to the displacement current D by

$$\vec{J}_{out} = \frac{\partial \vec{D}}{\partial t}. \quad (2.34)$$

Since the piezoelectric sensing electrode is separate from the piezoelectric driving electrode and the current is all in the out-of-plane dimension, along the thickness we get

$$J_{out} = \frac{\partial P}{\partial t} = \frac{\partial}{\partial t} (d_{23} \langle \sigma_3 \rangle) = \frac{\partial}{\partial t} (d_{23} Y_{pze} \langle \epsilon_3 \rangle). \quad (2.35)$$

where the polarization P is equal to the piezoelectric coupling constant d_{23} multiplied by the average stress (this is the direct piezoelectric effect). The strain must be averaged in the thickness dimension since it varies across the thickness, just as in the piezoresistive case. This gives

$$J_{out} = d_{23} Y_{pze} \frac{\partial}{\partial t} (\langle \epsilon_3 \rangle). \quad (2.36)$$

Integrating we get

$$\begin{aligned} I_{out} &= \omega_n d_{23} Y_{pze} w x_{pze,offset} \mathcal{A}_{rms} \int_0^l \Phi''(x_3) dx_3 \\ &= \omega_n \left(d_{23} Y_{pze} w \frac{t}{l} \zeta_{pze,offset} \mathcal{A}_{rms} \Phi'(\lambda_{pze}) \right). \end{aligned} \quad (2.37)$$

Note that if the aspect ratio is fixed (length l to thickness t), the motional current increases as frequency increases.

To obtain the motional resistance we put the result from Equation (2.14) into (2.37) (and noting that the quality factor pumps amplitude by a factor of Q)

$$\begin{aligned}
 I_{out} &= \omega_n \left(d_{23} Y_{pze} w \frac{t}{l} \zeta_{pze,offset} \right. \\
 &\quad \left. * \frac{Y_{pze} w d_{23} V_{in} \zeta_{pze,offset} t l^2 \Phi'(\lambda_{pze,act}) \Phi'(\lambda_{pze,det})}{\langle YI \rangle_{beam} \mathcal{J}_{beam,n}} \right) Q \quad (2.38) \\
 &= 12(V_{in} \omega_0) (d_{23}^2 Y_{pze}) \left(\frac{l}{t} w \right) \left(\frac{(\zeta_{pze,offset} \Phi'(\lambda_{pze,act}))^2}{\mathcal{J}_{beam,n}} \right) Q
 \end{aligned}$$

where we have grouped the terms into circuit parameters, material parameters, dimensional parameters, and device design parameters.

We start with the material parameters. For intrinsic piezoelectrics, aluminum nitride has one of the highest reported piezoelectric constants. Also, the Young's modulus is extremely high among materials (~ 400 GPa). Thus, with the exception of boron nitride, this is probably the best that can be expected for intrinsic nanoscale piezoelectric materials.

For the a doubly clamped beam, the 'device design' parameters in equation (2.38) can be optimized to give $\sim 10^{-3}$, with the piezoelectric element being the upper half of the beam. Thus for a quality factor ~ 1000 , we get

$$I_{out} \cong 10^{-11} (V_{in} \omega_0) \left(\frac{l}{t} w \right). \quad (2.39)$$

So the motional resistance becomes

$$R_m = \frac{V_{in,rms}}{I_{out,rms}} \cong \frac{10^{11}}{\omega_0} \left(\frac{t}{lw} \right). \quad (2.40)$$

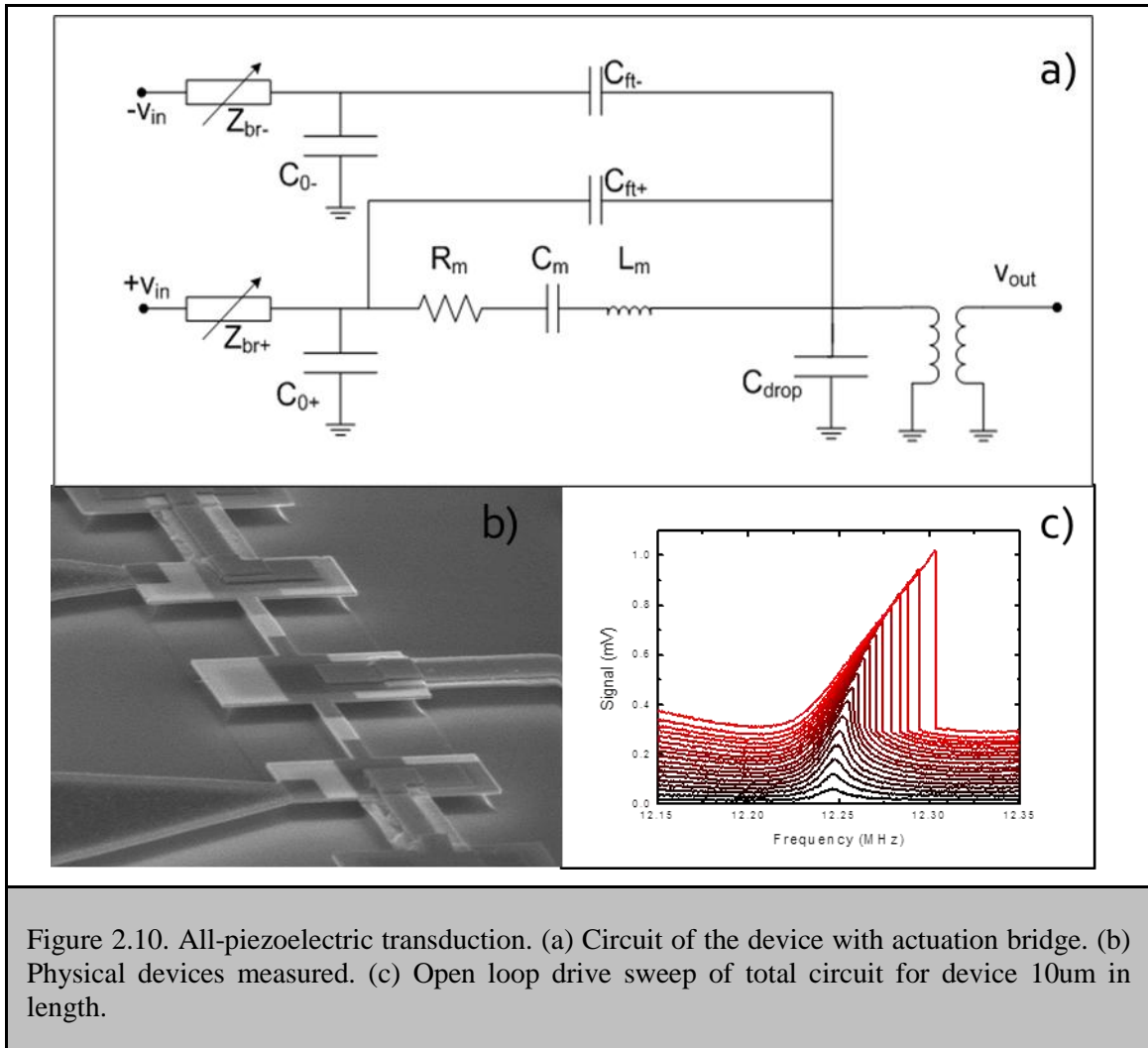
We put the motional resistance in terms of the device's electrical capacitance $C_{el} = \epsilon_{pze}A/t_{pze}$ with $2 * t_{pze} = t$,

$$R_m \cong 2 * 10^{11} \frac{\epsilon_{pze}}{\omega_0 C_{el}} \cong \frac{10}{\omega_0 C_{el}}. \quad (2.41)$$

2.10 All Piezoelectric Transduction Results

We now present some results for piezoelectric detection. An inductive RF transformer was placed close to the board in an attempt to match impedances. While this may not be the way to completely match the device as in the case of an LC tank, since it is broadband (at least up until 30 MHz), several devices can be measured using the same circuit.

In Figure 2.10 we show the piezoelectric detection circuit and sample devices. Figure 2.10 (c) shows a typical sweep of input drive. Notice that the background level is higher than the piezoresistive detection because signals due to the feedthrough capacitance are more effectively transferred to the load due to the matching network.



The parasitic capacitance (C_{drop} and C_{ft}) will be dominated by bonding and board capacitances, and not by the device's electrical capacitance C_{el} . Assuming that this is on the order $\sim 1\text{pF}$, we can treat this as a voltage divider against the output signal. We confirm that it is indeed the case and that parasitic capacitance is approximately 3pF by using a PSPICE simulator. In Table 2.5, we compare those simulations against the collected data for two beams. The longer beam is driven into two different modes to compare the influence of mode number. Also, noting that the device under test (shown in Figure 2.10 (b)) has been modified from an ideal beam, since the top electrode has been removed from the middle third of the beam (which significantly alters the

areal moment and mode shape). Simulations were run in Mathematica in order to accurately integrate the mode shapes.

$L \times w \times t$ (μm)	Mode	f_0 (MHz)	$S_{21,est}$	$S_{21,exp}$
10 x 1 x 0.21	1	12	-81dB	-82dB
8x 1 x 0.21	1	20	-81dB	-83dB
10 x 1 x 0.21	2	35	-101dB	-100dB

Table 2.3: Results for the piezoelectric detection using a transformer. The power transmission was estimated using a 3pF capacitor.

The model gives results within a factor of 2dB for these three measurements. Note that the second mode decreases in transmitted power since the beam electrodes are optimized for the first mode, and that the increase in frequency causes a decrease in the impedance across the parasitic capacitance.

Using an off-chip LC tank [16], matching a $8M\Omega$ (estimated from the dimensions of the beam in Figure 2.7) impedance at a frequency $f_0 = 14.3 \text{ MHz}$ with a shunt capacitance $C_{par} = 3pF$ would need a series inductance of $L = 40\mu H$. We desire a quality factor for the tank to be around $Q \sim 30$. This would give an impedance $Z_{tank} = \sim 50k\Omega$ into the tank from the resonator (assuming 1Ω resistance in the inductor and capacitor coming from the bonds). This gives a power transmission coefficient $S_{21} = -65dB$, $\sim 20dB$ better than the transformer matching.

The power spectral density for the noise voltage coming from the device's thermomechanical fluctuations (equation (2.15)) is given by current in equation (2.37) loaded into the tank impedance. This gives $S_{thm,v} = 1.4nV/\sqrt{Hz}$, which is around 5-6x that of the piezoresistive

output noise. Also, there would be no Johnson noise from the resistance of the piezoresistor, which would give a much better ratio of thermomechanical noise to background noise.

2.11 Choosing Piezoresistive Detection

Using off chip methods at a frequency $\sim 10\text{MHz}$, it seems clear that if we want to observe the thermomechanical motion, piezoelectric detection is superior to piezoresistive detection. However, as frequency increases, matching off-chip methods are limited due to the parasitic capacitance set at $\sim pF$. We only need a method that is sensitive enough to find the thermomechanical motion.

The piezoresistor also gives us a method to control the frequency (through thermoelastic forces) in the range $\sim f_0/10$, which is much better than the piezoelectric tuning range $\sim f_0/100$. We can also use this thermoelastic effect to create large static deflections (as shown in the next chapter).

Also, by attempting to match to the motional resistance, we also match to the feedthrough impedances between input and output, increasing background. This will be problematic for making oscillators (chapters 4 and 5) since feedthrough signals interfere with the oscillation of the mechanical resonator.

Therefore, although piezoelectric sensing has definite advantages in terms of absolute noise, the flexibility and ease of piezoresistive sensing (coupled with its high signal-to-background ratio) make it the preferred candidate.

2.12 Future Work

Integrating semiconductor piezoresistive materials with piezoelectrics could prove an interesting topic of research [26]. Semiconducting piezoresistors not only have larger gauge factors (and therefore higher responsivity), but could also be gated by piezoelectrics, increasing the effective gauge factor. If the gauge factor gets large enough, then the motional resistance could become negative, making a negative resistance mechanical oscillator, which would simplify the task of making oscillator arrays. Embedding a semiconducting piezoresistor could be accomplished through the use of epitaxial doped aluminum nitride, much like the GaAs systems used by Masmanidis and Karabalin [19].

Piezoelectric detection of the small NEMS in the preceding sections proved to be promising using LC tank off-chip. However, as frequencies approach the microwave band, on-chip matching methods would have to be used, and maybe better than piezoresistive sensing. For fixed aspect ratio, the motional resistance of the device does not change, making on-chip matching networks easier to design.

Since this transduction scheme allows many kinds of devices and modes, predicting and measuring the motional resistance of these devices could lead to optimal device designs for applications such as sensing and clocks.

Bibliography

1. *Electromechanical Transducers at the Nanoscale: Actuation and Sensing of Motion in Nanoelectromechanical Systems (NEMS)*
K.L. Ekinici
Small, 2005, 1(8-9), 786-797.
2. *Optomechanical crystals*
M. Eichenfield, J. Chan, R.M. Camacho, K.J. Vahala and O. Painter
Nature, 2009, 462(7269), 78-82.
3. *Broadband all-photon transduction of nanocantilevers*
M. Li, W.H.P. Pernice and H.X. Tang
Nat Nano, 2009, 4(6), 377-382.
4. *Nanoelectromechanical systems: Nanodevice motion at microwave frequencies*
X.M. Henry Huang, C.A. Zorman, M. Mehregany and M.L. Roukes
Nature, 2003, 421(6922), 496-496.
5. *Cooling a nanomechanical resonator with quantum back-action*
A. Naik, O. Buu, M.D. LaHaye, A.D. Armour, A.A. Clerk, M.P. Blencowe and K.C. Schwab
Nature, 2006, 443(7108), 193-196.
6. *Putting Mechanics into Quantum Mechanics*
K.C. Schwab and M.L. Roukes
Physics Today, 2005, 58(7), 36-42.
7. *Quantum ground state and single-phonon control of a mechanical resonator*
A.D. O'Connell, M. Hofheinz, M. Ansmann, R.C. Bialczak, M. Lenander, E. Lucero, M. Neeley, D. Sank, H. Wang, M. Weides, J. Wenner, J.M. Martinis and A.N. Cleland
Nature, 2010, 464(7289), 697-703.
8. *Laser cooling of a nanomechanical oscillator into its quantum ground state*
J. Chan, T.P.M. Alegre, A.H. Safavi-Naeini, J.T. Hill, A. Krause, S. Groblacher, M. Aspelmeyer and O. Painter
Nature, 2011, 478(7367), 89-92.
9. *Sideband cooling of micromechanical motion to the quantum ground state*
J.D. Teufel, T. Donner, D. Li, J.W. Harlow, M.S. Allman, K. Cicak, A.J. Sirois, J.D. Whittaker, K.W. Lehnert and R.W. Simmonds
Nature, 2011, 475(7356), 359-363.
10. *Towards single-molecule nanomechanical mass spectrometry*
A.K. Naik, M.S. Hanay, W.K. Hiebert, X.L. Feng and M.L. Roukes

11. **Nature Nanotechnology, 2009, 4(7), 445-450.**
Ultra-sensitive NEMS-based cantilevers for sensing, scanned probe and very high-frequency applications
M. Li, H.X. Tang and M.L. Roukes
12. **Nature Nanotechnology, 2007, 2(2), 114-120.**
50 nm thick AlN film-based piezoelectric cantilevers for gravimetric detection
P. Ivaldi and et al.
13. **Journal of Micromechanics and Microengineering, 2011, 21(8), 085023.**
Zeptogram-Scale Nanomechanical Mass Sensing
Y.T. Yang, C. Callegari, X.L. Feng, K.L. Ekinici and M.L. Roukes
14. **Nano Letters, 2006, 6(4), 583-586.**
Noise processes in nanomechanical resonators
A.N. Cleland and M.L. Roukes
15. **Journal of Applied Physics, 2002, 92(5), 2758-2769.**
I. Bargatin, *High-frequency nanomechanical resonators for sensor applications*. 2008, California Institute of Technology.
16. **Efficient and Sensitive Capacitive Readout of Nanomechanical Resonator Arrays**
P.A. Truitt, J.B. Hertzberg, C.C. Huang, K.L. Ekinici and K.C. Schwab
17. **Nano Letters, 2006, 7(1), 120-126.**
In-plane nanoelectromechanical resonators based on silicon nanowire piezoresistive detection
E. Mile, G. Jourdan, I. Bargatin, S. Labarthe, C. Marcoux, P. Andreucci, S. Hentz, C. Kharrat, E. Colinet and L. Duraffourg
18. **Nanotechnology, 2010, 21(16).**
Efficient electrothermal actuation of multiple modes of high-frequency nanoelectromechanical resonators
I. Bargatin, I. Kozinsky and M.L. Roukes
19. **Applied Physics Letters, 2007, 90(9).**
Multifunctional Nanomechanical Systems via Tunably Coupled Piezoelectric Actuation
S.C. Masmanidis, R.B. Karabalin, I. De Vlaminck, G. Borghs, M.R. Freeman and M.L. Roukes
20. **Science, 2007, 317(5839), 780-783.**
Self-Sensing Micro- and Nanocantilevers with Attonewton-Scale Force Resolution
J.L. Arlett, J.R. Maloney, B. Gudlewski, M. Muluneh and M.L. Roukes
21. **Nano Letters, 2006, 6(5), 1000-1006.**
Sensitive detection of nanomechanical motion using piezoresistive signal downmixing
I. Bargatin, E.B. Myers, J. Arlett, B. Gudlewski and M.L. Roukes

- Applied Physics Letters**, 2005, 86(13).
22. *Intrinsic Noise Properties of Atomic Point Contact Displacement Detectors*
N.E. Flowers-Jacobs, D.R. Schmidt and K.W. Lehnert
- Physical Review Letters**, 2007, 98(9), 096804.
23. *Strong Coupling Between Single-Electron Tunneling and Nanomechanical Motion*
G.A. Steele, A.K. Hüttel, B. Witkamp, M. Poot, H.B. Meerwaldt, L.P. Kouwenhoven and H.S.J. van der Zant
- Science**, 2009, 325(5944), 1103-1107.
24. I. Bargatin, *High-frequency nanomechanical resonators for sensor applications*. 2008: California Institute of Technology.
25. *Foundations of Nanomechanics: From Solid-State Theory to Device Applications*
A.N. Cleland and J. Krim
- Physics Today**, 2004, 57(5), 58-59.
26. R. Karabalin, *Nonlinear, coupled, and parametric nanoelectromechanical systems*. 2008, California Institute of Technology.
27. *Modified free vibrating beam method for characterization of effective e_{31} coefficient and leakage resistance of piezoelectric thin films*
E. Defay, C. Zinck, C. Malhaire, N. Baboux and D. Barbier
- Review of Scientific Instruments**, 2006, 77(10), 103903.
28. *Thickness dependence of the properties of highly c-axis textured AlN thin films*
F. Martin, P. Muralt, M.-A. Dubois and A. Pezous
- Journal of Vacuum Science & Technology A: Vacuum, Surfaces, and Films**, 2004, 22(2), 361-365.
29. S. Timoshenko and J.N. Goodier, *Theory of elasticity*. 3d ed. Engineering societies monographs. 1969, New York, : McGraw-Hill. xxiv, 567 p.
30. *Piezoresistance Effect in Germanium and Silicon*
C.S. Smith
- Physical Review**, 1954, 94(1), 42-49.
31. *Efficient electrothermal actuation of multiple modes of high-frequency nanoelectromechanical resonators*
I. Bargatin
- Applied Physics Letters**, 2007, 90(9), 093116.
32. *Self-Transducing Silicon Nanowire Electromechanical Systems at Room Temperature*
R. He, X.L. Feng, M.L. Roukes and P. Yang
- Nano Letters**, 2008, 8(6), 1756-1761.
33. *Optimization of sensitivity and noise in piezoresistive cantilevers*
X. Yu, J. Thaysen, O. Hansen and A. Boisen

- Journal of Applied Physics, 2002, 92(10), 6296-6301.**
34. N.W. Ashcroft and N.D. Mermin, *Solid state physics*. 1976, New York,: Holt. xxi, 826 p.
35. ***Fundamentals of low-noise analog circuit design***
W.M. Leach, Jr.
- Proceedings of the IEEE, 1994, 82(10), 1515-1538.**
36. ***Detecting and characterizing frequency fluctuations of vibrational modes***
Z.A. Maizelis, M.L. Roukes and M.I. Dykman
- Physical Review B, 2011, 84(14), 144301.**

Chapter 3

Nonlinear Mechanics

In order to measure the nonlinear dynamics of NEMS, we have narrowed down our choice of transduction to piezoelectric actuation and piezoresistive detection. We show that the sensitivity and linearity (dynamic range) is sufficient to make accurate measurements of the first order nonlinear stiffness and cross coupling coefficients for three different modes in a nanomechanical beam. We use the measured mode-mode cross-coupling coefficients to make estimates of the viability in measuring quantum transitions of a quantized mechanical state using the tensile interaction in a quantum nondemolition scheme. Finally, using the heating from piezoresistor, we modify the nonlinear stiffness of a doubly clamped beam through deflection. *This work was done in collaboration with Guillermo Villeneuve. The theory for mode cross coupling was adapted from work by John Sader. The predictions for nonlinear stiffness changes were also carried out by John Sader.*

3.1 Introduction

In order to implement nonisochronicity in mechanical oscillators, we use the nonlinearity of a doubly clamped beam. This mechanical structure is well-studied and has simple analytical predictions for the first order corrections of the nonlinear stiffness. This nonlinearity has been exploited in several interesting nonlinear studies [1, 2] and applications [3, 4]. Also, since the predicted minimum frequency noise in mechanical resonators is limited by the amount of nonlinear stiffness [5], its quantitative understanding is crucial for any application [6]. There are also several new ideas [7-9] for using nonlinear tensile coupling between different mechanical modes of the same resonator in order to perform quantum nondemolition (QND) experiments, which was originally proposed for two different resonators with mechanical coupling [10]. Here we attempt to accurately calibrate and find the nonlinear stiffness tensor for the first three modes of a doubly clamped beam. After we have done this, we make predictions for the applicability of this device for QND experiments. Finally, we use the developed methods to explore a quadratic nonlinearity arising in deflected beams. These methods will be useful for the following chapters in which the nonlinear stiffness sets the scale of the nonisochronicity of our feedback oscillators.

3.2 Analytical Prediction for Nonlinear Stiffness in a Doubly Clamped Beam

The flexural motion of a doubly clamped beam causes strain to develop, since the ends are clamped. This additional strain induces tensile stress (through stress-strain relations), which tunes the frequency. This tuning due to amplitude can be modeled as a nonlinear stiffness (for self-tuning) and nonlinear mode coupling (for cross-tuning).

We start by solving for the normal modes of a doubly clamped beam. The mode solutions are given by (more detail on how to find this solution can be found in Chapter 2 or reference [11])

$$\Phi_n(\xi) = Q_n \left(\cosh \kappa_n \xi - \cos \kappa_n \xi + \frac{\cosh \kappa_n - \cos \kappa_n}{\sinh \kappa_n - \sin \kappa_n} [\sin \kappa_n \xi - \sinh \kappa_n \xi] \right), \quad (3.1)$$

where ξ is normalized distance along the beam, and Q_n is the n th mode's amplitude

normalization constant, and κ_n is defined in equation (2.7). We now move to Euler-Bernoulli equation under tensile stress. This is

$$\frac{\partial^2 u_2}{\partial t^2} + \gamma^2 \frac{\partial^4 u_2}{\partial \xi^4} - \overbrace{\gamma^2 \frac{A}{I} \left(\frac{Tl^2}{Y} + \frac{1}{2} \int_0^1 \left(\frac{\partial u_2}{\partial \xi} \right)^2 d\xi \right)}^{\text{tensile correction}} \frac{\partial^2 u_2}{\partial \xi^2} = 0, \gamma^2 = \frac{YI}{\mu l^4}, \quad (3.2)$$

where μ is the linear mass density in the direction of the beam, and the other variable are the same as in chapter two. The middle term is the correction for stress within the beam. Here T is the static part to the stress. The other term in the brackets is the stress due to extension along the length of the beam.

For a beam we know we can decompose the motion into the normal modes with

$$u_2(\xi, t) = \sum_n \mathcal{A}_n \Phi_n(\xi) \zeta_n(t). \quad (3.3)$$

Thus substituting equation (3.3) into equation (3.2), we get

$$\begin{aligned} \sum_n \mathcal{A}_n \ddot{\zeta}_n + \gamma^2 \sum_n \mathcal{A}_n \zeta_n^{IV} - \gamma^2 \frac{A}{I} \sum_n \mathcal{A}_n \zeta_n \left(\frac{Tl^2}{Y} + \frac{1}{2} \int_0^1 \left(\sum_n \mathcal{A}_n \zeta_n' \right)^2 d\xi \right) &= 0, \end{aligned} \quad (3.4)$$

For two modes this gives

$$\ddot{\zeta}_k + \omega_{k,0}^2 \zeta_k + \eta_k \omega_{k,0}^2 \zeta_k \left[X_{kk} \frac{Tl^2}{Y} + \frac{1}{2} \mathcal{A}_k^2 \zeta_k^2 X_{kk}^2 + \mathcal{A}_j^2 \zeta_j^2 \left(\frac{X_{kk} X_{jj}}{2} + X_{jk}^2 \right) \right] = 0, \quad (3.5)$$

where $\eta_k = \frac{A}{l} \frac{1}{\int_0^1 \Phi_k \Phi_k^{IV} d\xi}$, $X_{nm} = \int_0^1 \Phi_n' \Phi_m' d\xi$, $\omega_{k,0}^2 = \int_0^1 \Phi_k \Phi_k^{IV} d\xi * \gamma^2$.

The resonant frequency is modified by the intrinsic stress,

$$\omega_{k,t}^2 = \omega_{k,0}^2 \left(1 + \eta_k X_{kk} \frac{Tl^2}{E} \right), \quad \tau_k = \frac{\eta_k}{1 + \eta_k X_{kk} \frac{Tl^2}{E}}. \quad (3.6)$$

According to reference [12], the modified frequency from only the dynamic resonant tensile terms is

$$\omega_{k,mod}^2 = \omega_{k,t}^2 (1 + 2\lambda_{kk} \mathcal{A}_k^2 + 2\lambda_{jk} \mathcal{A}_j^2). \quad (3.7)$$

with coupling coefficients

$$\lambda_{jk} = (2 - \delta_{jk}) \frac{\tau_j}{8} \left(\frac{X_{kk} X_{jj}}{2} + X_{jk}^2 \right). \quad (3.8)$$

Thus, the change in frequency for mode k is

$$\frac{\Delta\omega_k}{\omega_k} = \lambda_{jk} \mathcal{A}_{max,j}^2, \quad (3.9)$$

assuming that only mode j is driven to high amplitudes. These coefficients λ_{jk} form the nonlinear stiffness tensor which relates change in frequency and amplitude of resonant motion. The

diagonal components are well-known “Duffing” terms. The off-diagonal components are coupling between two different modes.

3.3 Transduction Nonlinearity

In order to accurately measure the nonlinear stiffness of beams, the mechanical amplitudes must be accurately calibrated. Other studies [7, 9] use actuation efficiencies in order to calibrate the mechanical amplitudes. These, however, depend on the ability to accurately model the actuation (including the actuation nonlinearities), which can vary widely from device to device. Here we use the extreme linearity and moderate sensitivity of the metallic piezoresistive sensing from the last chapter in order to measure the nonlinearity. In Figure 3.1, we sketch the basic idea. The beam measured in this experiment is shown in Figure 3.1 (a). In Figure 3.1 (b), we show a diagram for how the thermomechanical motion is measured (with a background noise set by the transducer noise and amplifier noise while the switch is set to a 50Ω resistor). After this, the device is driven with the output signal measured (with the switch set to a signal source). The thermomechanical motion is Brownian motion of a particle in harmonic potential (a well understood physical phenomena with a simple mathematical expression), giving the calibration a firm foundation. However, the electronic output can only be calibrated to this mechanical motion given that both the transducer and amplifier stages stay linear. The transducer here can be electronic, optical, mechanical, etc.

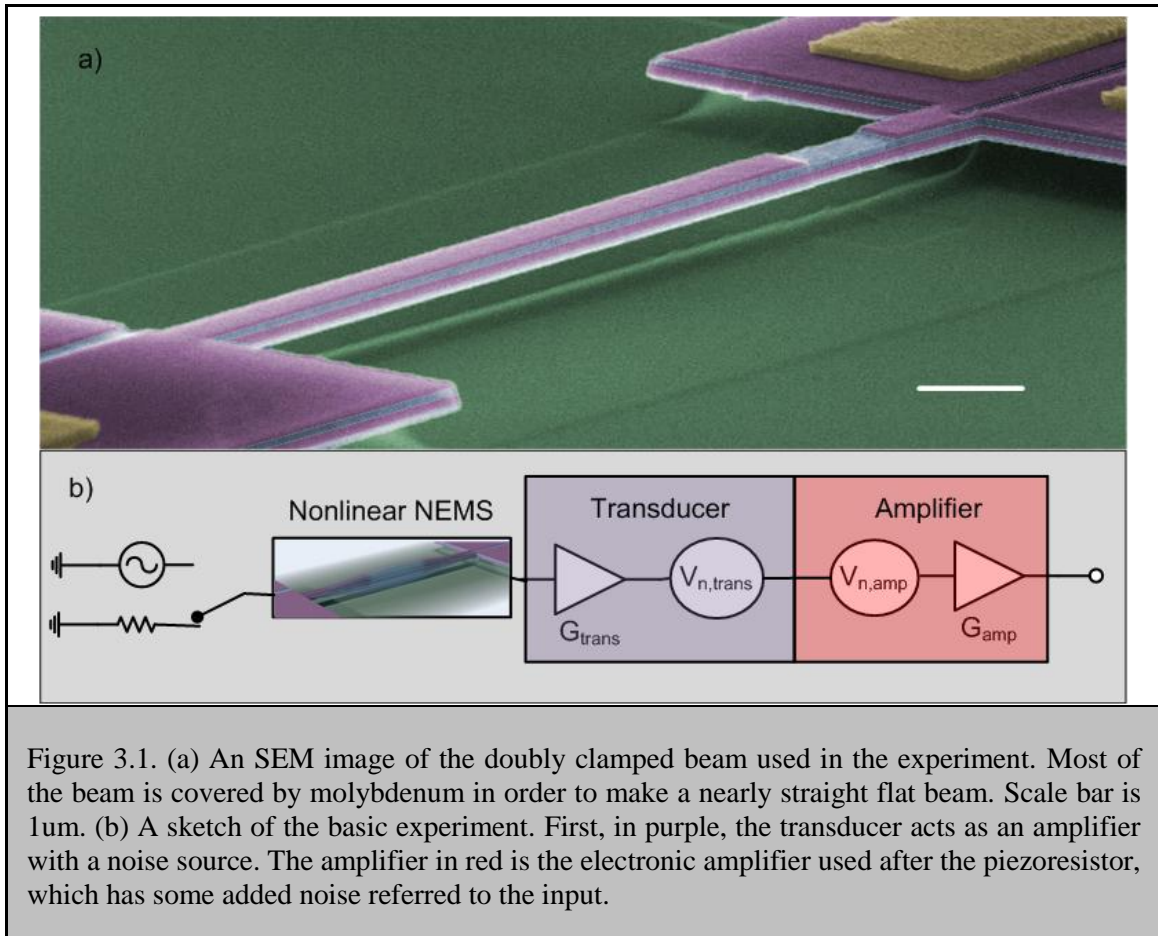
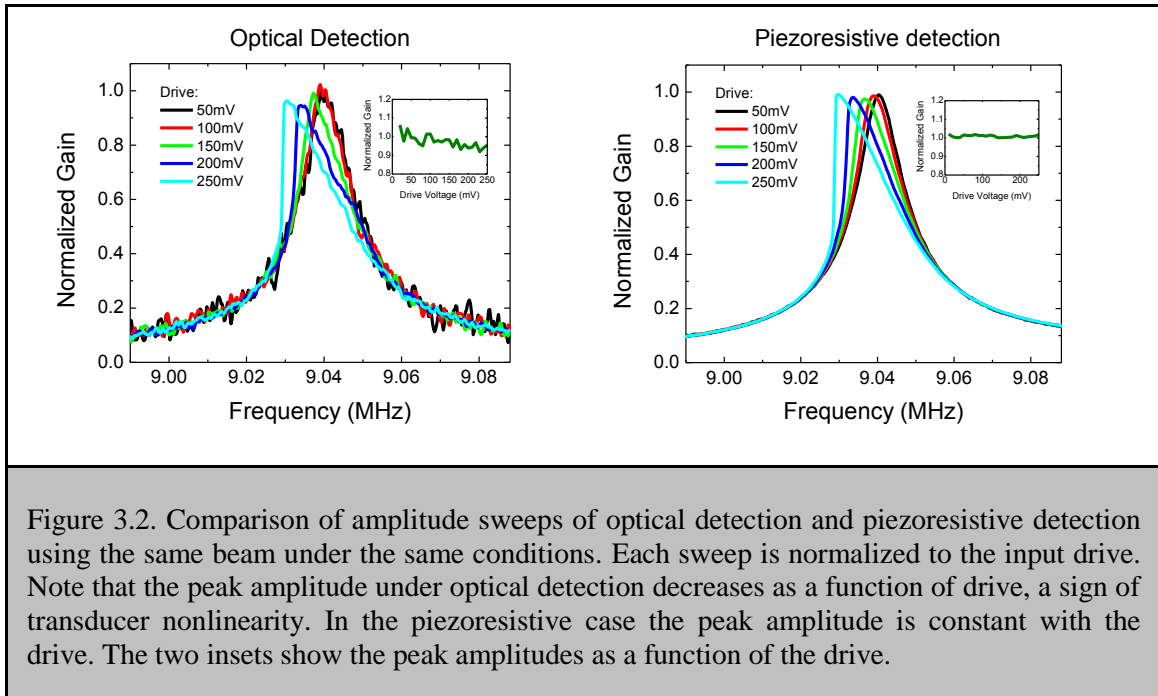


Figure 3.1. (a) An SEM image of the doubly clamped beam used in the experiment. Most of the beam is covered by molybdenum in order to make a nearly straight flat beam. Scale bar is 1 μm . (b) A sketch of the basic experiment. First, in purple, the transducer acts as an amplifier with a noise source. The amplifier in red is the electronic amplifier used after the piezoresistor, which has some added noise referred to the input.

We show the difference between a linear and nonlinear transducer in Figure 3.2, in which we take the same beam and measure both optically and piezoresistively under the same drive conditions. We divide the output signals by the drive (total gain) and normalize them to the 50mV drive level. The insets show the peak height versus the drive level. In both cases, the amplitude should be the same. However, there is a clear loss of detection efficiency in the optical case. In this optical case, it might be impossible to distinguish intrinsic from detection nonlinearity when using optical interferometry



We therefore use the piezoelectric/piezoresistive transduction scheme to measure the geometric nonlinear effects in a nearly ideal doubly clamped beam (shown in Figure 3.1 (a)), with dimensions $length \times width \times thickness = 9\mu\text{m} \times 470\text{nm} \times 210\text{nm}$ (Stack II, Appendix II). We use FEM simulation to find the effective masses for the first three out-of-plane modes, which slightly differ from the theoretically derived effective masses for a perfectly clamped, rectangular beam, primarily due to a 500 nm ledge originating from the fabrication process. We first observe the spectral response in a narrow range around the resonant frequency given an applied piezoresistive bias voltage of 100mV. We observe a flat white noise in addition to a small Lorentzian peak centered at the resonance frequency Figure 3.3 (a, bottom) and fit as described in the last chapter. For the first mode, we find a flat noise background referred to input of about $0.86\text{nV}/\text{Hz}^{1/2}$ as shown in green (Figure 3.3 (a, bottom), green line). Its level is consistent with the Johnson white noise generated by the finite resistance of the 70 Ohm piezoresistive loop combined with noise from the first stage amplifier (see section 2.7). We note that even though our background noise is

more than an order of magnitude higher than our thermomechanical noise, we are still able to measure the thermomechanical noise. With infinite averaging time any size background white noise does not pose a problem for this measurement. However, due to system and device parameter drifts, the available averaging time is limited. Therefore, the detection scheme must be sensitive enough to measure the noise within the timescale of the drift of the overall system.

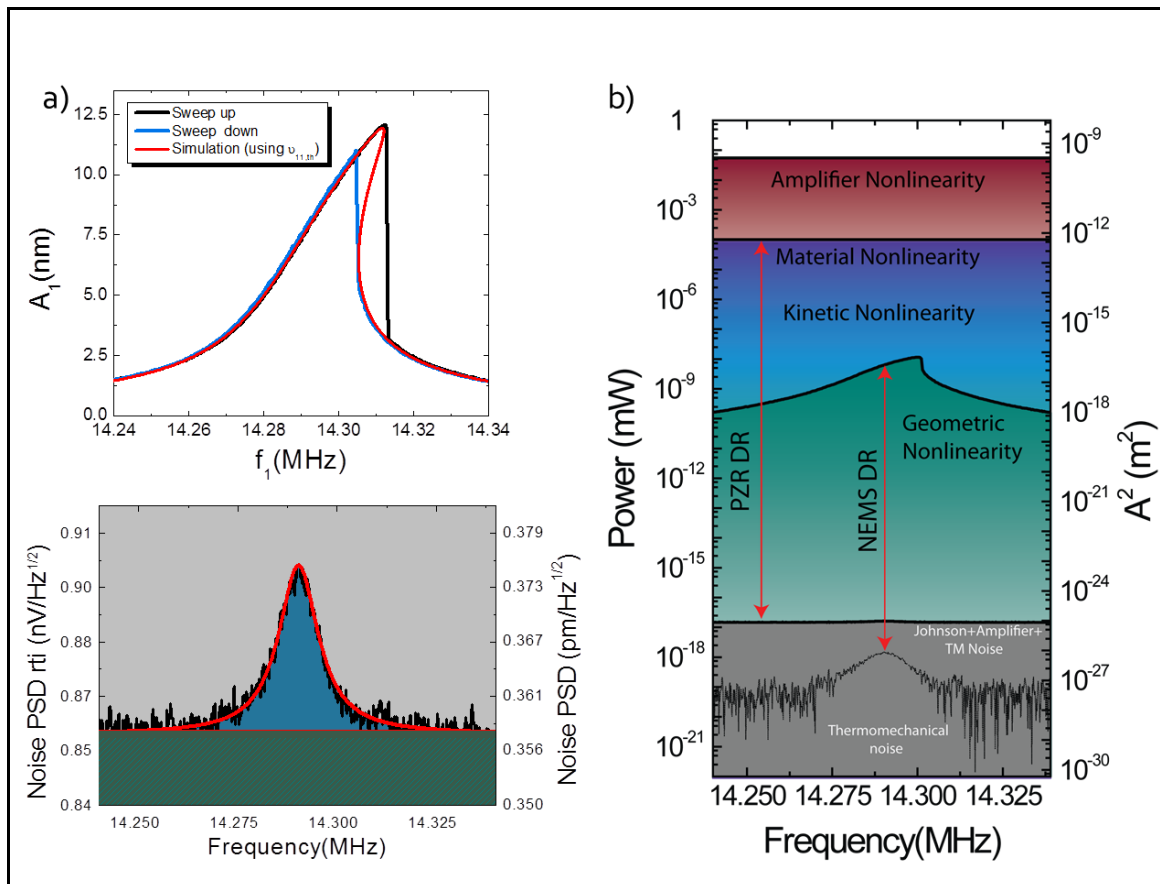


Figure 3.3. (a, Bottom) Noise referred to the input of the first stage electronic amplifier. Black is the raw data. Light green line is the fitted Johnson noise background, red the Lorentzian fit for the thermomechanical noise. (a, Top) Driven response of the system above critical amplitude. Black line is sweeping frequency up, blue is sweeping frequency down. Red line is theoretical simulation using resonant frequency and quality factor from thermomechanical noise data and nonlinear stiffening from Euler-Bernoulli equation. (b) Overall dynamic range for the system. The left axis is the power referred to the input of the amplifier. The right axis is the maximum square displacement of the device. The area below the noise floor of the system is shown in grey. Black line separating grey area from green area is total output noise. Dotted line is the thermomechanical noise after flat white noise background subtraction. Green area is real dynamic range of nanomechanical system, with the noise floor set by the electromechanical transduction and the amplifier noise floor, and the ceiling set by the critical amplitude of the device. Blue area represents the range where kinetic (inertial) nonlinearities should arise. Purple represents the region where material nonlinearities become important. Red is region where amplifier nonlinearity becomes important. Note that the piezoresistive (PZR) dynamic range is much larger than the NEMS DR.

With the noise measurement, we correlate the voltage from the open loop driven response to the RMS temporal mean displacement of the beam as long as the electromechanical transduction and amplification in the detection circuit are linear. Shown in Figure 3.3 (b) are the relevant dynamic ranges for this nanomechanical system. The left axis is the power referred to the input of the amplifier, and the right axis is the maximum square displacement of the NEMS device. The geometric-stiffness dynamic range (green region) is limited as the amplitude approaches the thickness dimension (divided by \sqrt{Q}) for the beam. If we were to use a singly clamped beam, then typically a kinetic (inertial) nonlinearity is the limit of the dynamic range [13], when the amplitude approaches the length dimension of the beam (teal region). If this resonator was driven in a bulk mode, material nonlinearity (taken from the transition from elasticity to plasticity $\epsilon \sim 10^{-2}$) can be the limit (purple region). The piezoresistive detection is typically an effect induced by linear stress-strain relations, and is therefore limited by material nonlinearity. This sets the limit for our transduction linearity. In our measurement, we use electronic amplifiers with compression amplitudes well above material nonlinearity (red region). This graph clearly shows

that the nonlinear compression point of our transduction (found from estimates on the breakdown of stress-strain relations, i.e., material nonlinearity) and amplification circuitry (found from the amplifier power compression) is 4-5 orders of magnitude above the mechanical nonlinearity of interest. Also, if we wish to explore inertial nonlinearities dominant in other geometries, it should still be possible using this setup.

Before proceeding further, we present our method for determining the intrinsic stress in the beam ('T' in equation (3.6)), since the nonlinearity has a stress dependence. We estimate the average tension in the beam by comparing the measured mode frequencies to the simulated values. These must be simulated since the mode frequencies are highly sensitive to the size of the ledge (which comes from surface micromachining, suspending the NEMS). Since multiple modes can be actuated through the piezoelectric mechanism, both in-plane modes and out-of-plane modes are found. The mode frequencies are listed in Table 3.1. Based on this analysis, we estimate an average beam tensile stress of 67.5 ± 2.5 MPa.

1 st out of plane	1 st in plane	2 nd out of plane	3 rd out of plane	2 nd in plane	4 th out of plane
14.26 MHz	31.9 MHz	37.9 MHz	71.5 MHz	86.9 MHz	116 MHz

Table 3.1. Frequencies of the first 4 out-of-plane and first 2 in-plane modes of the 10 μ m beam.

Given that we can now estimate the nonlinear coefficients, care must be taken that the transduction does not perturb or obfuscate the mechanical system, as in the case of capacitive detection. For example, in the study by Kacem et al.[14], the electromechanical nonlinear response was altered due to the capacitive nonlinearity. In Figure 3.3 (a,top), we compare the

theoretical estimate for the frequency sweep with geometric tensile nonlinearity to the experimental result for mode 1. The vertical lines indicate unstable points where the amplitude from the upper solution jumps to a lower solution, or vice versa. It is obvious from the plot that for this mode and drive level, the theoretical value for the mechanical nonlinearity accurately predicts the behavior of the system.

3.4 Measurement of the Nonlinear Stiffness Tensor

In order to extract the experimental values for the nonlinear stiffness tensor, we perform two experiments. We first extract the diagonal elements (λ_{jj}). Then, by monitoring frequency shifts in one mode due the tension induced by large amplitudes in other modes, we find the nonlinear coupling between modes in terms of frequency shifts such that

$$\frac{\Delta\omega_k}{\omega_k} = \widetilde{\lambda}_{jk} \frac{\Delta\omega_j}{\omega_j}, \quad (3.10)$$

where $\widetilde{\lambda}_{jk}$ is the coupling coefficient in terms of relative frequency shift. We can apply equation (3.9) for mode j (using λ_{jj}) to obtain λ_{jk} .

To determine the diagonal coefficients, we sweep the drive frequency and step the amplitude using the experimental setup in Figure 3.4 (a), using only the network analyzer (without external source f_d) and no phase locked loop control. The peak amplitudes fit according to equation (2.5)(linear fit of Figure 3.4 (b,top)). We then check frequency shifts of the other modes. In this example, we use an external drive to excite the second resonant mode, and measure the frequency shift of the third resonant mode with a software phase locked loop implemented in the network analyzer. Figure 3.4 (b,bottom) shows the shift of the third mode when the second mode is driven at high amplitudes, giving us behavior described by equation (3.3). We keep the amplitude of the

third mode well below the critical amplitude so that tension from mode three does not affect the result. By comparing the slopes of the fits in Figure 3.4 (b) we extract the off-diagonal element λ_{23} .

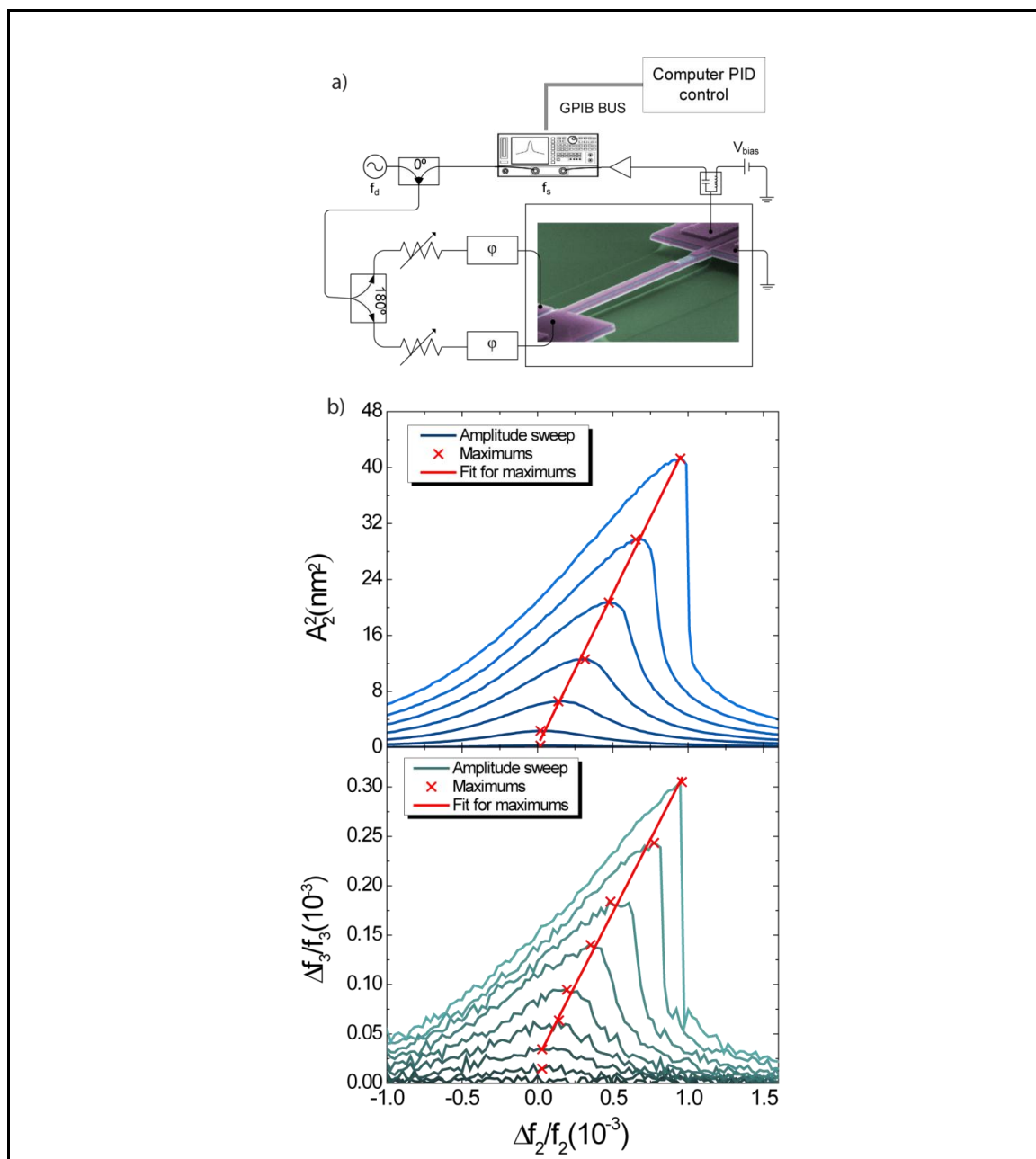


Figure 3.4. (a) Circuit diagram for measurement of nonlinear stiffness coefficients. Two different experiments are conducted. First, the PID loop and the source f_d are not used and the system is swept with frequency and amplitude, with the response measured (b, top). Afterwards, the original frequency used for the first experiment is swept using external source at f_d and the network analyzer is locked to the phase response of a different mode (b, bottom). Measuring the slopes of the linear fits of the upper graph gives in this case gives λ_{22} . Using the slopes from both graphs gives λ_{23} .

The nonlinear stiffness tensor is presented below in Table 3.2. Uncertainties for the theoretical results (shown in parenthesis) taken from error in the tension are much smaller than uncertainties those from the experimental fitting error. Uncertainties in experimental results are determined using the linear fits similar to the example in figure 3 (b).

$\lambda(10^{-5}\text{nm}^{-2})$	Driven 1	Driven 2	Driven 3
Sensed 1	0.53 ± 0.01 (0.53)	1.76 ± 0.36 (1.45)	3.51 ± 0.47 (3.59)
Sensed 2	0.18 ± 0.01 (0.186)	1.16 ± 0.03 (1.16)	1.77 ± 0.13 (1.65)
Sensed 3	0.13 ± 0.01 (0.124)	0.35 ± 0.06 (0.445)	1.43 ± 0.07 (1.43)

Table 3.2. Measured (Simulated) nonlinear stiffness coefficients for the first three modes of the beam. Uncertainties are found from a combination of the uncertainty of linear fits in Figure 3.4 (b) and from uncertainties in amplitude conversions from thermomechanical noise fits (Figure 3.3 (b, bottom)).

The uncertainty is larger in the off-diagonal modes, due to large amounts of noise in the experiment. In order to reduce the SNR in Figure 3.4 (b, bottom), the experiments for the off-diagonal components take much longer than the amplitude sweeps, since the measurement is taken through a phase locked loop with an integration time $\sim 100\text{ms}$. Thus each point on a curve

in (4.5)(b,bottom) takes on the order of a couple seconds to take. For these reasons a measurement for a single mode can take ~hours, through which the frequency of both the sensed and driven mode can drift. If we try to reduce the drift by taking the measurements in a shorter time period, frequency noise of the ‘detected mode’ becomes large compared to the signal from the sensed mode. The SNR of the mode-mode coupling method is smaller than the simple “Duffing” measurements since the mode coupling is relatively weak. There is a careful balance of noise and drift at work.

The deviation of the measured λ_{23} coefficient from the theoretical value is outside the uncertainty. The uncertainty of λ_{21} is also very large, so agreement between theory and experiment is not very convincing. The middle column of Table 3.2 is for sweeps where mode 2 is driven to large amplitudes. It is possible that mode interactions (which hinges on the premise that mode shapes can be predicted precisely by equation (3.1)) cannot be accurately modeled for mode 2. The presented theory is for an ideal beam without clamps, and therefore, still achieves excellent agreement. This validates both the measurement technique and Euler-Bernoulli beam theory for beams ~100nm.

3.5 Quantum Nondemolition Predictions

We can make some predictions for quantum nondemolition (QND) experiments for this beam. The basic idea of QND measurements is to measure quantum signatures using detection operator that commutes with the Hamiltonian of the system (in this case a harmonic oscillator). The square of the amplitude satisfies this property. This beam frequency is low, so it is assumed that cavity backaction cooling will have to be employed in order to detect quantum states with $\hbar\omega \sim k_b T$. We assume that the rest of the system is at a bath temperature of 20mK. For this we

construct Table 3.3 based on these predictions. Here the amplitude $k_b T / m\omega^2$ is the integrated amplitude around the mode at $k_b T = \hbar\omega$.

Mode number	T (mK)	$\mathcal{A}^2(m^2)$	$\frac{\Delta f_1}{f_1}$	$\frac{\Delta f_2}{f_2}$	$\frac{\Delta f_3}{f_3}$	$\frac{\delta f}{f}$
1	0.7	4.0×10^{-28}		7.2×10^{-16}	5.2×10^{-16}	5.9×10^{-9}
2	1.8	1.4×10^{-28}	2.5×10^{-15}		4.9×10^{-16}	2.3×10^{-9}
3	3.5	8.3×10^{-29}	2.9×10^{-15}	1.4×10^{-15}		1.4×10^{-9}

Table 3.3. Predictions for QND experiments using this beam. The second column is the temperature the mode has to be in order to reach the ground state. The next column is the square amplitude of the device at peak at that temperature in the previous column. The next three columns show how much fractional frequency deviation will this mode cause in other modes. The rightmost column is the minimum observable frequency resolution taken from reference [6] with a bath temperature of 20mK. Detecting quantum states in this manner is not possible since the last column is 6 orders of magnitude larger than the previous three columns.

Note that this theoretical measurement favors sensing lower mode frequencies and seeing the quantum jumps of higher modes. Practically speaking, this is also favored, since detection of lower frequencies is in general easier, and higher modes have less extreme requirements on temperature. In fact, if we used beam with a frequency a mode at ~1GHz, cryogenic cooling would be sufficient to reach quantum ground states. We also compare these values to the minimum observable frequency resolution [6]. The level of frequency noise required to measure quantum ‘jumps’ is six orders of magnitude lower than what is possible with this beam.

These are extremely low signals to detect, even for systems at low temperatures. We estimate that, assuming this theory scales to ~1nm of thickness for the beam, quantum jump $\frac{\delta f}{f}$ would be at best $\sim 10^{-9}$. On a beam of this thickness, the dynamic range decreases to almost zero, so we cannot make estimates on the frequency noise. However, atomically thin structures lose their areal moments (become string-like) and the nonlinearity decreases from ~thickness to ~length. As

such, both ‘frequency noise’ and nonlinearity experiments will have to be performed on these kinds of devices before estimates can be made at the truly ‘nano’ level.

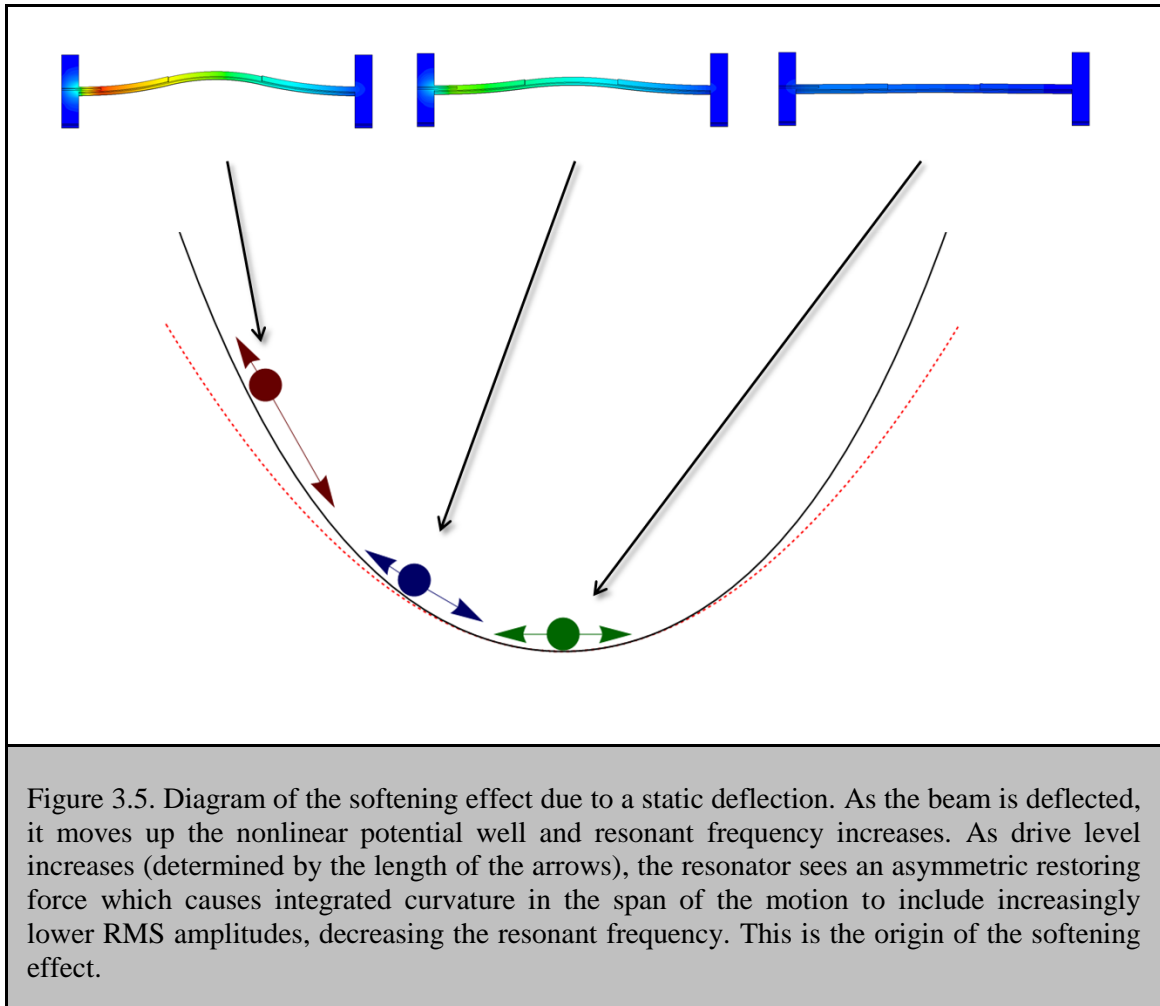
3.6 Nonlinearity Tuning through Beam Deflection

Controlling nonlinearity in mechanical structures could be important for sensing and applications, as mentioned in the introduction to the chapter. In Figure 3.2, the data is not accurately predicted by the beam theory described in sections 3.2, since the nonlinear stiffness coefficient is negative.

This change of nonlinearity is induced by a static deflection of the beam. If we introduce a static force into the equation of motion, it is the same as adding a linear term to the harmonic oscillator potential. This term breaks the symmetry of the potential well, and thus the restoring force prefers to push only one way, and on average reduces the effective nonlinearity[15].

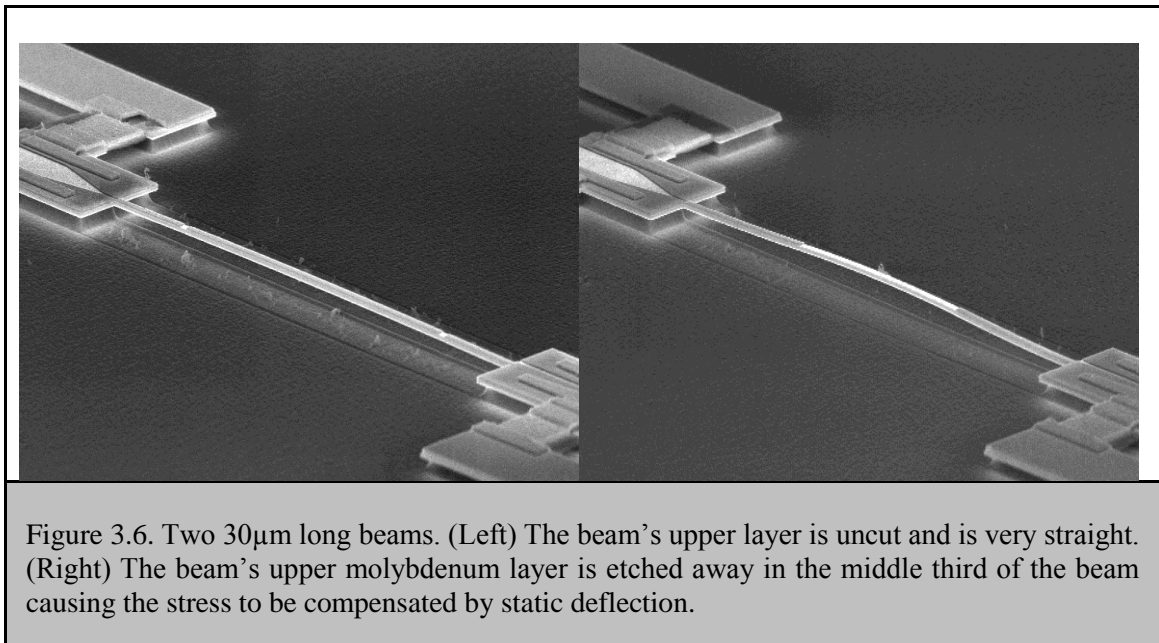
In Figure 3.5, we offer a diagram of this effect. An undeflected beam will sit at the bottom of the well (green ball). The frequency is determined by the integral of the curvature within the span of the motion (green arrow). As the beam is deflected, it moves up the nonlinear potential well (black line) of the resonator (which has fourth order term due to the tensile nonlinearity). At higher points in the potential well, the symmetry of restoring force acting back on the resonator will be broken (arrow length for left and right directions in Figure 3.5). Also, at these higher points, since the well is nonlinear, the resonant frequency will be higher (the ‘linear’ potential well is shown with the red dotted line), since the curvature has a term which depends on position. As the resonant drive is increased for a given deflection (i.e., for the red ball in figure 3.5), the integrated curvature includes larger spans tending toward the bottom of the well (bottom red arrow), effectively reducing the frequency. This causes a ‘softening’ effect on the nonlinearity,

since this is an amplitude dependent reduction in frequency. Hence, it is the hardening tensile nonlinearity itself (the fourth order term in the well) which causes this softening nonlinear term to appear. In cantilevers (singly-clamped beams), this effect is not as pronounced, since the amplitude-frequency nonlinearities are much smaller in those systems.

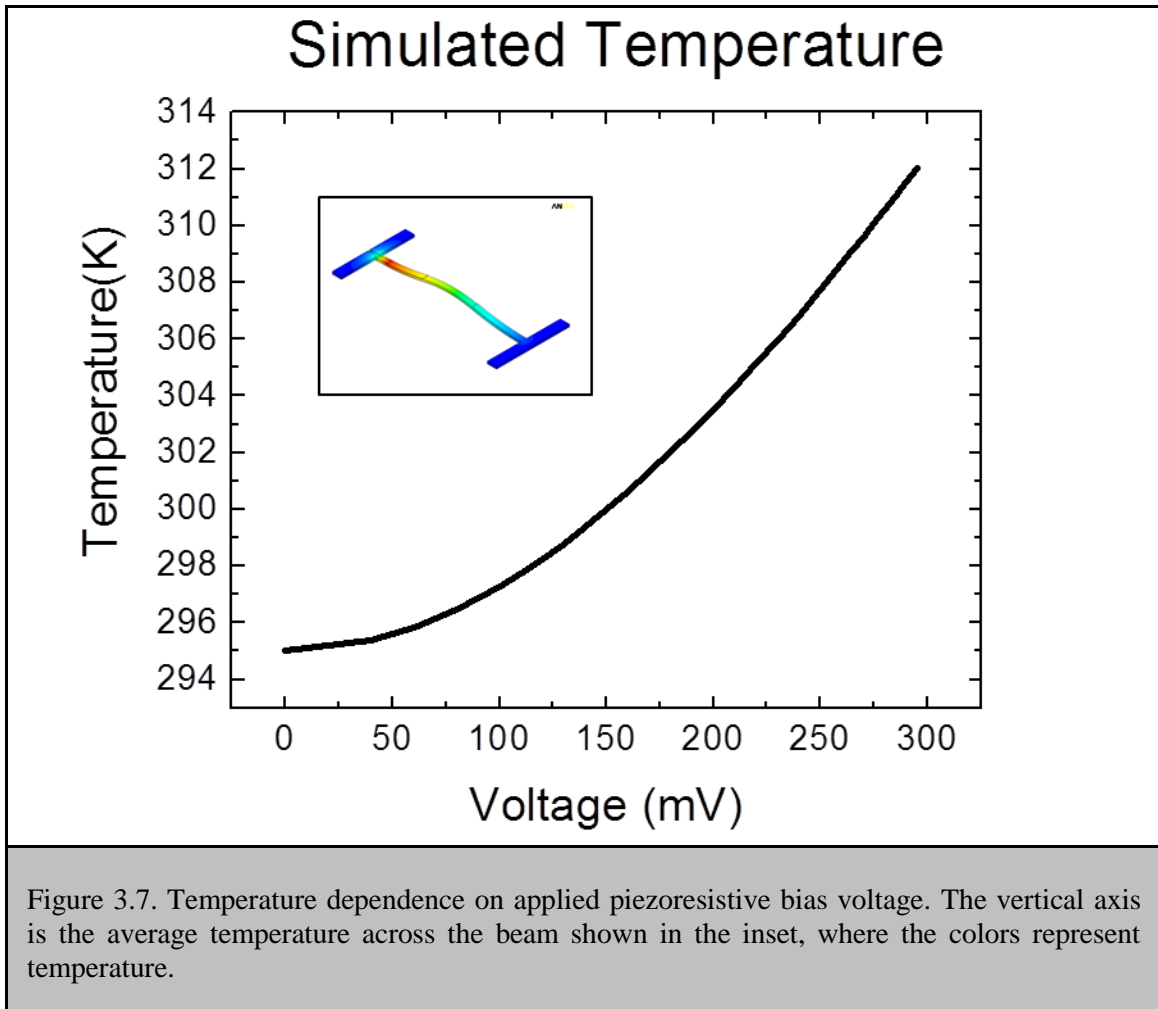


In our wafers, the stress in the piezoelectric stack is compensated, such that the aluminum nitride and molybdenum have no net stress across the thickness of the beam. However, when the top layer of molybdenum of the wafer stack on the beam is completely or partially removed, the

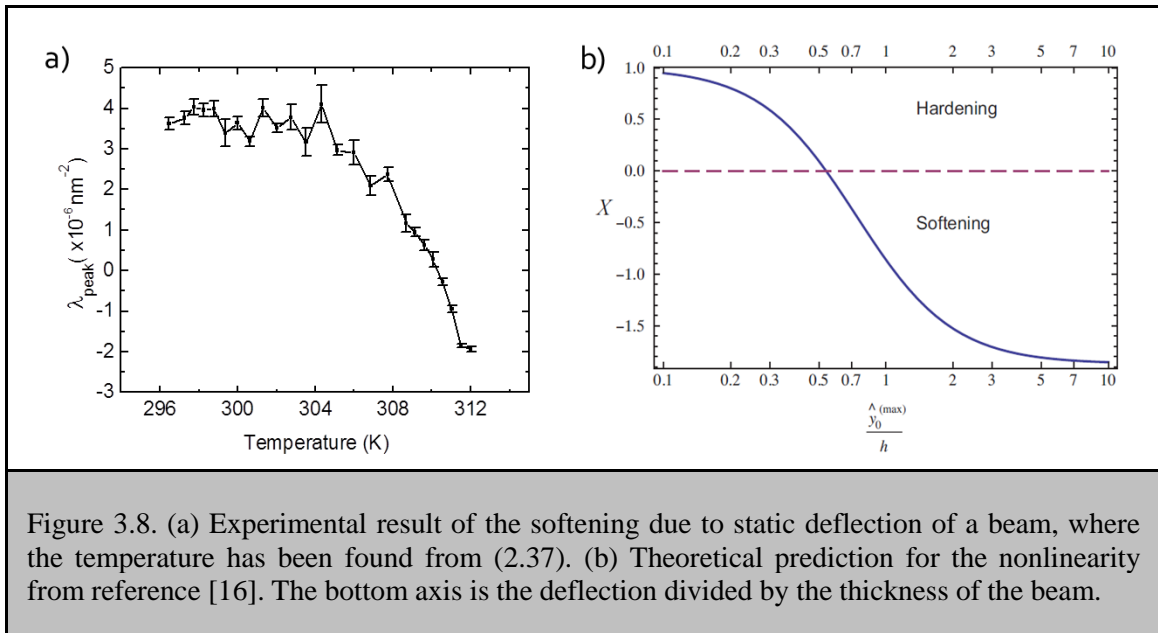
stress is no longer compensated. As a result, a net torque, which statically deflects the beam, is developed. In Figure 3.6 (left), the beam is essentially uncut, and remains straight. In the image (Figure 3.6 (right)), the middle third of the top layer is removed, causing the deflection of the beam. We can increase the deflection of the beam by thermal heating through the piezoresistive bias since the coefficient of thermal expansion is different for the two materials.



We use the same method for calibrating the nonlinearity of a deflected beam as described in section 3.3. In this case, since we modify the temperature of the piezoresistor, we change the nonlinearity through deflection. FEM is used to simulate how much the temperature would increase under the applied voltage bias, since it is important for calculating thermomechanical rms amplitudes. In Figure 3.7, we show how the average temperature across a beam of dimensions $12\mu\text{m} \times 0.5\mu\text{m} \times 0.21\mu\text{m}$ (Stack II, Appendix II), with the middle section of top molybdenum cut, depends on applied voltage bias.

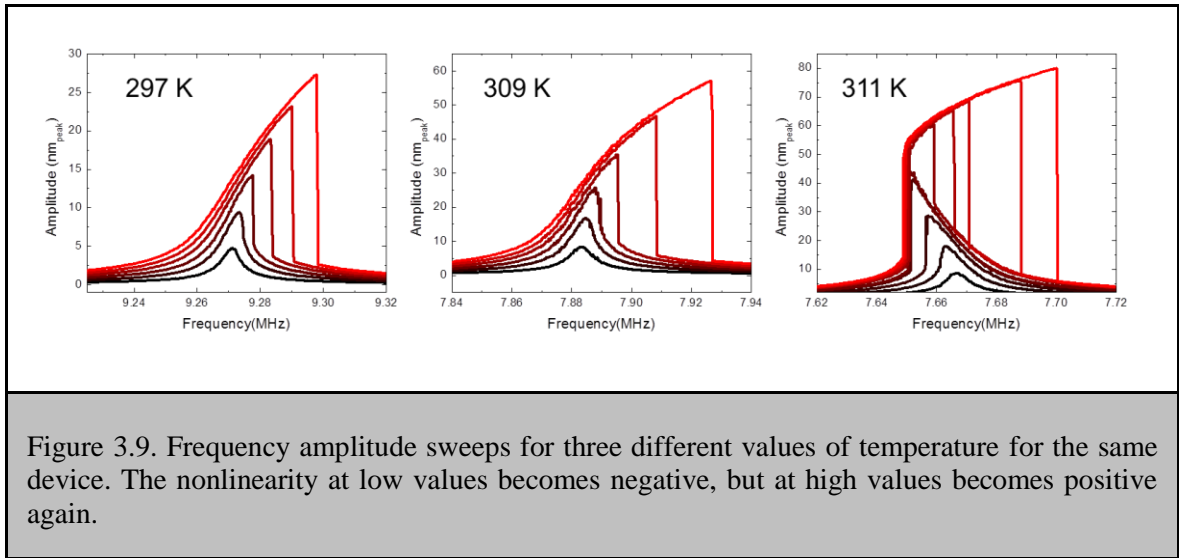


The experimental data is shown in Figure 3.8 (a). Here the nonlinearity is relatively constant for lower values and then drastically decreases in a small range of temperatures. If we assume the deflection is linear in temperature in this range, then the change in nonlinearity has basically the same functional form. In Figure 3.8 (b), we show the prediction from reference [16]. It is difficult to quantitatively compare the theory to the experiment since we do not know static beam deflection *in situ*. Also, it is challenging to simulate the deflection since the thermal expansion coefficients for these thin film materials might deviate from reported bulk values.



For drive levels with resonant amplitudes much larger than the static deflection, the integrated curvature of the potential well will effectively be the same as an undeflected beam, and thus this effect is destroyed.

In Figure 3.9 we show three sweeps of amplitude at different effective temperatures. Take note of the vertical scale of these plots, since it increases from left to right. In the first one (297K), the nonlinearity is close to what is expected from beam theory. The second (309K) shows a reduced nonlinearity at low amplitudes. The third (311K) shows a true softening nonlinearity at low amplitudes followed by a flip to hardening nonlinearity at larger values of amplitude.



3.7 Future Work

This chapter is important in determining the nonlinear coefficient for fundamental limits on sensing [6],[17],[18, 19] and for QND [20] experiments, especially since the rise of atomically thin [21, 22] mechanical devices. Also, new applications can be imagined, using the nonlinear coupling between different modes as a transducer. In section 3.3, we showed detection of one mode using another mode. This could be used to detect modes that are electrically (or optically) inaccessible, but coupled mechanically [23] to other modes which are electrically accessible. This could have applications in sensing technology, since high frequency modes can be difficult to detect (see chapter 2). Also, nonlinearities that are not predicted theoretically such as nonlinear damping, or nonlinear stiffness from complex mechanical structures, could be found with the methods presented.

Bibliography

1. ***Basins of Attraction of a Nonlinear Nanomechanical Resonator***
I. Kozinsky, H.W.C. Postma, O. Kogan, A. Husain and M.L. Roukes
Physical Review Letters, 2007, 99(20), 207201.
2. ***Response of parametrically driven nonlinear coupled oscillators with application to micromechanical and nanomechanical resonator arrays***
R. Lifshitz and M.C. Cross
Physical Review B, 2003, 67(13), -.
3. ***Signal amplification in a nanomechanical Duffing resonator via stochastic resonance***
R. Almog, S. Zaitsev, O. Shtempluck and E. Buks
Applied Physics Letters, 2007, 90(1), 013508-3.
4. ***Evading amplifier noise in nonlinear oscillators***
D.S. Greywall, B. Yurke, P.A. Busch, A.N. Pargellis and R.L. Willett
Physical Review Letters, 1994, 72(19), 2992-2995.
5. ***Noise processes in nanomechanical resonators***
A.N. Cleland and M.L. Roukes
Journal of Applied Physics, 2002, 92(5), 2758-2769.
6. ***Ultrasensitive nanoelectromechanical mass detection***
K.L. Ekinici, X.M.H. Huang and M.L. Roukes
Applied Physics Letters, 2004, 84(22), 4469-4471.
7. ***Nonlinear Modal Interactions in Clamped-Clamped Mechanical Resonators***
H.J.R. Westra, M. Poot, H.S.J. van der Zant and W.J. Venstra
Physical Review Letters, 2010, 105(11), 117205.
8. ***Anharmonic modal coupling in a bulk micromechanical resonator***
T. Dunn, J.S. Wenzler and P. Mohanty
Applied Physics Letters, 2010, 97(12), -.
9. A. Gaidarzhy, J. Dorignac, G. Zolfagharkhani, M. Imboden and P. Mohanty, *Energy measurement in nonlinearly coupled nanomechanical modes*. Vol. 98. 2011: AIP. 264106.
10. ***Quantum nondemolition measurement of Fock states of mesoscopic mechanical oscillators***
D. Santamore, A. Doherty and M. Cross
Physical Review B, 2004, 70(14).
11. A.N. Cleland, *Foundations of nanomechanics : from solid-state theory to device applications*. 2003, Berlin ; New York: Springer. xii, 436 p.
12. J.E. Sader, *Nonlinear Tuning of Resonant Frequency of Elastic Beams*. 2009. p. 8.

13. *50 nm thick AlN film-based piezoelectric cantilevers for gravimetric detection*
P. Ivaldi and et al.
Journal of Micromechanics and Microengineering, 2011, 21(8), 085023.
14. *Bifurcation topology tuning of a mixed behavior in nonlinear micromechanical resonators*
N. Kacem and S. Hentz
Applied Physics Letters, 2009, 95(18), 183104.
15. R. Lifshitz and M.C. Cross, *Nonlinear Dynamics of Nanomechanical and Micromechanical Resonators*. Reviews of Nonlinear Dynamics and Complexity. 2009: Wiley-VCH Verlag GmbH & Co. KGaA. 1-52.
16. *Effect of Initial Deflection on the Nonlinear Response of Nanoelectromechanical Resonators*
J.E. Sader
Unpublished Work, 2010.
17. *Ultra-sensitive NEMS-based cantilevers for sensing, scanned probe and very high-frequency applications*
M. Li, H.X. Tang and M.L. Roukes
Nature Nanotechnology, 2007, 2(2), 114-120.
18. *Ultimate and practical limits of fluid-based mass detection with suspended microchannel resonators*
J. Arlett
Journal of Applied Physics, 2010, 108(8), 084701.
19. *Self-Sensing Micro- and Nanocantilevers with Attonewton-Scale Force Resolution*
J.L. Arlett, J.R. Maloney, B. Gudlewski, M. Muluneh and M.L. Roukes
Nano Letters, 2006, 6(5), 1000-1006.
20. *Anharmonic effects on a phonon-number measurement of a quantum-mesoscopic-mechanical oscillator*
D. Santamore, H.-S. Goan, G. Milburn and M. Roukes
Physical Review A, 2004, 70(5).
21. *Electromechanical Resonators from Graphene Sheets*
J.S. Bunch, A.M. van der Zande, S.S. Verbridge, I.W. Frank, D.M. Tanenbaum, J.M. Parpia, H.G. Craighead and P.L. McEuen
Science, 2007, 315(5811), 490-493.
22. *NEMS applications of graphene*
C. Changyao, S. Rosenblatt, K.I. Bolotin, P. Kim, I. Kymissis, H.L. Stormer, T.F. Heinz and J. Hone
in Electron Devices Meeting (IEDM), 2009 IEEE International, 2009.
23. *Coherent mixing of mechanical excitations in nano-optomechanical structures*
Q. Lin, J. Rosenberg, D. Chang, R. Camacho, M. Eichenfield, K.J. Vahala and O. Painter

Nat Photon, 2010, 4(4), 236-242.

Chapter 4

Feedback Oscillators

After having laid out the methods for understanding the frequency control element of our oscillators, namely, the piezoelectric/piezoresistive (PZE/PZR) Duffing resonator, we proceed to understand their dynamics when inserted into feedback loops. We begin by modeling the feedback loop within the amplitude equation, after which, we validate this modeling through measurements on the amplitude and frequency of the feedback oscillator as loop phase shift is swept. We also measure the phase noise in the feedback oscillator with the amplifier well saturated and provide arguments based on the isochrone formalism as to how parametric noise couples into the oscillator phase. Excellent qualitative agreement between the theory and experiment is shown, proving that the system dynamic range outlined in chapter 3 does not set strict limits on phase noise. *The theory for the parametric noise (with numerical simulations) was primarily developed by Eyal Kenig. The data for the phase noise was taken in collaboration with Guillermo Villanueva.*

4.1 Introduction

Electromechanical feedback oscillators have been miniaturized from quartz crystal oscillators [1], to MEMS oscillators [2], and finally, to NEMS oscillators [3]. Phase noise for these mechanical oscillators is projected from the loaded quality factor, the ratio of transmitted output power to input power through the resonator (S_{21}), and system dynamic range (DR) (as discussed in chapter 3). The purpose of the following chapter is to understand oscillator dynamics using devices taken beyond their dynamic range into the nonlinear regime, where the amplitude couples to the frequency. Such oscillators are defined as *nonisochronous oscillators* [4].

As the geometric tensile nonlinearity increases in flexural beams, the quality factor decreases. We can understand this as follows. Although sources of dissipation are not well understood in nanomechanical resonators, reference [5] notes that from thermodynamic arguments the upper bound of Q-f product for these resonators is estimated to be $\sim 10^{14}$ for bulk silicon or aluminum nitride. For fixed aspect ratio of a flexural doubly-clamped beam, as size decreases, frequency and nonlinearity increases. Thus, if all non-thermoelastic sources of dissipation are removed, then at a fixed aspect ratio, by increasing nonlinearity we necessarily decrease the quality factor.

The transmitted power through the device is another key characteristic which contributes to phase noise. Transmitted power through the resonator (S_{21}) is understood to decrease as size decreases [5] from theoretical arguments [6]. High values of amplification within the feedback loop are needed to satisfy the Barkhausen criterion for self-sustained oscillations, causing amplifier noise to be significantly amplified before being fed back to the resonator. In the case of a saturated feedback, this noise affects only the phase component of the actuation signal (at least

for amplifier noise being transduced into the resonator through the piezoelectric port). The amplifier noise converted into phase noise through this mechanism was shown to be reduced for a special set of system parameters at a ‘critical’ amplitude [7]. At that special point in parameter space, there is no dependence of the oscillator frequency on the loop phase shift. In this work, we extend this research into amplitudes beyond the critical amplitude.

In order to understand experiments related to oscillator phase noise above critical amplitudes, in the next section we next model the feedback loop within the amplitude equation. These results are also important for the modeling of coupled feedback oscillators in chapter 5.

4.2 Oscillators with Nonlinear Stiffness

We insert the feedback loop modeling directly into the amplitude equation that we derived in Appendix I. This gives

$$\frac{d\tilde{A}}{dT} + \frac{\tilde{A}}{2} - i\lambda_{ii}Q|\tilde{A}|^2\tilde{A} = -i\frac{\tilde{F}(\tilde{a})}{2}e^{i\Delta} \cdot e^{i\varphi(T)}, \quad (4.1)$$

where we take $\tilde{A} = \tilde{a}e^{i\varphi}$. Recall that \tilde{A} is the amplitude which varies at timescales on the order of the decay time. Here $\varphi(T)$ is the phase of the slow time oscillation such that $\frac{d\varphi}{dT} = \varphi' = \Omega$, which is the difference of the oscillator frequency and natural frequency of the resonator (with zero nonlinear stiffness). It is written as a function of the slow time T in order to emphasize its dependence on time, as opposed to Δ , which is a time-independent phase shift in the feedback loop. We consider only the first term in the nonlinear stiffness for resonator mode i (λ_{ii} from chapter 3), and drop any nonlinear dissipation. The nonlinear dissipation can only be seen at extremely high amplitudes, which none of these experiments are able to access. Therefore, all the

nonlinearity in the real (dissipative) part is due to amplifier feedback compression, which is inserted into the feedback function $\tilde{F}(\tilde{a})$.

We will scale equation (4.1) in order to obtain the unitless slow time amplitude such that $A = \sqrt{\lambda_{ii}Q}\tilde{A}$. Then equation (4.1) becomes

$$\frac{dA}{dT} + \frac{A}{2} - i|A|^2A = -i\frac{F(a)}{2}e^{i\Delta} \cdot e^{i\varphi(T)}, \quad (4.2)$$

where we have divided by a factor of $\sqrt{\lambda_{ii}Q}$. Also note that the feedback function has been normalized by the same factor.

To solve equation (4.2), we note that $A' = a'e^{i\varphi} + ia e^{i\varphi} \cdot \varphi'$. For steady state oscillations on a nearly circular limit cycle, slow time amplitude does not change in time, i.e., $a' = 0$. Splitting this between the real and imaginary parts we are left with two algebraic equations, given by

$$\varphi' = \Omega = -\frac{F(a)}{2a} \cos \Delta + |a|^2, \quad (4.3)$$

and

$$0 = a' = -\frac{a}{2} + \frac{F(a)}{2} \sin \Delta \Rightarrow a = F(a) \sin \Delta. \quad (4.4)$$

We can reduce equations (4.3) and (4.4) to give

$$\Omega = -\frac{\cot \Delta}{2} + |a|^2, \quad (4.5)$$

and

$$\frac{F(a)}{a} = \csc \Delta. \quad (4.6)$$

We can first acquire the amplitude by solving equation (4.4) and use this amplitude to find the frequency shift Ω .

At this point, it is impossible to proceed further without explicitly identifying the feedback function $F(a)$. Here we use a specific model for which equations (4.5) and (4.6) can be explicitly solved, which is generally not possible.

4.3 Feedback Oscillators with the Rapp Saturation Model

We consider a common model for solid state amplifiers with saturation, the Rapp model [8]. This model is

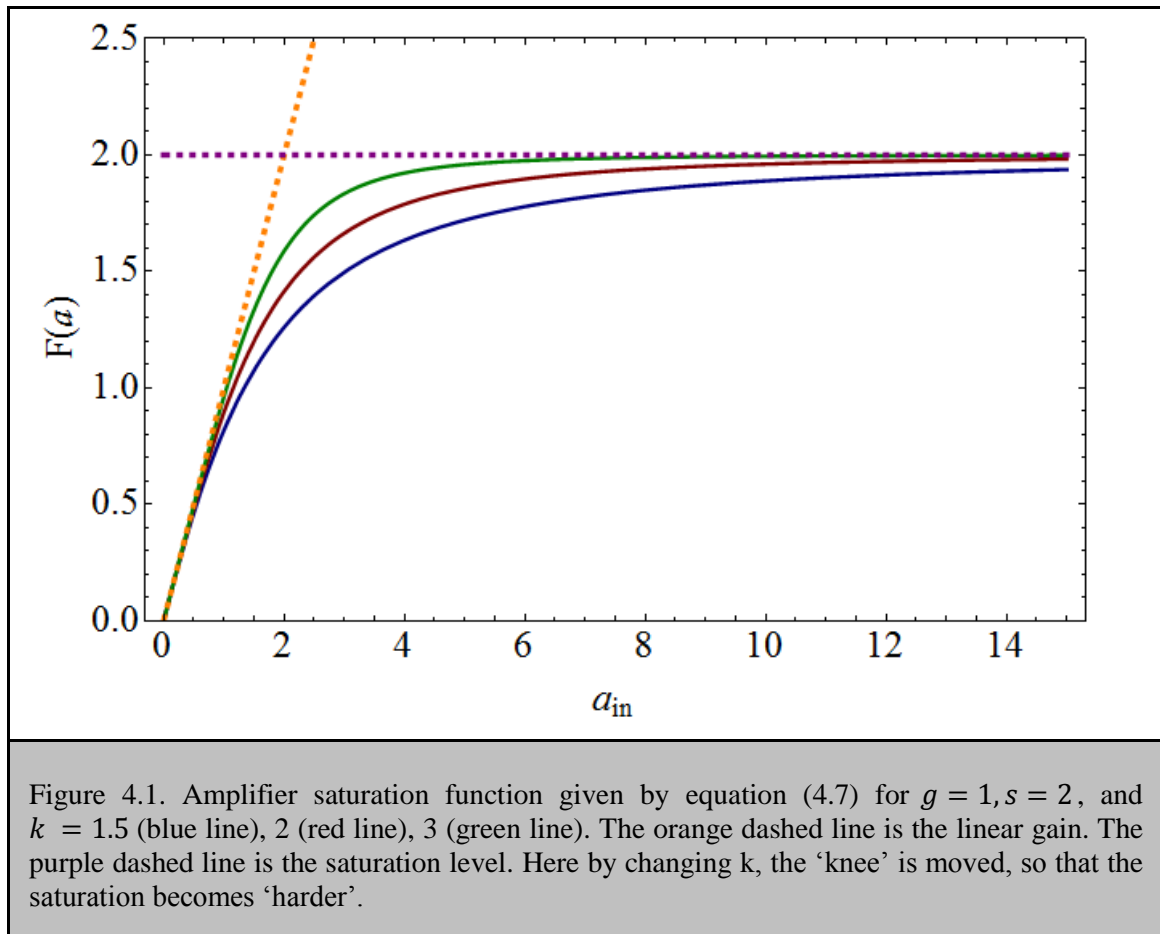
$$F(a) = \frac{ga}{\left[1 + \left(\frac{g}{s}a\right)^k\right]^{\frac{1}{k}}} \quad (4.7)$$

where k is a rational number (known as the ‘knee’), g is the unitless gain, and s is the saturation of this amplifier.

This feedback function behaves like a linear amplifier with gain g for low amplitudes. From equation (4.4) we can see that a non-zero steady state amplitude first becomes possible for increasing gain at $\Delta = \pi/2$, $g - 1 = 0$. This is the Barkhausen criterion for oscillation. This ‘gain’ g is therefore the total gain of the loop including signal losses associated with signal

transduction, but excluding the loss associated with device damping. It is *not* the gain of the amplifiers, which has to be very large ($10^3 - 10^4$) in order to counteract the signal loss associated with the NEMS device.

Equation (4.7) is plotted in Figure 4.1 for three different values of k , with $g = 1, s = 2$. As k increases, the knee moves up closer to the crossing of the unsaturated gain (orange dashed line) and the saturation (purple dashed line).



If we solve equation (4.4) using equation (4.7) we get

$$a = \frac{g}{s} [(g \sin \Delta)^k - 1]^{\frac{1}{k}}. \quad (4.8)$$

4.4 Experimental Validation of Feedback Loop Modeling

We validate the feedback loop modeling that we have proposed in equations (4.5) and (4.6) with a PZE/PZR NEMS device using the Rapp formula in equation (4.7). In Figure 4.2, we show the circuit diagram for the feedback oscillator experiment with a PZE/PZR NEMS device. The device is actuated through an impedance bridge (as in chapters 2 and 3). The signal out of the NEMS is fed through a low pass filter to remove stray harmonics above the device's fundamental frequency. The signal phase shift can be adjusted with the voltage controlled phase shifter (VC-PS, blue box). Then the signal is fed through an electronic limiter (Mini-circuits part #VLM-52) that has a limiting component made from a semiconducting diode. After the signal passes through this element, it can be attenuated using the voltage controlled attenuator (VCA, red box).

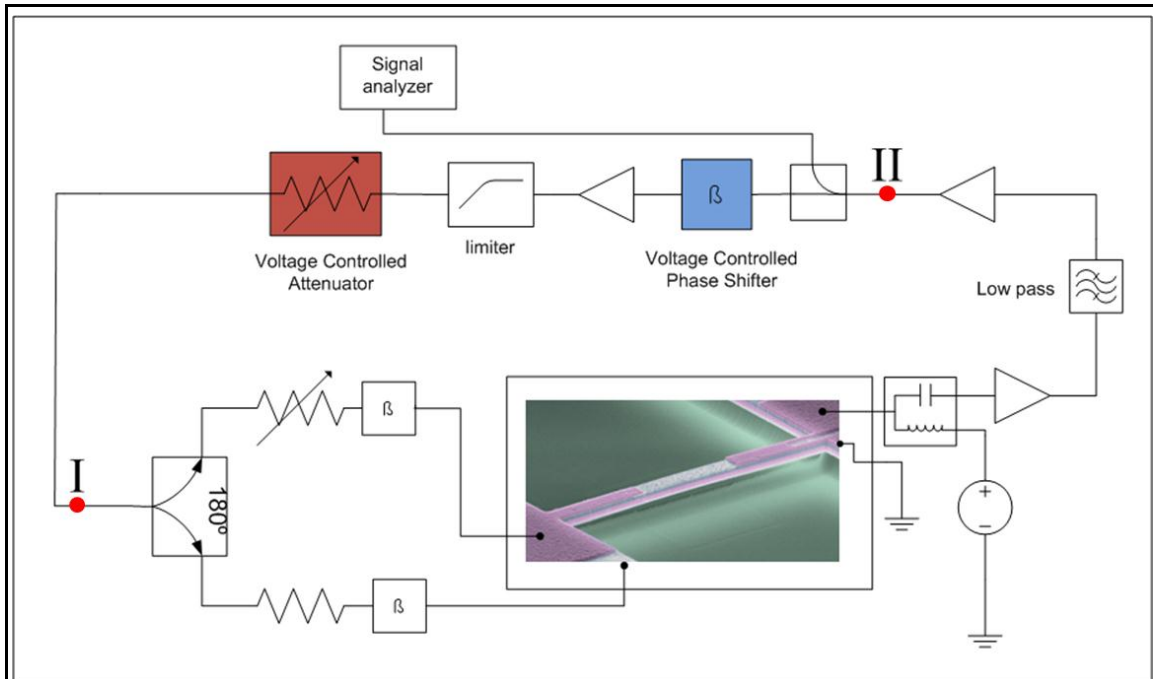
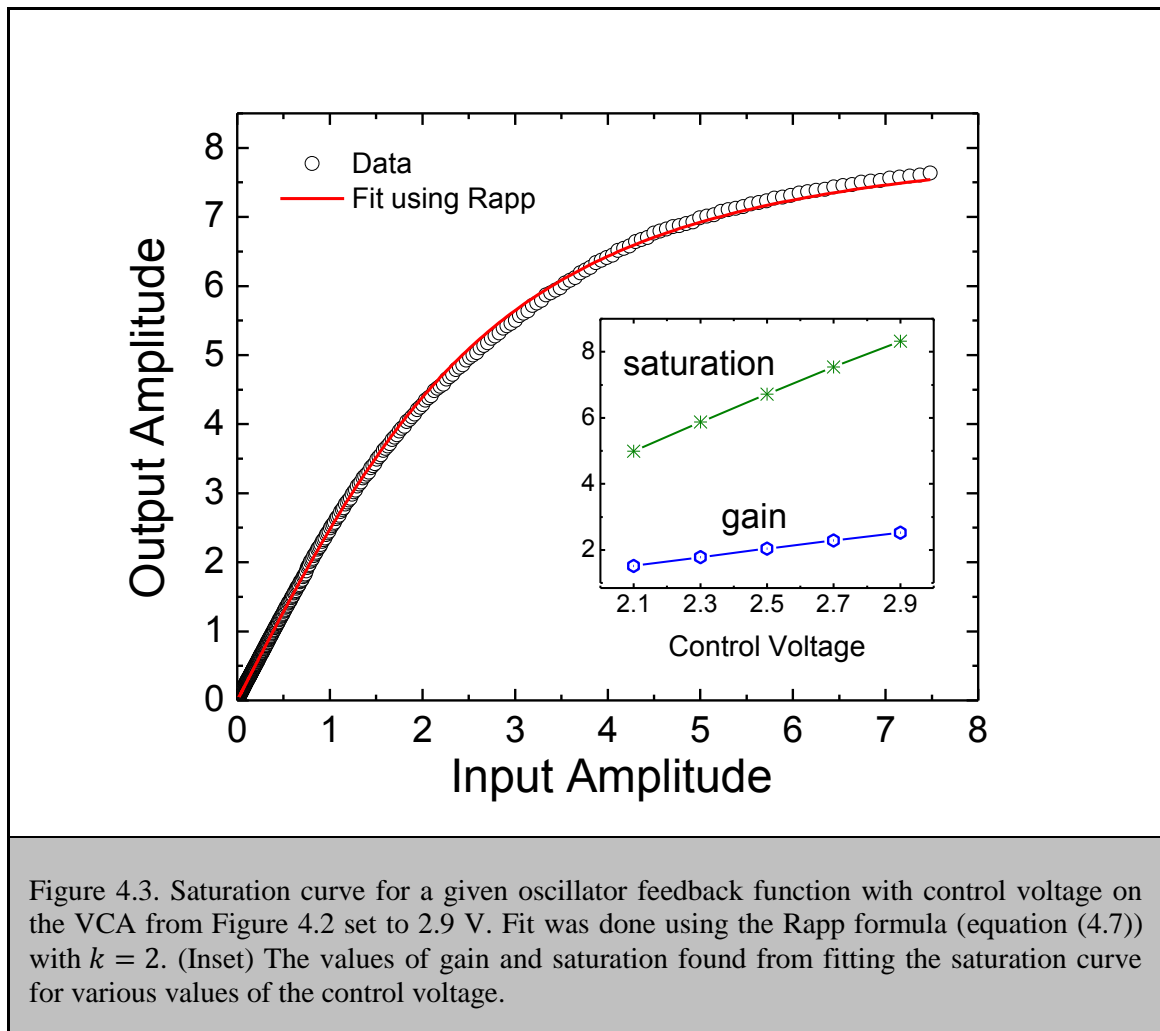


Figure 4.2. Feedback oscillator diagram using piezoelectric/piezoresistive device. The phase shift Δ is swept using a voltage controlled phase shifter. Saturation and gain is controlled through a voltage controlled attenuator, which is used after an electronic limiter. The saturation curve is found by sweeping the drive amplitude and measuring the total transfer function from point II to point I. Total gain is found by breaking the loop at either point I or point II and measuring the open loop resonance at low amplitudes around the loop back to the same point.

We can make predictions based on equations (4.5) and (4.8) by using values of gain and saturation found by examining the oscillator loop. First, we measure the gain by doing an open loop frequency sweep (by breaking the loop at point I and measuring the response back around to I) of the oscillator at low values of drive (taking the value at the resonance peak), so as not to saturate the electronic components. Again, this gain is not only the amplifier gain, but includes losses associated with signal transduction and the electronic components of the loop. Next, by measuring the transfer function of the electronic components (in amplitude) between points II and I, we find the saturation curve. We then scale this saturation curve so that the linear region of the

curve gives the values for gain we obtain from the open loop frequency sweep. We can then fit the saturation curve to equation (4.7) using $k = 2$ in order to find the values of g and s . In Figure 4.3 we show one such fit. The saturation and gain are plotted in the inset using this fit for several values of the attenuator control voltage in Figure 4.2 (“VCA”, red box). The amplitudes plotted in Figure 4.3 are unitless according to equation (4.4).

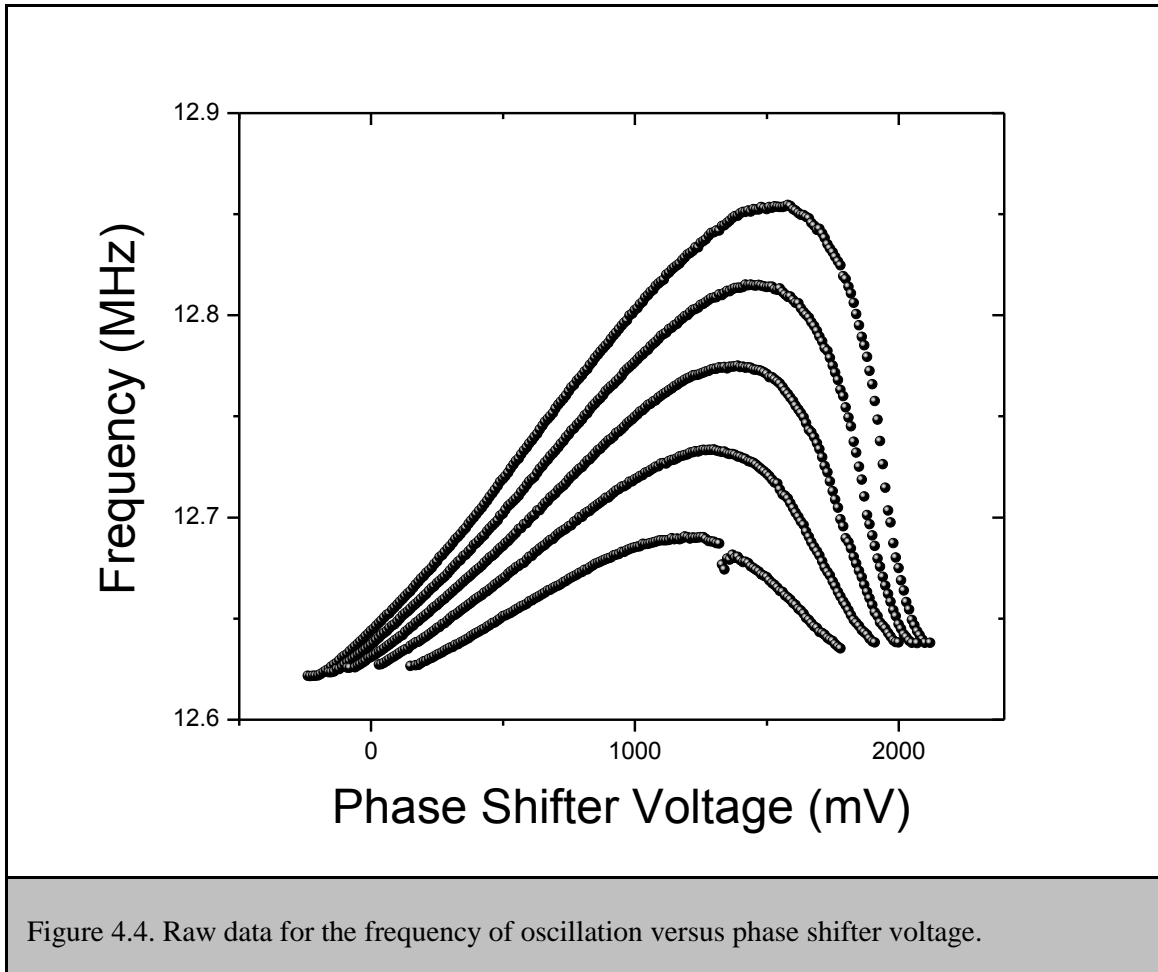


Next, we compare simulations of the oscillator amplitude and frequency using the values of gain and saturation found in Figure 4.3 to experimental data. In Table 4.1, we show the NEMS device properties relevant to these experiments on feedback oscillators. We measure the nonlinear

stiffness λ_{11} as laid out in chapter 3, with piezoresistive bias voltage set to 128mV. The oscillator's electronic signal at point II is measured as in Figure 4.2. The mechanical amplitudes are calibrated, at this same point, by measuring thermomechanical noise.

Device dimensions	Resonant frequency, f_i	Quality Factor	Nonlinear stiffness, λ_{11}
10 μ m x 400nm x 210nm	12.6 MHz	1590	1.55 x 10 ¹³ m ⁻²
Table 4.1. Relevant NEMS device properties for the feedback oscillator experiments.			

In Figure 4.4 we show the data for the frequencies of the oscillator measured as a function of the phase shifter voltage. This raw data coming in to the signal analyzer must be corrected since there is substantial frequency dependent phase shift associated finite signal path lengths and filtering.



In Figure 4.5, we show the results of this measurement against the prediction from using the values of gain and saturation found in Figure 4.3. We calibrate the loop phase against the phase shifter voltage and convert the plots in Figure 4.4 to Figure 4.5. The data agrees well with the prediction in amplitude and frequency. Slight differences between the data and predictions are probably due to the variation of attenuation within the phase shift for different values of phase shifter control voltage. With the agreement shown in Figure 4.5, we are confident in the ability of the feedback modeling to accurately describe the dynamics in feedback oscillators.

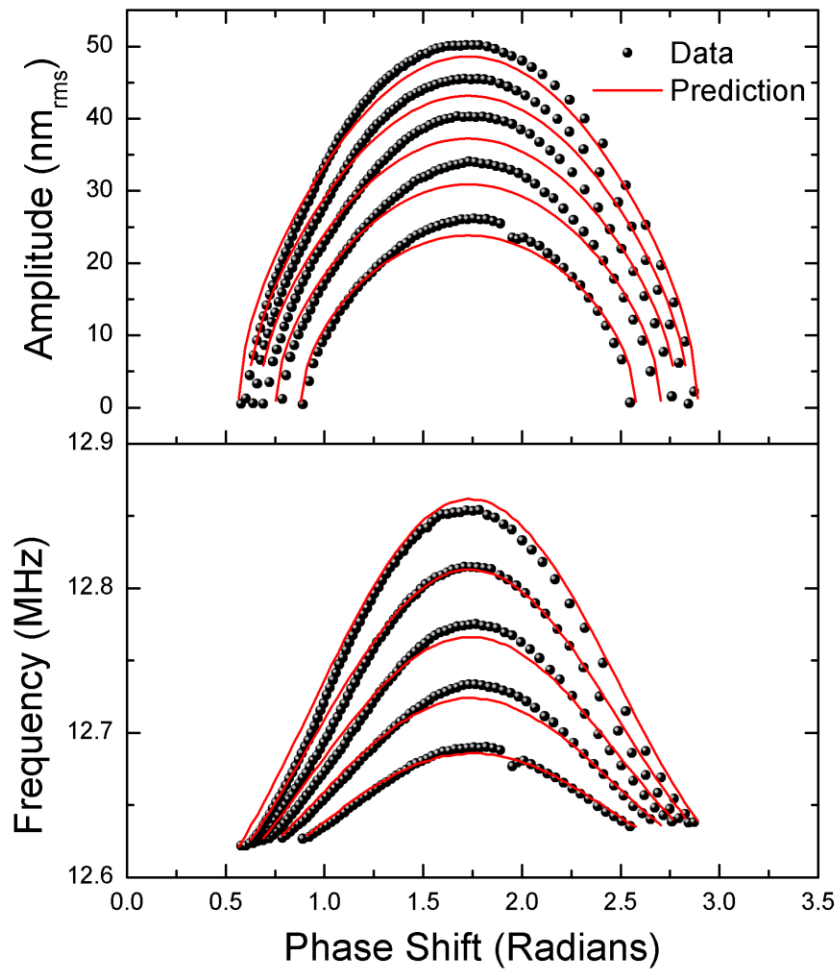


Figure 4.5. Measured amplitude and frequency (black spheres) against the predicted results using gain and saturation from the fits of the inset in Figure 4.3 (red lines). The ‘real’ phase shift plotted here is found by measuring the phase shift against frequency for a given values of phase shifter voltage.

4.5 Unsaturated and Saturated Oscillators

The previous discussion showed that changing the variable attenuator's control voltage (red box Figure 4.2) changes gain and saturation values, which alter steady state oscillator amplitude. However, from Figure 4.3 we can see that for large input amplitudes, output amplitudes would be immune to variations in the input. This is a limiting case for the feedback oscillator described above, which we will call the 'heavily saturated' or 'saturated' oscillator. If the oscillator is not saturated, we say it is 'unsaturated'.

For the case of the saturated oscillator we can write the feedback function in equation (4.7) as

$$F(a) = s \frac{\frac{g}{s} a}{\left[1 + \left(\frac{g}{s} a\right)^k\right]^{\frac{1}{k}}}, \quad (4.9)$$

to give in the limit of $ga \gg s$,

$$F(a) = s \frac{\frac{g}{s} a}{\left[1 + \left(\frac{g}{s} a\right)^k\right]^{\frac{1}{k}}} \xrightarrow{\frac{ga}{s} \gg 1} s, \quad (4.10)$$

so that the feedback function does not depend on the amplitude. Doing this will simplify the analysis of noise in feedback oscillators.

4.6 Noise in Saturated Oscillators

Since oscillator research has important implications in the timing and sensing communities, it is important to understand the lower limit of phase noise for nanomechanical resonator and oscillator systems. In equation (1.6), the ratio of thermal noise to oscillator carrier power gives the oscillator phase noise. One strategy for reducing phase noise would be to increase carrier power. The upper limit to this increase is conventionally understood to be the critical amplitude [9-12] (the point in driven nonlinear resonator systems where two stable solutions of amplitude exist for fixed frequency), since amplitude fluctuations couple into frequency fluctuations through the Duffing nonlinearity. Coupling of these fluctuations is known as amplitude-modulation to phase-modulation (AM-PM) conversion.

Reference [6] gives the limit on phase noise for a nanomechanical flexural beam

$$\mathcal{L}_\phi(\Delta f) \cong 10 \log \frac{3\sqrt{3}k_b T f_c}{2\pi M_{eff} t^2} \frac{1}{(\Delta f)^2}, \quad (4.11)$$

where $\Delta\omega$ is the offset from carrier frequency ω_c , M_{eff} is the effective mass, and t is the thickness in the dimension of vibration. Equation (4.11) is related to equation (1.6) by inserting the thermomechanical noise for the sideband power, and the power at critical amplitude for the carrier power. In other words, we have inserted the dynamic range for a NEMS device. This limit assumes two things: first, there is always AM-PM conversion above this limit, and second, thermomechanical noise is the only source of noise. However, in the case of most NEMS, these assumptions are false.

The first assumption is false in feedback oscillators, as will be shown later. This is due to the fact that there exists special feedback loop phase shift points where the system becomes isochronous within a small region of oscillator amplitudes. This will mean that if the system is thermomechanically limited, the system can be taken to larger amplitudes without any AM-PM conversion.

The second assumption is false since transducer/amplifier noise is dominant over thermomechanical noise in most flexural mechanical oscillators above a frequency of ~ 10 MHz (although recent developments within the optomechanics community [13, 14] have shown impressive results in thermomechanically-limited NEMS detection with excellent signal-to-background ratios). This means that when fed back to the resonator, the signal is noisier than if it were just thermomechanically noise limited. This assumption also does not account for other sources of noise such as temperature fluctuations [12] or surface adsorbates [15] which can cause fluctuations in resonator frequency.

This amplifier noise-induced phase noise was shown to be reduced in the work by Greywall, et. al. [7] by saturating the feedback, stabilizing the oscillator at the critical amplitude, and shifting the loop phase to $\Delta = 2\pi/3$. For these special conditions, the derivative of oscillator frequency with respect to loop phase shift becomes zero ($\frac{d\Omega}{d\Delta} = 0$) so that there was no dependence of the frequency to fluctuations in the loop phase shift. We will show how this occurs in saturated oscillators and extend these ideas to include nonisochronicity.

For a saturated oscillator we can write equation (4.2) with the feedback given by equation (4.10)

$$\frac{dA}{dT} = \left(-\frac{1}{2} + i|A|^2 \right) A - i\frac{S}{2} e^{i(A+\varphi)}, \quad (4.12)$$

This amplitude equation is complex and yields two real equations

$$\frac{da}{dT} = -\frac{a}{2} + \frac{s}{2} \sin \Delta = f_a, \quad (4.13)$$

and

$$\frac{d\varphi}{dT} = a^2 - \frac{s}{2a} \cos \Delta = f_\varphi. \quad (4.14)$$

Just as before the limit cycle oscillations are given by $f_a = 0$, so that

$$a_0 = s \sin \Delta, \quad (4.15)$$

and

$$\Omega = f_\varphi(a_0) = a_0^2 - \frac{s}{2a_0} \cos \Delta = s^2 \sin^2 \Delta - \frac{\cot \Delta}{2}. \quad (4.16)$$

With equations (4.15) and (4.16) we can examine how different noise sources will influence phase noise. We write equations (4.13) and (4.14) and include thermomechanical fluctuations and phase shift fluctuations (to first order). This gives

$$\frac{da}{dT} = -\frac{a}{2} + \frac{s}{2} \sin \Delta + \text{Re}(\xi_{th}) + \xi_{\Delta} \frac{s}{2} \cos \Delta, \quad (4.17)$$

and

$$\frac{d\varphi}{dT} = a^2 + \frac{s}{2a} \cos \Delta - \frac{\text{Im}(\xi_{th})}{a} - \xi_{\Delta} \frac{s}{2a} \sin \Delta. \quad (4.18)$$

If we consider each noise source ($n \in \{Th, \Delta\}$) to be white and have noise intensity I_n we can define

$$\langle \xi_n(T) \xi_n(T') \rangle = I_n \delta(T - T') \quad (4.19)$$

Although we use a white noise source here, we can include colored noise sources without affecting the qualitative nature of the discussion. Equation (4.19) will change along with the spectral shape if colored noise sources are used.

Going into the rotating frame, the oscillator phase is defined

$$\psi = \varphi - \Omega T \quad (4.20)$$

For large time delays white noise leads to diffusion[16] so that

$$\langle [\psi(T + \tau) - \psi(T)]^2 \rangle = (I_{Th,re} D_{Th,re} + I_{Th,im} D_{Th,im} + I_{\Delta} D_{\Delta}) |\tau| \quad (4.21)$$

where the constants D_n are the susceptibilities of the oscillator phase. The noise susceptibility, together with the noise intensity, will give the amount of phase noise diffusion of the oscillator phase.

From references [16, 17], for white noise sources the spectral density of the oscillator displacement is Lorentzian with a spectral width given by the product of the phase diffusion and the resonator half-width, so that

$$S_{aa}(f) \propto \frac{1}{\left(\frac{\sum_n I_n D_n f_0}{2Q}\right)^2 + (f - f_0)^2}. \quad (4.22)$$

We can remove the diffusion dependence in the denominator for $|f - f_0| \gg |I_n D_n| f_0 / 2Q$. The

diffusion term here is usually much smaller than 1, so for $|f - f_0| > f_0 / 2Q$ we get

$$S_{aa}(f) \propto \frac{1}{(f - f_0)^2}. \quad (4.23)$$

Thus the noise intensity outside the spectral half-width of the resonator is goes as $1/f^2$.

The phase noise is conventionally defined by the logarithm of the ratio of the sideband spectral density to the total power [18],

$$\mathcal{L}_\phi(\Delta f) = 10 \log_{10} \left[\frac{S_{aa}(f + \Delta f)}{P_{tot}} \right], \quad (4.24)$$

which, using equation (4.22) gives

$$\mathcal{L}_\phi(\Delta f) = 10 \log_{10} \left[\frac{1}{2\pi Q} \frac{\sum_n I_n D_n f_0}{\left(\frac{\sum_n I_n D_n f_0}{2Q}\right)^2 + (\Delta f)^2} \right], \quad (4.25)$$

and using equation (4.23) gives

$$\mathcal{L}_\phi(\Delta f) \approx 10 \log_{10} \left[\frac{1}{2\pi Q} \frac{\sum_n I_n D_n f_0}{(\Delta f)^2} \right]. \quad (4.26)$$

Thus we have a simple expression for the phase noise in equation (4.26). The phase diffusion terms in the numerator set the phase noise, and for frequencies outside the width, we have $1/\Delta f^2$ dependence as expected [18]. The only thing left to do is calculate the phase diffusion terms due to the susceptibility to the thermal and loop phase fluctuations.

As mentioned in Chapter 1, the susceptibility of the oscillator phase in equations (4.20) to noise is intricately related to two topological sets: the limit cycle, and the isochrones. Since the limit cycle is approximately circular for weak nonlinearity, we only have to examine the isochrones.

4.7 Isochrones and Noise Diffusion Constants

We find the isochrones for the heavily saturated oscillator by the method described by Reference [19]. Since the limit cycle is rotationally symmetric, the isochrones are also rotationally symmetric

$$\mathbb{I}(\varphi, a) = \varphi - f(a), \quad (4.27)$$

where f is a function to be determined. We can take the derivative of equation (4.27) to get

$$\frac{df}{da} = - \frac{\frac{d\mathbb{I}}{dt} - \frac{d\varphi}{dt}}{\frac{da}{dt}}. \quad (4.28)$$

We also know that the isochrones rotate at the rotational velocity of the limit cycle, i.e.

$$\frac{d\mathbb{I}}{dt} = \Omega = s^2 \sin^2 \Delta - \frac{1}{2} \cot \Delta, \quad (4.29)$$

and so after putting equations (4.13), (4.14), and (4.29) into (4.28) and integrating we get

$$\mathbb{I}(\varphi, a) = \varphi + 2 a s \sin \Delta + a^2 + \cot \Delta \ln a. \quad (4.30)$$

We plot an isochrones set for $\Delta = \pi/2$, and $s = 1$ in Figure 4.6. The red line is the limit cycle, the blue dashed lines are the isochrones, and the green lines are flow of the oscillator under two different perturbations along the limit cycle.

We diagram the oscillator dynamics in Figure 4.6 (inset) to understand how noise forces in phase space influence the oscillator's phase noise. The eigenvectors ($\mathbf{j}_{\mathbb{I}}, \mathbf{j}_{\varphi}$) of the Jacobian matrix of equations (4.13) and (4.14) along with the eigenvector (\mathbf{j}_{φ^t}) of the transposed Jacobian are the black arrows. The transposed Jacobian eigenvector corresponding to the radial direction is not necessary for understanding the noise susceptibility, and has been left out. The eigenvector

pointing along the isochrones \mathbf{j}_{\parallel} has eigenvalue $-1/2$, meaning that perturbations along this direction will decay in time since negative eigenvalues correspond to stable solutions. This is the maximum rate of decay available according to equation (4.13). Along this direction, noise will have no long term effect on the oscillator. Therefore, it is perturbations perpendicular to this vector, in the direction of \mathbf{j}_{φ^t} , that create maximum phase deviation. For a more detailed explanation, see references [17, 19].

The eigenvectors of the Jacobian vectors are

$$\mathbf{j}_{\parallel} = \left\{ -\frac{2s^2 \sin^2 \Delta}{8s^3 \sin^3 \Delta + s \cos \Delta}, 1 \right\}, \mathbf{j}_{\varphi} = \{0, 1\}. \quad (4.31)$$

The noise vector, \mathbf{v}_n , whose components are the noise terms from equations (4.17) and (4.18), is represented by the red arrow, and is projected along \mathbf{j}_{φ^t} to find its contribution to the phase. The transposed Jacobian eigenvector is

$$\mathbf{j}_{\varphi^t} = \left\{ 2s \sin \Delta + \frac{s \cos \Delta}{4s^2 \sin^2 \Delta}, 1 \right\}. \quad (4.32)$$

Note that when the amplitude component of \mathbf{j}_{φ^t} is zero, the vector points along the oscillator phase and the oscillator is isochronous.

The susceptibility to noise from a noise vector is given by

$$D_n = |\mathbf{v}_n \cdot \mathbf{j}_{\varphi^t}|^2 = \mathbf{v}_1^2 \quad (4.33)$$

which was used in equation (4.21).

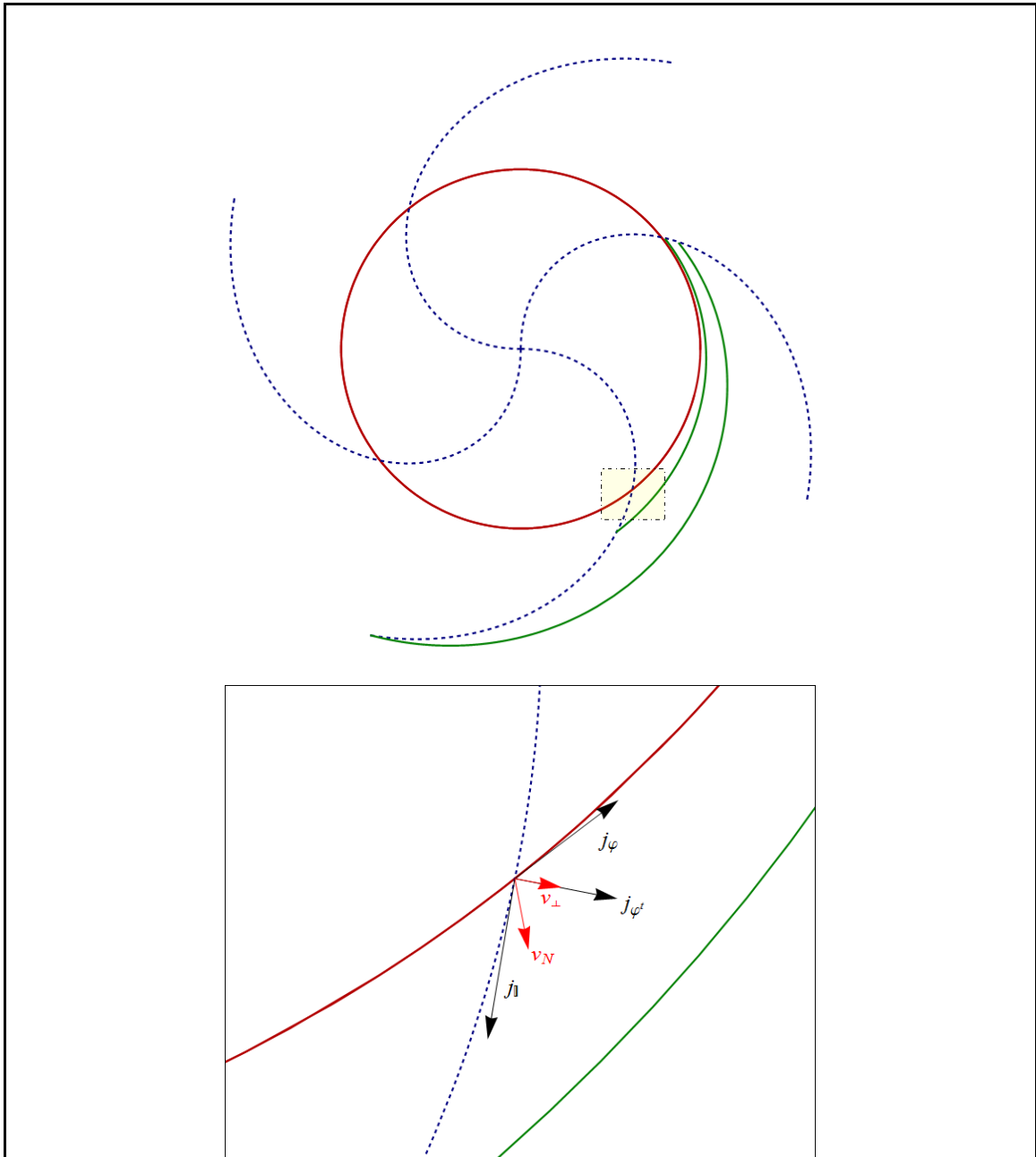


Figure 4.6. Phase space for the saturated oscillator for $\Delta = \frac{\pi}{2}, s = 1$. The red line represents the limit cycle. The blue dashed lines are isochrones for this oscillator. Green lines show the evolution of the oscillator with two different perturbations along the isochrones. (Inset) Zooming in, for a given noise vector \mathbf{v}_n , by projecting this vector along the maximal phase change direction \mathbf{j}_{φ^t} (found from the transposed Jacobian matrix of equations (4.13) and (4.14)), we can find the diffusion constant for that noise source.

4.8 Phase Noise Due to Fluctuating Phase Shift

We can directly calculate the phase noise susceptibility due to a fluctuating phase shift. According to equations (4.17) and (4.18) we have for the noise vector for the phase fluctuations,

$$\mathbf{v}_{\delta\Delta} = \left\{ \frac{s}{2} \cos \Delta, -\frac{1}{2} \right\}. \quad (4.34)$$

By using equation (4.33) with (4.34) and (4.32) we get

$$D_{\Delta} = \left(\frac{1}{2} s \cos \Delta \left(4s \sin \Delta + \frac{s \cos \Delta}{2s^2 \sin^2 \Delta} \right) - \frac{1}{2} s^2 \sin^2 \Delta \right)^2. \quad (4.35)$$

For equation (4.35) there exists a solution in saturation s and phase shift Δ for which the term inside the parentheses is zero thereby nulling the noise susceptibility from a fluctuating phase shift. We know this zero solution exists for $a \geq a_{crit}$ from Greywall et. al. [7] which is equivalent to finding where the derivative of the oscillator relative to the phase shift is zero,

$$\frac{d\Omega}{d\Delta} = 0.$$

4.9 Phase Noise Due to Thermomechanical Noise

We apply the same reasoning to the phase noise due to thermomechanical fluctuations. From equations (4.17) and (4.18) we get two noise vectors

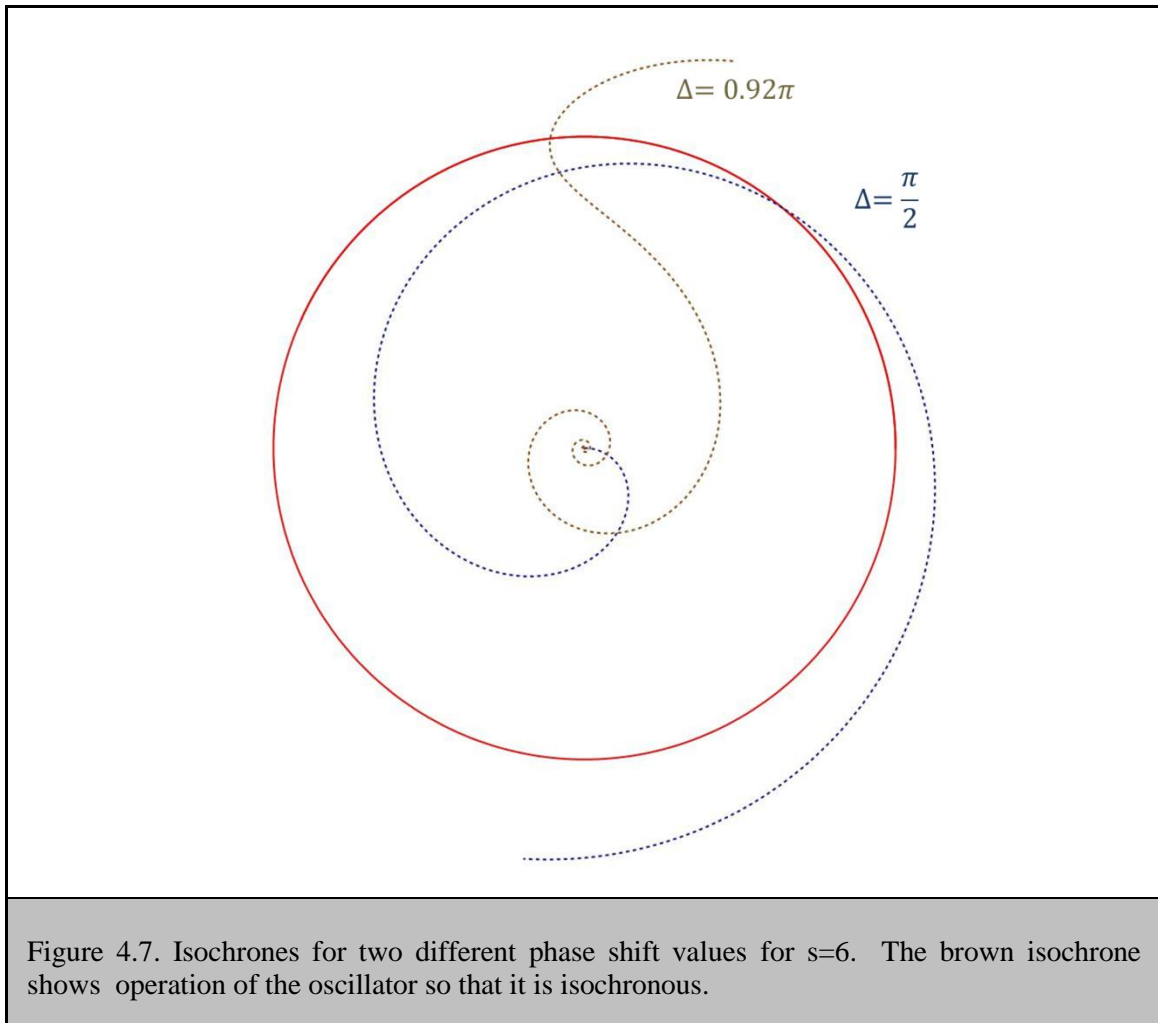
$$\mathbf{v}_{Th,Re} = \{1,0\}, \quad \mathbf{v}_{Th,Im} = \left\{0, \frac{1}{s \sin \Delta}\right\}, \quad (4.36)$$

which, together with equation (4.32) yields

$$D_{Th,Re} = \left(2s \sin \Delta + \frac{s \cos \Delta}{4s^2 \sin^2 \Delta}\right)^2, \quad D_{Th,Im} = \left(\frac{1}{s \sin \Delta}\right)^2. \quad (4.37)$$

Note that the real part of the thermal noise projects onto the amplitude term of the transposed Jacobian vector, and thus, for isochronous oscillators, $D_{Th,Re}$ is zero. In other words, finding a solution for saturation s and phase shift Δ which gives zero inside the parentheses gives no AM-PM conversion. There exists solutions of this type for $s > 0$ and $\frac{\pi}{2} \leq \Delta \leq \pi$. The result for the imaginary component $D_{Th,Im}$ is the standard result [12] which comes from increasing the SNR, where the signal here is given by $a = s \sin \Delta$.

In Figure 4.7 we show the isochrones for two different values of loop phase shift Δ and saturation $s = 6$. For a special value of loop phase shift $\Delta = 0.92$ the isochrones are perpendicular to the limit cycle. Hence, the oscillator is isochronous, eliminating the AM-PM conversion. This is not limited to amplitude fluctuations arising from thermomechanical fluctuations, but includes amplitude fluctuations due to other sources, such as fluctuations in damping rate[20].



4.10 Optimizing Phase Noise for Both Phase Shift and Thermomechanical Fluctuations

To bring the phase shift fluctuations into the picture, we plot both the oscillator frequency as a function of phase shift and the oscillator amplitude against frequency as a function of phase

shift. In Figure 4.8 (a), we show the oscillator frequency as a function of loop phase shift for different values of saturation (blue, green, brown, and red solid lines). The purple and orange lines are the points where the susceptibility in equation (4.35) is zero, which eliminates the conversion from loop phase shift fluctuations to oscillator phase fluctuations. Operating the oscillator at these points eliminates the conversion of amplifier noise on the phase noise of a saturated oscillator.

In (b), we plot amplitude against frequency while changing phase shift and saturation. The same points from (a) are plotted in purple and orange on this plot. In cyan, we show points where the oscillator is isochronous, as in Figure 4.7 (brown line) where the isochrones are perpendicular to the limit cycle. Note that in (b) the orange line is very close to the cyan line, which, we claim, corresponds to the minimums in the experimental data of Figure 4.10.

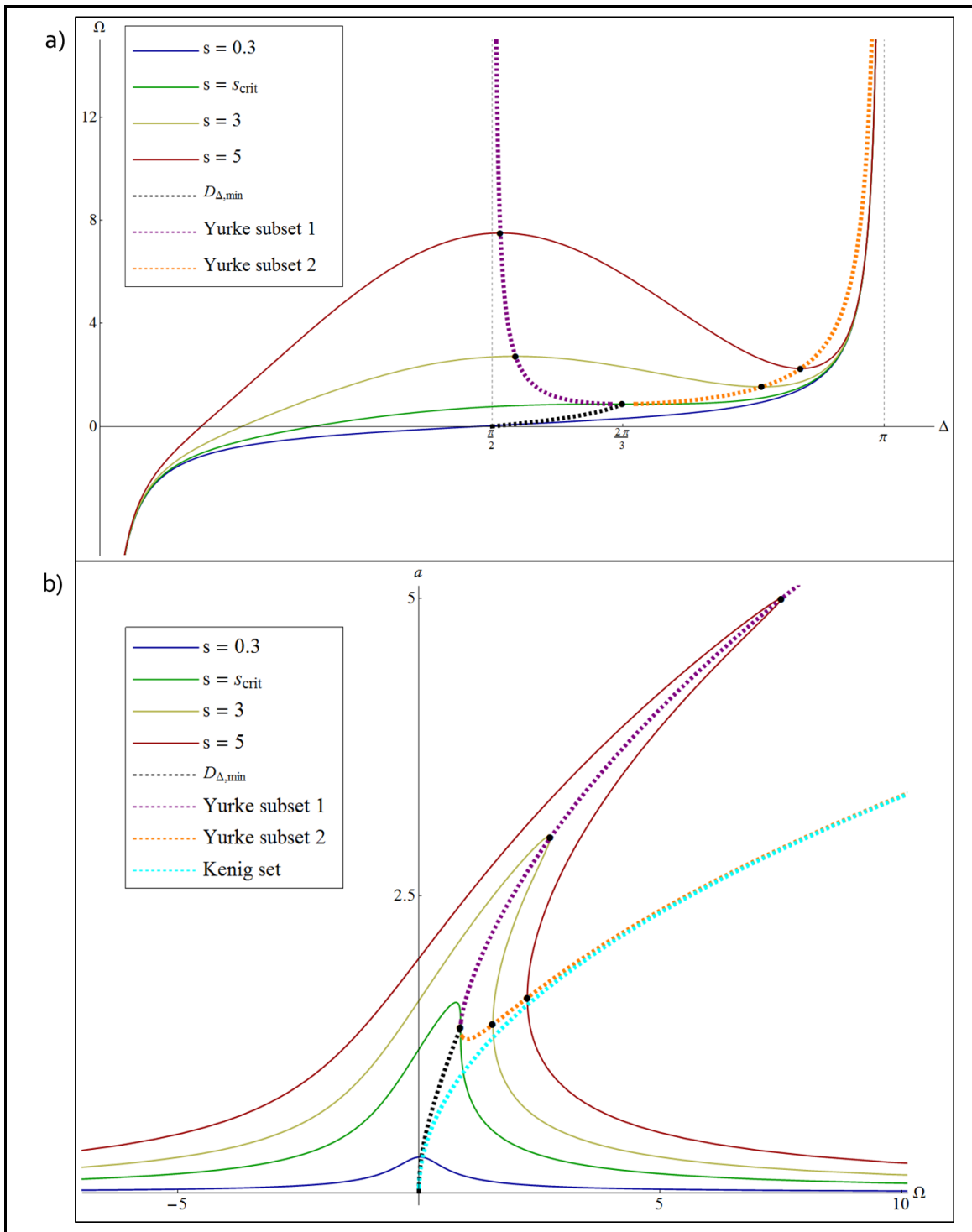
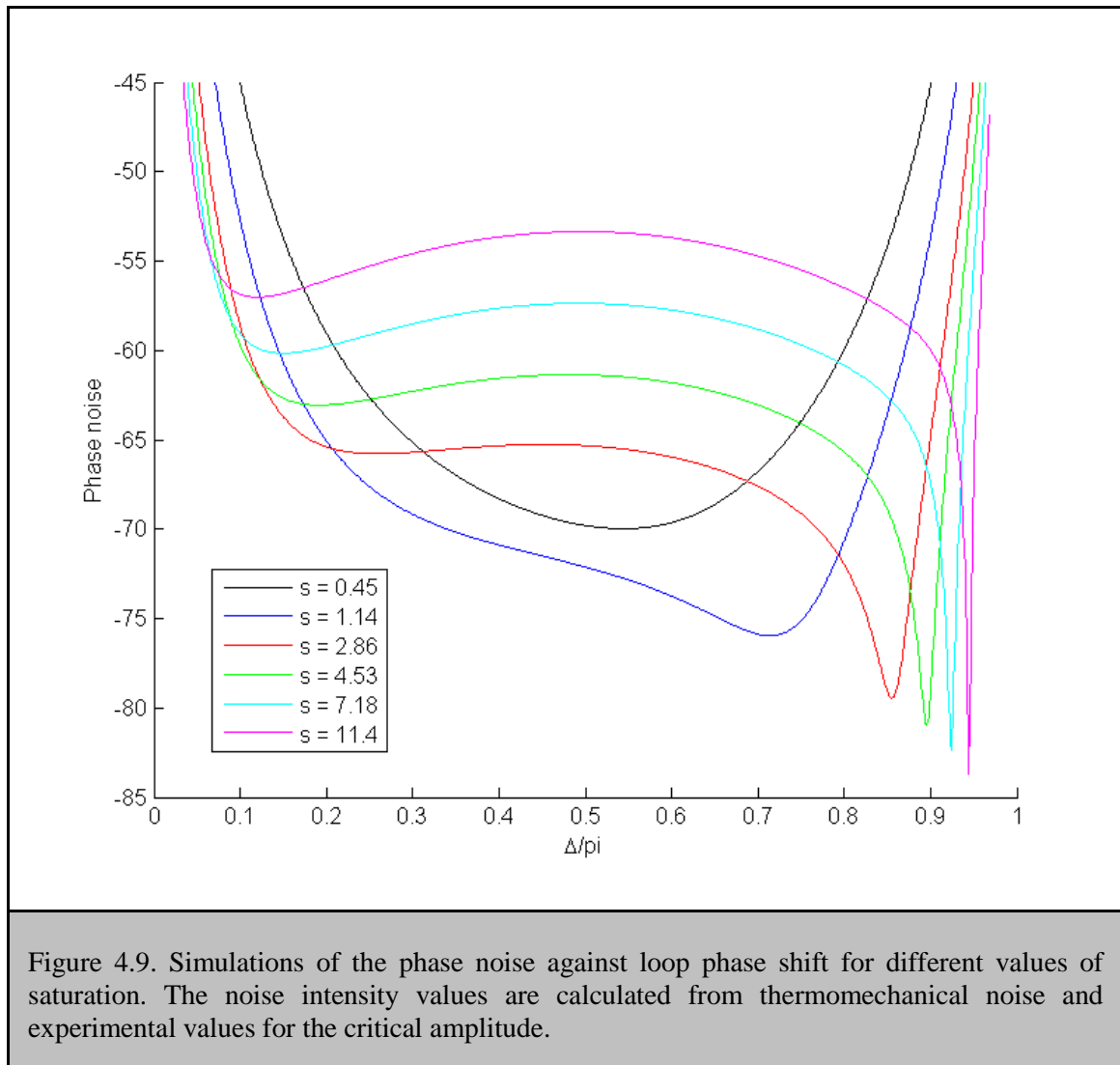


Figure 4.8. (a) Frequency plotted against loop phase shift for four different saturations. The points given by equation (4.35) are shown in purple and orange. The black line is the points with minimum phase shift slope. (b) The purple and orange lines correspond to the purple and orange lines in (a). The isochronous points are shown in cyan.

In Figure 4.9 we present Matlab calculations for the phase noise at 1kHz offset as a function of loop phase shift for different values of saturation, using equation (4.25) with noise intensities $I_{Th,Re} = I_{Th,Im} = \frac{k_B T}{E_c} = 1.2 * 10^{-5}$, and $I_{\Delta} = \frac{1}{a_0^2} I_{Th}$. This noise intensity is scaleless (coming from the amplitude equation) and so we must scale out the displacement from the thermal noise using the same factor of nonlinear stiffness. Therefore, the value for the thermomechanical noise intensity is the ratio of the thermal noise energy to the energy at critical amplitude. We assume equality (at unit amplitude) between phase shift noise intensity and thermal noise fluctuation intensity based on agreement between predicted values and data (to be presented in the next section). We also assume the origin of the phase shift fluctuations come from amplifier noise fed into the saturation element and so depends on the SNR of the oscillator (which increases as noise is amplifier noise is held constant and signal increases). The saturation values are chosen to be the same as the saturation values taken from the experimental data presented in the next section.

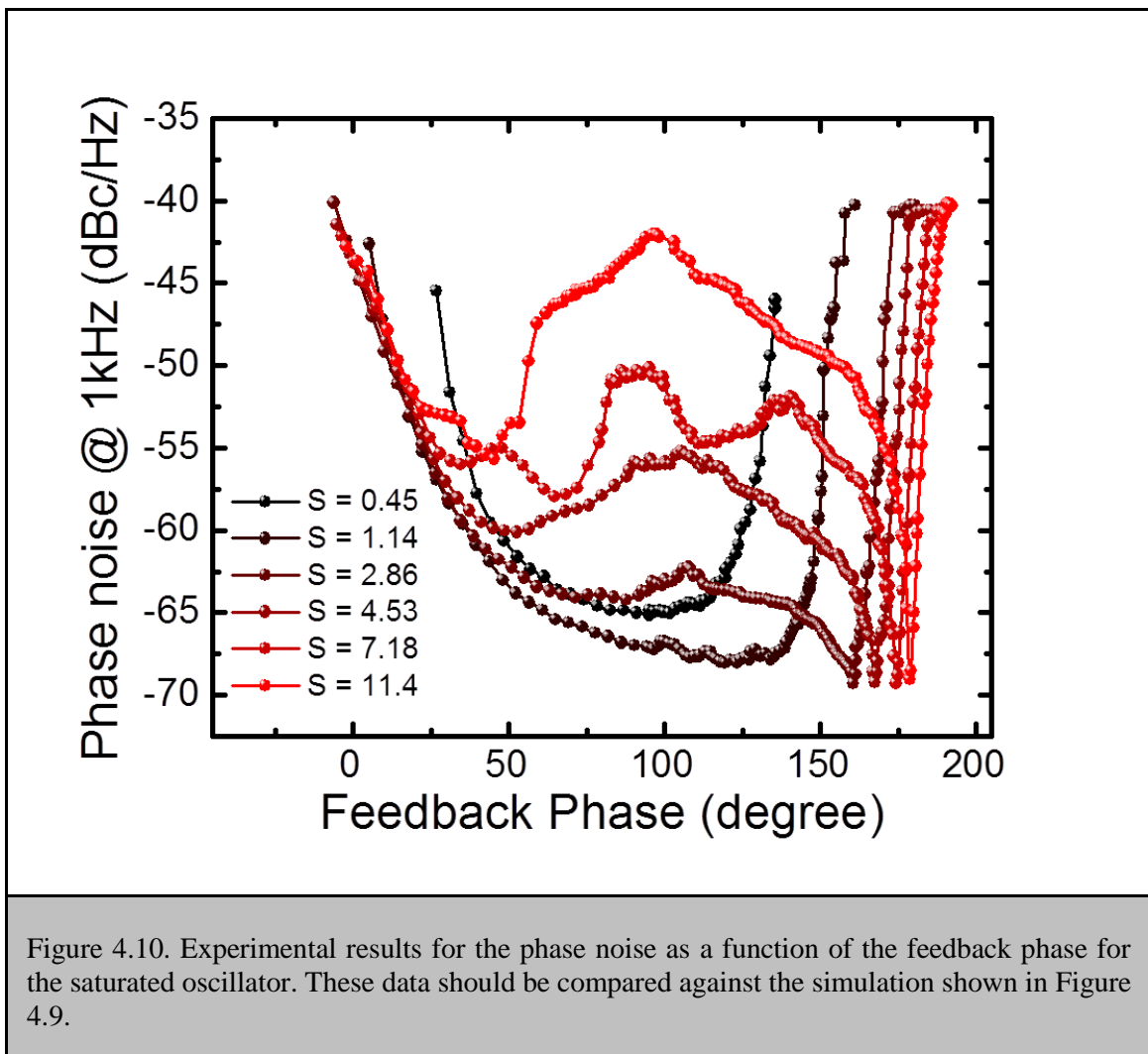


4.11 Experimental Results for Noise in a Saturated Oscillator

We measure the phase noise (at point II in Figure 4.2) and present this data in Figure 4.10. We show the phase noise for the oscillator at 1kHz offset as the phase shifter is adjusted, with the saturation stepped for different colors. Notice that the qualitative behavior of the curves is

strikingly similar to the simulations presented in Figure 4.9. However, the scale seems to be shifted by $\sim 10\text{dB}$ between the two plots. This probably signifies an additional source of noise.

It should be noted that the minimum noise in the experiment near the isochronous point for $s \geq 2.86$ is limited at -70dBc/Hz , whereas in theory it should keep decreasing with increasing saturation (Figure 4.9). The origin of this limit is unclear, but we note that it corresponds to the limit found from Allen deviation measurements in phased locked loops [21], implying that this is related to direct frequency fluctuations in the resonant device [22].



In summary, we have shown theoretically that there exists a special feedback phase shift Δ and saturation s which causes the oscillator to be isochronous, eliminating AM-PM conversion. These isochronous points are shown to exist above critical amplitudes. Therefore, in thermomechanically noise limited oscillators (where thermomechanical noise dominates amplifier noise), the oscillator amplitude is not limited to values below the critical amplitude. Since increasing oscillator power decreases oscillator phase noise for zero AM-PM conversion, phase noise also decreases. In addition, this point of isochronicity is predicted to exist near a point of minimum conversion of loop phase shift noise to phase noise. Most importantly, we have confirmed these theoretical predictions, at least qualitatively, with experimental data on a NEMS oscillator. These results show that *feedback oscillator phase noise is not limited to estimates based on the dynamic range (as described in equation (4.11))*. This should lead to a phase noise limit lower than predicted by the theory published for NEMS sensors [23, 24] if the direct device frequency noise is eliminated.

If there are more noise sources than just thermomechanical noise, such as loop phase shift noise, then one can use the nonisochronicity to reduce the influence of the noise sources on the phase noise by changing the loop phase shift, as was shown in equation (4.35) and in reference [7]. This gives more flexibility in design for oscillators than suggested by Leeson's formula, where the phase noise strongly depends on amplifier noise (and therefore insertion loss) and quality factor.

4.12 Future Work

These results can be extended to the more general case of the Rapp model. We expect regions in the parameter space of the oscillator (damping, saturation, nonlinear stiffness, phase

shift, and gain) which will give similar results. These results will include gain which complicates the analysis since amplitude fluctuations can be fed back to the oscillator, and thus be converted to phase noise through nonisochronicity.

Even though the phase noise data only qualitatively agree with calculations, they hint at strategies to reduce the noise further. For example, if direct frequency noise [22] or nonlinear stiffness fluctuations set the limit on phase noise, since the parametric fluctuations probably have a single source (such as temperature, charge, etc), they can be used to ‘beat’ against each other. This would be important since this would be a method for reducing fundamental device frequency noise (which is correlated) by employing feedback.

Since quality factor may play no role for an oscillator at a point of zero phase shift susceptibility (since Q will be eliminated for equation (4.26) with $I_{Th} \propto 1/E_c \propto Q$), we can explore non-mechanical types of oscillators that have not been implemented before, which were rejected due to high damping rates. These can include electronic oscillators which are easier to integrate and have a long history of application outside the scope of stable frequency sources [5, 25, 26].

Finally, this research opens up new ways of understanding nonisochronous oscillators of all types, and can be used to examine more exotic oscillators [27] to find proper bias point to reduce the noise.

Bibliography

1. ***A History of the Quartz Crystal Industry in the USA***
V.E. Bottom
in Thirty Fifth Annual Frequency Control Symposium. 1981, 1981.
2. ***A review of the recent development of MEMS and crystal oscillators and their impacts on the frequency control products industry***
C.S. Lam
in Ultrasonics Symposium, 2008. IUS 2008. IEEE, 2008.
3. ***A self-sustaining ultrahigh-frequency nanoelectromechanical oscillator***
X.L. Feng, C.J. White, A. Hajimiri and M.L. Roukes
Nature Nanotechnology, 2008, 3(6), 342-346.
4. A. Pikovsky, M. Rosenblum and J. Kurths, *Synchronization : a universal concept in nonlinear sciences.* The Cambridge nonlinear science series. 2001, Cambridge: Cambridge University Press. xix, 411 p.
5. ***A review of MEMS oscillators for frequency reference and timing applications***
J.T.M.v. Beek and R. Puers
Journal of Micromechanics and Microengineering, 2012, 22(1), 013001.
6. X.L. Feng, *Ultra-High Frequency Nanoelectromechanical Systems with Low-Noise Technologies for Single-Molecule Mass Sensing*, in *Electrical Engineering*. 2006, California Institute of Technology: Pasadena, California.
7. ***Evading amplifier noise in nonlinear oscillators***
D.S. Greywall, B. Yurke, P.A. Busch, A.N. Pargellis and R.L. Willett
Physical Review Letters, 1994, 72(19), 2992-2995.
8. ***Pattern selection in parametrically driven arrays of nonlinear resonators***
E. Kenig, R. Lifshitz and M.C. Cross
Physical Review E, 2009, 79(2), -.
9. ***Tuning nonlinearity, dynamic range, and frequency of nanomechanical resonators***
I. Kozinsky, H.W.C. Postma, I. Bargatin and M.L. Roukes
Applied Physics Letters, 2006, 88(25).
10. H.W.C. Postma, I. Kozinsky, A. Husain and M.L. Roukes, *Dynamic range of nanotube- and nanowire-based electromechanical systems.* Vol. 86. 2005: AIP. 223105.
11. ***Fundamental limits on the frequency stabilities of crystal oscillators***
F.L. Walls and J.R. Vig
Ultrasonics, Ferroelectrics and Frequency Control, IEEE Transactions on, 1995, 42(4), 576-589.

12. *Noise processes in nanomechanical resonators*
A.N. Cleland and M.L. Roukes
Journal of Applied Physics, 2002, 92(5), 2758-2769.
13. *Harnessing optical forces in integrated photonic circuits*
M. Li, W.H.P. Pernice, C. Xiong, T. Baehr-Jones, M. Hochberg and H.X. Tang
Nature, 2008, 456(7221), 480-484.
14. *Near-field cavity optomechanics with nanomechanical oscillators*
G. Anetsberger, O. Arcizet, Q.P. Unterreithmeier, R. Riviere, A. Schliesser, E.M. Weig, J.P. Kotthaus and T.J. Kippenberg
Nature Physics, 2009, 5(12), 909-914.
15. *Surface Adsorbate Fluctuations and Noise in Nanoelectromechanical Systems*
Y.T. Yang, C. Callegari, X.L. Feng and M.L. Roukes
Nano Letters, 2011, 11(4), 1753-1759.
16. *Classical Noise. V. Noise in Self-Sustained Oscillators*
M. Lax
Physical Review, 1967, 160(2), 290-307.
17. *Phase noise in oscillators: a unifying theory and numerical methods for characterization*
A. Demir, A. Mehrotra and J. Roychowdhury
Circuits and Systems I: Fundamental Theory and Applications, IEEE Transactions on, 2000, 47(5), 655-674.
18. *A simple model of feedback oscillator noise spectrum*
D.B. Leeson
Proceedings of the IEEE, 1966, 54(2), 329-330.
19. *Oscillator Phase Noise: A Geometrical Approach*
T. Djurhuus, V. Krozer, J. Vidkjaer and T.K. Johansen
Ieee Transactions on Circuits and Systems I-Regular Papers, 2009, 56(7), 1373-1382.
20. E. Kenig, *Minimizing phase noise in duffing oscillators above critical amplitude*. 2012.
21. *Towards single-molecule nanomechanical mass spectrometry*
A.K. Naik, M.S. Hanay, W.K. Hiebert, X.L. Feng and M.L. Roukes
Nature Nanotechnology, 2009, 4(7), 445-450.
22. *Detecting and characterizing frequency fluctuations of vibrational modes*
Z.A. Maizelis, M.L. Roukes and M.I. Dykman
Physical Review B, 2011, 84(14), 144301.
23. *Ultrasensitive nanoelectromechanical mass detection*
K.L. Ekinici, X.M.H. Huang and M.L. Roukes

24. **Applied Physics Letters**, 2004, 84(22), 4469-4471.
Ultra-sensitive NEMS-based cantilevers for sensing, scanned probe and very high-frequency applications
M. Li, H.X. Tang and M.L. Roukes
25. **Nature Nanotechnology**, 2007, 2(2), 114-120.
A history of the development of CMOS oscillators: The dark horse in frequency control
M.S. McCorquodale and V. Gupta
in Frequency Control and the European Frequency and Time Forum (FCS), 2011 Joint Conference of the IEEE International, 2011.
26. *A study of phase noise in CMOS oscillators*
B. Razavi
27. **Solid-State Circuits, IEEE Journal of**, 1996, 31(3), 331-343.
A Nanoscale Parametric Feedback Oscillator
L.G. Villanueva, R.B. Karabalin, M.H. Matheny, E. Kenig, M.C. Cross and M.L. Roukes
Nano Letters, 2011, 11(11), 5054-5059.

Chapter 5

Synchronization

In the previous chapter we demonstrated the effect that nonisochronicity has upon a single feedback oscillator; here we will show the effects nonisochronicity has upon the interaction of two feedback oscillators. We show synchronization of two feedback oscillators when their mutual reactive weak coupling colludes with their nonisochronicity. In our system, we perform careful calibration of the relevant synchronization parameters used in the theoretical predictions. In the case of small coupling, this calibration gives analytical predictions which show close agreement with the experimental results. For large coupling, our predictions from numerical simulations show excellent agreement with experiment. In addition to phase locking behavior, phase slipping between two oscillators is observed in the time domain. Finally, data are presented showing an improvement in the oscillators' frequency precision between synchronized and unsynchronized states.

5.1 Introduction

The mutual entrainment of coupled self-sustained oscillators, the phenomenon known as synchronization, was observed as early as 1665 [1]. This phenomenon is not commonly observed in natural nonbiological oscillatory systems, since they, primarily, are quasi-conservative (e.g., astronomical phenomena), or driven (e.g., the ocean tides). However, in natural biological systems, synchronization is ubiquitous, ranging from ecological scales [2] to microscopic scales [3]. It is also known to play a key role in neural networks [4].

Since synchronization is so prevalent in natural systems, candidate systems are sought in which to observe and control this phenomenon. One well-understood candidate system is Josephson junction arrays [5], which exhibits dynamics described by the Kuramoto model [6]. Implementing these arrays is relatively easy, since a single voltage can be applied to many devices, whereby they oscillate. Oscillations in Josephson junctions reside in a one-dimensional phase space; they can be mapped by a single phase variable (they lack an amplitude component, as in equation (4.13)). Thus, these arrays are excellent at mapping out the phase dynamics of coupled oscillators. However, since Josephson junctions are one-dimensional, much of the dynamics displayed by self-sustained oscillators (which reside in two-dimensional phase space) will not be seen, such as Hopf bifurcations [7]. Other candidate systems which display more complex dynamics (involving both amplitude and phase) are currently under investigation.

For example, in spin-torque systems, nonisochronous oscillators [8] have been shown to lock [9, 10], but these studies do not show results for a wide range of the system parameters. Synchronization is especially important for frequency sources constructed from spin-torque oscillators, since they currently exhibit large phase noise [11].

In nanomechanical systems, there has been theoretical work [12] for large arrays of NEMS. However, there has not been much experimental work in nanomechanical systems. Much of the difficulty for doing a well-controlled experiment comes from not being able to set up self-sustained oscillators using these extremely small and lossy resonators. In 2005, the first self-sustained NEMS oscillator was developed [13] and studied in detail. It was constructed from a magnetomotively actuated and detected resonator solving the major challenge of achieving enough signal to background ratio, which was accomplished through a resistance bridge. In that study, the NEMS was immersed in a high magnetic field through the use of helium cooled superconducting magnets. Making arrays of these type of feedback oscillators is not simple since each device needs signal lines, increasing the number of ports into the low temperature system. Also, since coupling between two adjacent magnetomotively transduced NEMS devices is capacitive in nature, experiments are limited to attractive coupling.

One advantage of piezoelectrically actuated NEMS [14] over monopolar NEMS (with a single electrode, such as capacitively [15], magnetomotively [16], and thermoelastically [17] actuated NEMS) is the dipolar nature of the coupling mechanism, which can be tuned to be both positive or negative. Also, tuning parameters such as frequency [18] and nonlinearity [19] is relatively simple. To the author's knowledge, we present the first study where careful control and analysis of the phase locking of two nonisochronous oscillators has been performed. This is also the first study where synchronization has been shown in NEMS.

5.2 Feedback Oscillators with Multiple Feedback Loops

Since this study of synchronization of two oscillators uses coupling through additional feedback loops off chip, we present a brief description of oscillators with multiple feedback loops.

As laid out in sections 4.2 and 4.3, a limit cycle will occur when the right side of equation (4.4) is positive. Notice that the phase Δ determines how much energy is fed back per cycle into the resonator. Here, an overall phase shift of $\frac{\pi}{2}$ gives maximum amplitude.

Instead of just one feedback loop, suppose we add another feedback loop with different amplitude and phase. This can be represented by the amplitude equation

$$A' + \frac{A}{2} - i|A|^2A = i\frac{F(a)}{2}e^{i\Delta} \cdot e^{i\varphi} + i\frac{D(a)}{2}e^{i\theta} \cdot e^{i\varphi}, \quad (5.1)$$

where $D(a)$ is a feedback function in general different from $F(a)$, with its own phase θ . In equation (5.1) the second feedback is assumed to have the same frequency as the oscillator, but the feedback could be at integer multiples of the oscillator frequency, which can lead to new types of oscillators [19].

If the amplitude of oscillation is set by the saturation of the feedback F , so that the second loop is always linear, this feedback function is linear with $D(a) = d \cdot a$. With steady oscillation $a' = 0$, we get

$$\varphi' = \frac{F(a)}{2a} \cos \Delta + a^2 + \frac{d}{2} \cos \psi, \quad (5.2)$$

and

$$a = F(a) \sin \Delta + d \sin \theta. \quad (5.3)$$

We may now use the first feedback loop $F(a)$ to tune the damping and cause self-sustained oscillations, and use the second feedback loop d to tune the stiffness. This gives two control knobs: one to control the amplitude of oscillation (F), and one to control the frequency of oscillation (d).

5.3 Synchronization Equations for Two Oscillators

We start the synchronization discussion with the equations for two coupled nearly identical oscillators each described by the equations developed in chapter 4 for saturated oscillators. The quality factors, oscillator saturations, and nonlinear tuning parameters are the same for these two oscillators, with the difference being the resonant frequency of the NEMS device (given by δ_1 and δ_2) and coupling between the two oscillators (given by β). We therefore get

$$\frac{d\tilde{A}_1}{dT} = i \left(\frac{\delta_1}{2} + \lambda_{ii} Q |\tilde{A}_1|^2 \right) \tilde{A}_1 - \frac{\tilde{A}_1}{2} + \frac{s}{2} e^{i\varphi_1} + i \frac{\beta}{2} (\tilde{A}_2 - \tilde{A}_1), \quad (5.4)$$

and

$$\frac{d\tilde{A}_2}{dT} = i \left(\frac{\delta_2}{2} + \lambda_{ii} Q |\tilde{A}_2|^2 \right) \tilde{A}_2 - \frac{\tilde{A}_2}{2} + \frac{s}{2} e^{i\varphi_2} + i \frac{\beta}{2} (\tilde{A}_1 - \tilde{A}_2), \quad (5.5)$$

where λ_{ii} is the nonlinear frequency tuning coefficient from chapter 3, φ_i is the phase of oscillator i , and s is the saturation level. This term, in the uncoupled case, gives the amplitude of oscillation in the steady state (equation (4.15)). We will assume β is a real number, resulting in what is known as *reactive* coupling. This can be either repulsive ($\beta > 0$) which is the tendency for two nearby resonators to repel, much like two positive charges, or attractive ($\beta < 0$), which is the tendency for two nearby resonators to attract, as in the case of two unlike charges (or two capacitor plates with one plate charged). In the absence of feedback ($s = 0$) and nonlinear stiffness ($\lambda = 0$), Equations (5.4) and (5.5) represent two coupled, damped resonators: the solution for a driven resonator can be found in any undergraduate textbook on mechanics[20]. For the case of externally driven coupled resonators with nonlinear stiffness see reference [21].

To analyze equations (5.4) and (5.5) we first normalize the amplitude by the saturation ($A = \tilde{A} * s$) to get equations similar to the form found in references [7, 22, 23]. Equations (5.4) and (5.5) can be simplified by separating the complex amplitude into a real magnitude and phase (with $A_i = a_i e^{i\varphi_i}$, $\alpha = \lambda_{ii} Q s^2$) to get

$$a'_1 = -\frac{a_1}{2} + \frac{1}{2} + \operatorname{Re} \left(i \frac{\beta}{2} (a_2 e^{i(\varphi_2 - \varphi_1)} - a_1) \right), \quad (5.6)$$

$$a'_2 = -\frac{a_2}{2} + \frac{1}{2} + \operatorname{Re} \left(i \frac{\beta}{2} (a_1 e^{i(\varphi_1 - \varphi_2)} - a_2) \right), \quad (5.7)$$

$$\varphi'_1 = \frac{\delta_1}{2} + \alpha a_1^2 + \operatorname{Im} \left(i \frac{\beta}{2} \left(\frac{a_2}{a_1} e^{i(\varphi_2 - \varphi_1)} - 1 \right) \right), \quad (5.8)$$

and

$$\varphi'_2 = \frac{\delta_2}{2} + \alpha a_2^2 + \text{Im} \left(i \frac{\beta}{2} \left(\frac{a_1}{a_2} e^{i(\varphi_1 - \varphi_2)} - 1 \right) \right), \quad (5.9)$$

where the prime is the derivative with respect to slow time, T.

Phase locked solutions can be found by looking at the phase difference, $\varphi = \varphi_2 - \varphi_1$, which we find by subtracting equation (5.9) from equation (5.8). Together with equations (5.6) and (5.7) we get

$$a'_1 = -\frac{a_1}{2} + \frac{1}{2} - \frac{\beta}{2} a_2 \sin \varphi, \quad (5.10)$$

$$a'_2 = -\frac{a_2}{2} + \frac{1}{2} + \frac{\beta}{2} a_1 \sin \varphi, \quad (5.11)$$

and for the phase difference

$$\varphi' = \varphi'_2 - \varphi'_1 = \frac{\delta_2}{2} - \frac{\delta_1}{2} + \alpha a_2^2 - \alpha a_1^2 + \frac{\beta}{2} \cos \varphi \left(\frac{a_1}{a_2} - \frac{a_2}{a_1} \right). \quad (5.12)$$

Equation (5.12) can be simplified as

$$\varphi' = \Delta\omega - (a_1^2 - a_2^2) \left(\alpha + \frac{\beta}{2a_1 a_2} \cos \varphi \right), \quad (5.13)$$

where the parameter $\Delta\omega = \frac{\delta_2}{2} - \frac{\delta_1}{2}$. Notice that φ' is the beat frequency of the two oscillators, or the rate of advance of one oscillator in the rotating frame of the other oscillator frequency. Equations (5.10), (5.11), and (5.13) completely describe the synchronization dynamics of two heavily saturated oscillators in the slow time scale.

Let us note what the three parameters mean for these equations. The parameter $\Delta\omega$ is the resonator frequency difference (called ‘detuning’) in units of the resonator’s open loop response spectral width ($\Delta\omega = \frac{f_2 - f_1}{\bar{f}/Q}$ with $\bar{f} = \frac{1}{2}(f_1 + f_2)$), which is unitless. The parameter α is the nonisochronicity, or ‘shear,’ again in terms of the width, i.e., $\alpha = \lambda Q s^2 = \frac{\Delta f_i}{f_i/Q} \tilde{s}^2 Q^2$ (where $\frac{\Delta f_i}{f_i}$ is the quantity measured in Figure 3.4 (b,top), and \tilde{s} is the level of saturation in units of the resonator amplitude \tilde{x}). Finally, β is the coupling between the two resonators. This parameter can be found by observing the splitting of the in-phase and anti-phase mode frequencies when the uncoupled resonator frequencies are the same.

The locking mechanism comes from two different sources. The oscillators can lock due to an amplitude difference combined with shear (the first term in the second parentheses in equation (5.13)), or from amplitude difference without the shear (the second term in the second parentheses in equation (5.13)). We call these “shear-induced coupling” and “direct coupling”, respectively. Obviously, the shear-induced coupling is of particular interest for us since this is the locking mechanism which arises from the nonisochronicity.

5.4 Synchronization in the Limit of Small Coupling

In the limit of small coupling, the amplitudes do not deviate far from unity in equations (5.10) and (5.11). The fixed points of the amplitude are therefore

$$a_1 \cong 1 - \beta \sin \varphi, \quad (5.14)$$

and

$$a_2 \cong 1 + \beta \sin \varphi, \quad (5.15)$$

which gives for the phase equation

$$\varphi' = \Delta\omega + 4\alpha\beta \sin\varphi, \quad (5.16)$$

known as the Adler Equation [24]. Thus, with zero coupling we get $\varphi' = \Delta\omega$, i.e., the oscillator beat frequency is simply the resonator frequency difference. Here upon exchange of oscillator one with oscillator two, the equations remain the same. Hence, an inherent symmetry between the oscillators occurs.

It should be noted that in the case of small dissipative coupling (where in the original amplitude equation, the coefficient of the coupling term is real and the coupling affects the equation for phases directly), shear neither hinders nor helps the synchronization. For the more general solution with both reactive and dissipative coupling we get [7]

$$\varphi' = \Delta\omega + (4\alpha \operatorname{Re}(\beta) + \operatorname{Im}(\beta)) \sin\varphi. \quad (5.17)$$

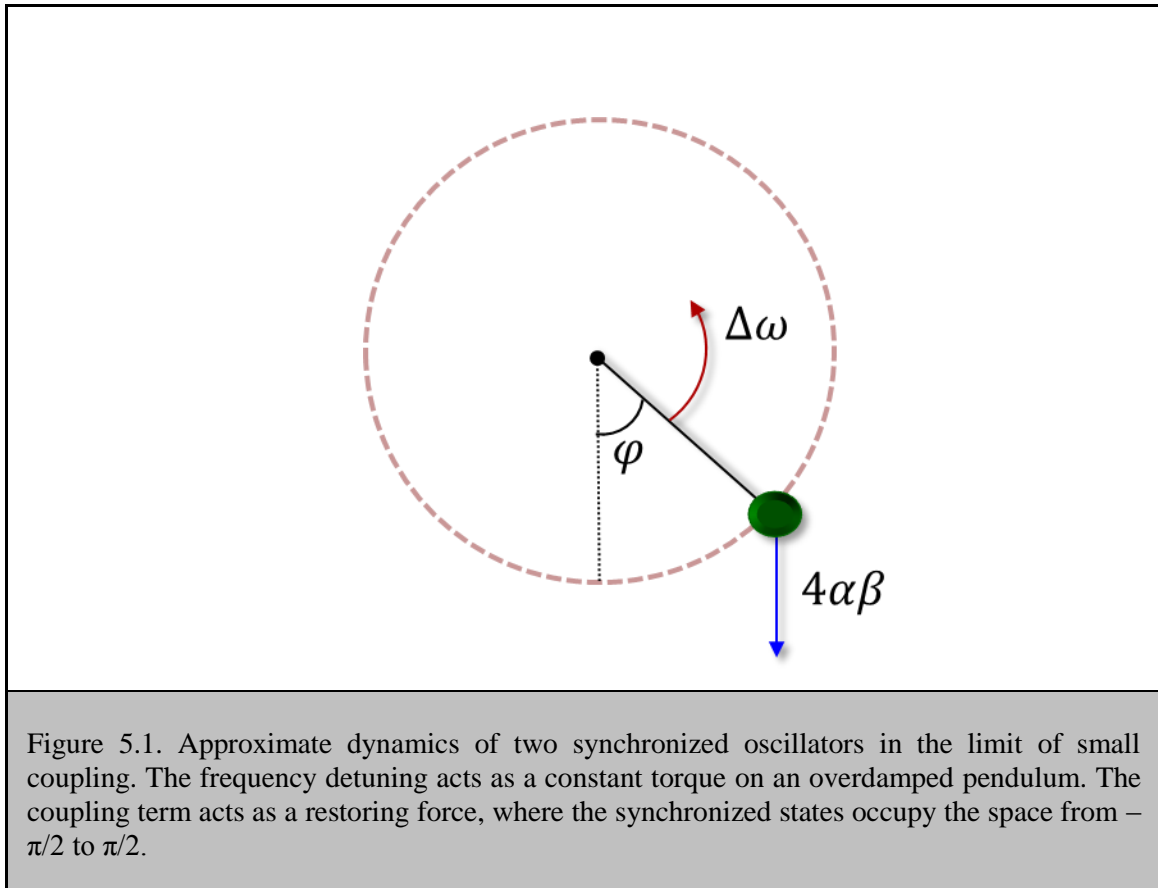
Therefore, since it is the goal of this study to understand the role of nonisochronicity, dissipative coupling is ignored.

To get a basic understanding of phase dynamics implied by (5.16), we map it onto an easily understandable physical system, a heavily damped rotating pendulum under constant torque (see Figure 5.1). Although this picture is not immediately intuitive (since we ignore the inertia), it can provide some insight. In the heavily damped pendulum without the inertial term we get

$$\gamma\dot{\varphi} = \tau - mg\sin\varphi \Rightarrow \dot{\varphi} = a - b\sin\varphi \quad (5.18)$$

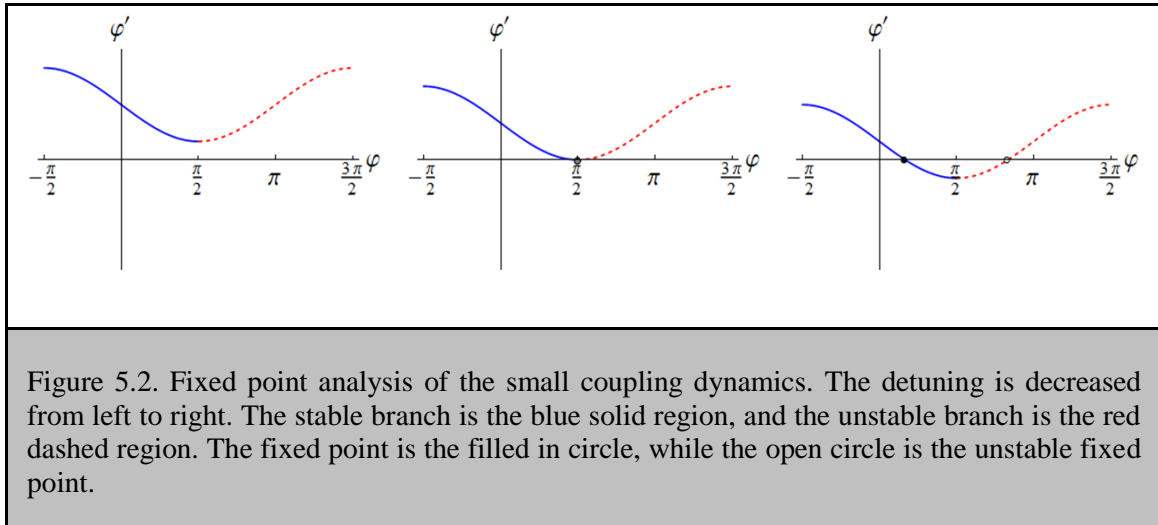
with the meanings of a and b being obvious. When the torque term a is much greater than the gravitational term b , the pendulum will smoothly rotate with uniform motion. As we turn down the torque (in the coupled oscillators this is the detuning), the gravitational term (in the oscillator system the coupling term) will slow the pendulum around the bottom of the cycle ($\varphi = 0$), the stable fixed point. Also, at the top, at the unstable fixed point, the gravitational potential speeds up the pendulum as it moves down. This motion will no longer be uniform and smooth; it exhibits periodic skips in phase. As the torque decreases further, the system eventually cannot escape from the potential well and relaxes to the bottom of the rotation.

In the coupled oscillators near the onset of synchronization, the motion also becomes non-uniform, like a ball skipping down a washboard potential (see section 5.11). The non-uniformity in the motion will cause frequency modulation of the two oscillator signals, which increases as the system gets closer to the synchronization regime. At the border of synchronization, there exists long periods of time where the motion appears steady and then suddenly jumps to the next cycle. This is known as phase slipping.



The transition of moving from the unsynchronized to the synchronized states creates fixed points in the system through a saddle-node bifurcation. This is diagrammed in Figure 5.2 with attractive coupling ($\beta < 0$). We plot oscillator frequency difference φ' (given by equation (5.16)) against the phase difference φ . As we change the frequency detuning $\Delta\omega$ we shift the whole curve down, and eventually create solutions where the oscillator frequency difference φ' can be zero. There are two solutions, a stable and an unstable one; the stability is given by the slope of the curve at those points. For the point in the region with a negative slope, the fixed point is stable, since small perturbations cause the phase to decay. In the region with a positive slope sits the unstable fixed point, since perturbations grow in time. Note that as we flip the sign of this curve by inverting the sign of the coupling, the stable point flips to the unstable fixed point. This

analysis of fixed points can be generalized to include higher dimensions with than one variable; this is known as linear stability analysis (LSA).



Assuming that the shear is always positive, we have different states depending on the sign of β . For repulsive coupling ($\beta > 0$) we get a stable fixed point when $\frac{\pi}{2} < \varphi < \frac{3\pi}{2}$, which we call the antiphase solution, since near $\Delta\omega = 0$ the stable fixed point for the ‘anti-phase’ state gives $\varphi = \pi$. The other state can be found with attractive coupling ($\beta < 0$), which gives the ‘in-phase’ state, $-\frac{\pi}{2} < \varphi < \frac{\pi}{2}$.

Note that changing the sign of $\Delta\omega$ is equivalent to reversing time. To understand this, say we take $\Delta\omega > 0$ in the in-phase solution at the bifurcation, $\varphi = \frac{\pi}{2}$, then $\varphi_2 = \varphi_1 + \frac{\pi}{2}$, and so oscillator 2 ‘leads’ oscillator 1. In the anti-phase solution, $\varphi = \frac{3\pi}{2}$ and so oscillator 1 leads oscillator 2, but this could be viewed such that time is just reversed with oscillator 2 leading oscillator 1 in the other direction.

Even though equation (5.16) is nonlinear, it can be explicitly solved. The beat frequency in the unsynchronized region is

$$\varphi' = \Omega = 2\pi \left(\int_0^{2\pi} \frac{d\varphi}{\Delta\omega + 4\alpha\beta\sin\varphi} \right)^{-1}, \quad (5.19)$$

which gives

$$\Omega = \sqrt{\Delta\omega^2 - (4\alpha\beta)^2}. \quad (5.20)$$

Equation (5.20) gives a square root cusp in the beat frequency Ω around the regime of synchronization. The regime of synchronization is $-\Delta\omega_{sync} < \Delta\omega < \Delta\omega_{sync}$ with

$$\Delta\omega_{sync} = -4\alpha\beta. \quad (5.21)$$

As the detuning is increased from zero, the sine of the phase difference between the oscillators in the synchronized state becomes non-zero and the amplitudes change. We solve (5.14) and (5.15) in the synchronization region,

$$\left| \frac{\Delta a_i}{a_i} \right| = \beta \sin \varphi = -\frac{\Delta\omega}{4\alpha}, \quad (5.22)$$

where the solution for the phase equation (5.16) for $\varphi' = 0$ has been inserted. As β becomes larger, the approximation for small changes in amplitude no longer holds, and we have to take into account the nonlinear changes in the amplitudes as a function of the detuning.

5.5 Amplitude Limitations

The equations for amplitude ((5.10) and (5.11)) for large coupling cannot be as easily analyzed as in the case of small coupling. The fixed points of the amplitude equations in the synchronization region give

$$a_1 = 1 - \beta a_2 \sin \varphi, \quad (5.23)$$

and

$$a_2 = 1 + \beta a_1 \sin \varphi. \quad (5.24)$$

Eliminating the phase from these equations yields

$$a_1(a_1 - 1) = -a_2(a_2 - 1) \Rightarrow a_1^2 + a_2^2 - a_1 - a_2 = 0, \quad (5.25)$$

which gives solutions

$$a_{1,2} = \frac{1}{2} \pm \sqrt{\frac{1}{4} - a_{2,1}(a_{2,1} - 1)}. \quad (5.26)$$

Physically, as oscillator 1 amplitude a_1 increases, oscillator 2 amplitude a_2 decreases. Only positive solutions are physical.

Note that for a real solution of equation (5.26) $a_{1,2} \leq \frac{1+\sqrt{2}}{2}$. For $a_2 = 1$, we get $a_1 = 1$, as expected. For $a_2 = \frac{1+\sqrt{2}}{2}$, $a_1 = \frac{1}{2}$, which means the ‘exchange’ of amplitudes is not generally symmetric. The reason for this symmetry breaking lies in the fact that no longer can we do the same exchange of oscillator number (as we did before in the small coupling case). Here, equation (5.13) flips sign if we exchange oscillator 1 and oscillator: the oscillators have ‘identity’ specified by the sign of the frequency detuning. We plot the solution curve for the oscillator amplitudes in Figure 5.3.

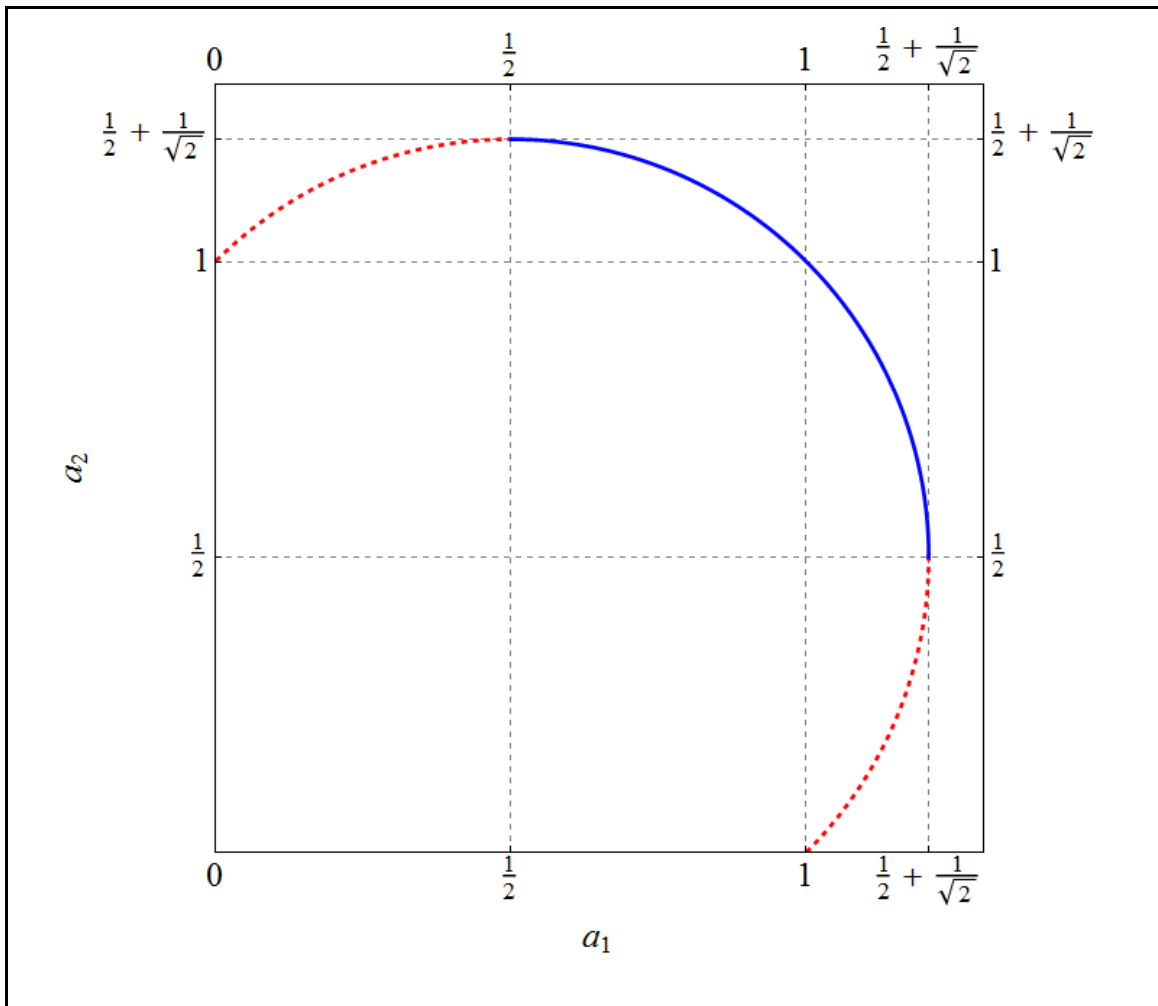


Figure 5.3. Amplitude space for the two oscillators. The solid blue and dashed red sections are the regions where the sign of equation (5.26) is positive and negative, respectively.

To know which values of amplitude are stable for fixed shear and coupling, we do a linear stability analysis (LSA) [25] of the system by finding the eigenvalues of the Jacobian of equations (5.10), (5.11), and (5.13). In Figure 5.4 we show the eigenvalues, both real (solid) and imaginary (parts) for $\beta = 0.9$ and $\alpha = 1.25$. For stability, all three real parts must be negative. This occurs for $0.56 \leq a < 1.21$, which is the region where stable amplitudes can occur.

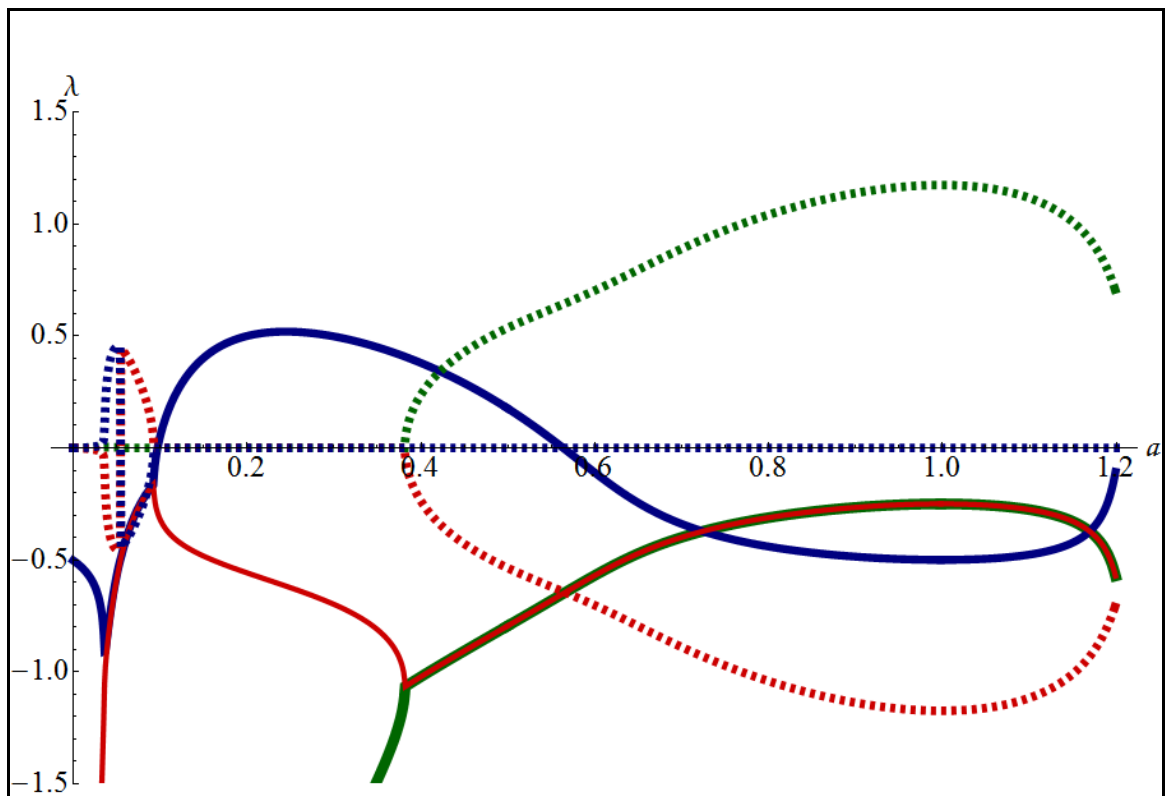


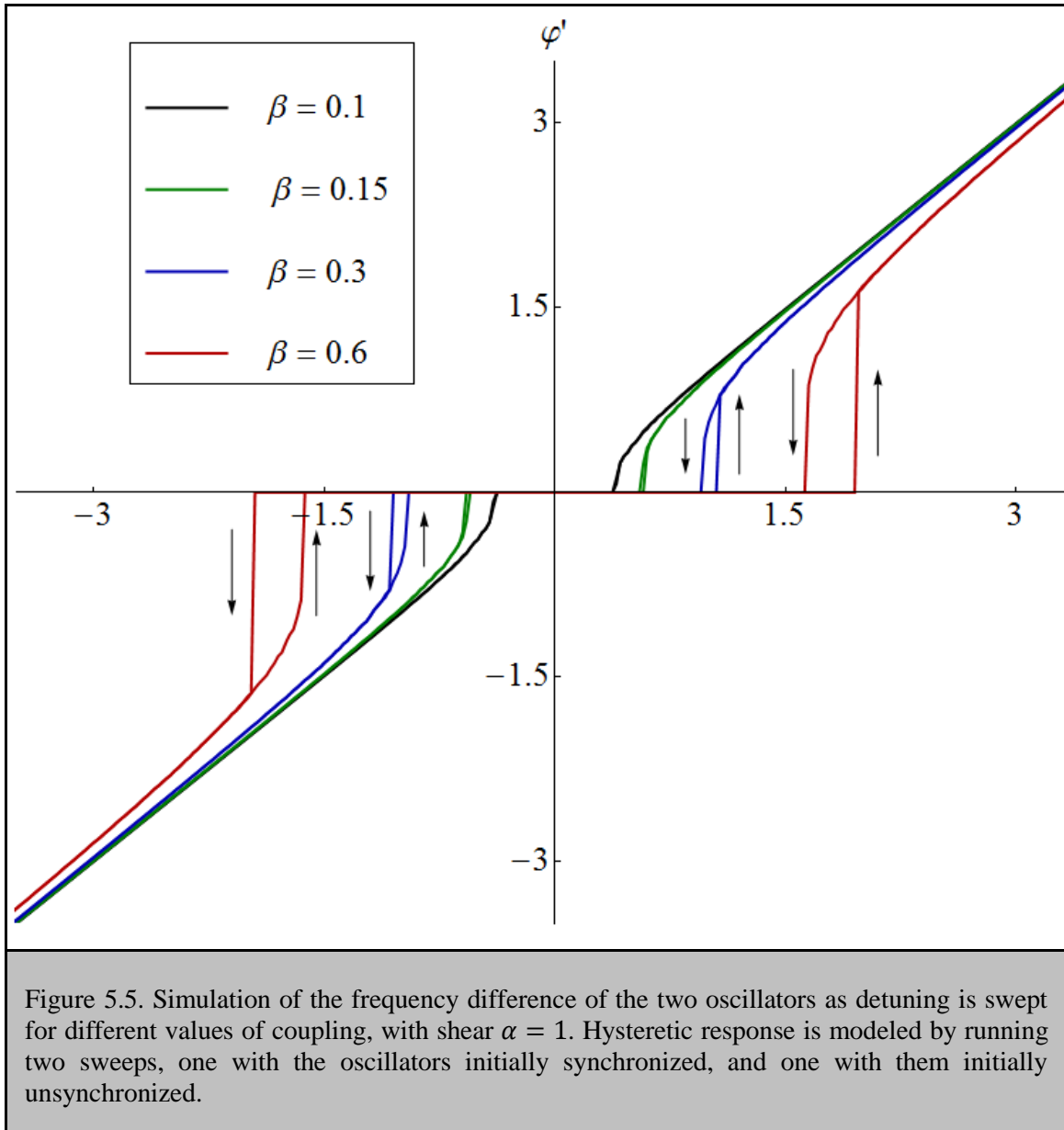
Figure 5.4. Eigenvalues for the Jacobian of equations (5.10), (5.11), and (5.13) with $\beta = 0.9$, $\alpha = 1.25$. The real and imaginary parts of the eigenvalues are given by solid and dashed lines, respectively. The solution is unstable at $a \cong 0.56$ since two of the real parts of the eigenvalues become positive at this point.

Since the amplitude difference is limited to this region, there exists a limit of the amount of coupling available in the phase equation (since both the shear and direct coupling terms from equation (5.13) require an amplitude difference to cause frequency locking). Once these limits are reached, the solution becomes unstable and unsynchronizes.

5.6 Simulations of Synchronization with Large Coupling

There is no analytic expression for a general solution to the full set of equations (5.10), (5.11), and (5.13), but we can simulate their behavior using Mathematica and Matlab.

In Figure 5.5 is a plot of a sweep of $\Delta\omega$ from -3.5 to 3.5 for different values of coupling β with shear $\alpha = 1$.



As the coupling β increases, we note the bifurcation to the synchronized state shows hysteresis on changing the direction of sweep. In Figure 5.6, we show another example of this hysteresis but with a Q factor difference between the two oscillators of 10%. Here the symmetry is broken between positive and negative values of $\Delta\omega$. This will also occur in two oscillators with different saturation values.

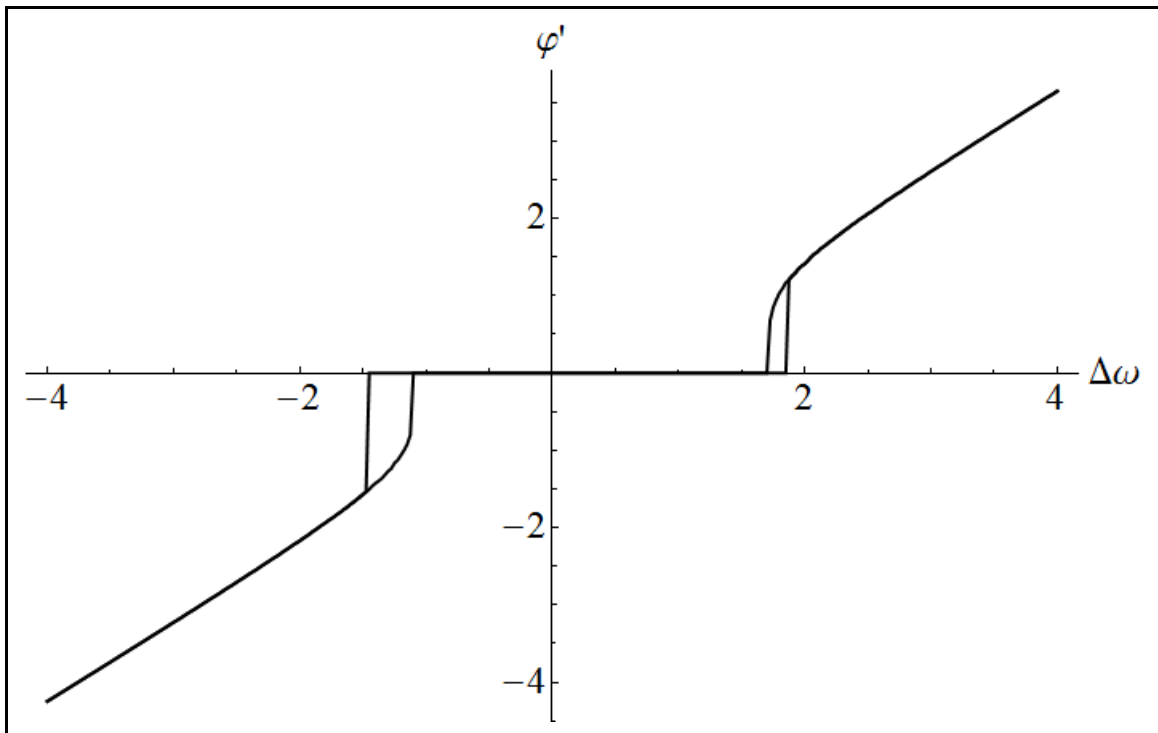


Figure 5.6. Detuning sweep with a resonator Q difference of 10% which displays an obvious asymmetry in both synchronized regime and hysteretic region size between negative and positive values of detuning.

5.7 Realization of Two Coupled Oscillators

It is possible to achieve the coupling described by equations (5.4) and (5.5) through an electrostatic mechanism, as in reference [26]. However, in piezoelectrics, by using this coupling mechanism, we would also be changing frequency. We would then have two parameters in our experiment changing at the same time, increasing experimental complexity. Also, since we use impedance bridge in order to create a differential signal at the output of each oscillator, feedthrough signals between the oscillators would not be nulled since each oscillator's impedance bridge is tuned in a different way. Thus, eliminating cross coupling would be impossible unless parasitic capacitances between the bonding pads could be significantly reduced. Finally, finding

two devices that are exactly the same (in terms of frequency, quality factor, nonlinearity, tuning range, and insertion loss) is difficult given our fabrication capabilities.

Here we develop a method by which experimental verification of the synchronization phenomena described in equations (5.10), (5.11) and (5.13) can be carried out without the complications described in the previous paragraph. In this work we employ an additional feedback loop to couple the oscillators together (similar to the methods describe in section 5.2). Although there is time delay between the amplitude of the resonator and the feedback signal, it can be ignored for delays smaller than the decay time (ϵf_0) since the feedback signal is effectively instantaneous on the slow timescale. Therefore, we do not have to include it into equations (5.4) and (5.5).

In Figure 5.7, we show the experimental setup with a “coupling loop,” which creates an effective coupling through feedback in the amplitude equation. We will show how this coupling is calibrated in the next section. All of the data except phase slipping and noise data, was taken using two separate spectrum analyzers. The amplitudes are monitored for several reasons: to verify equation (5.22), to calibrate the shear parameter α , and also to ensure that our oscillators are identical.

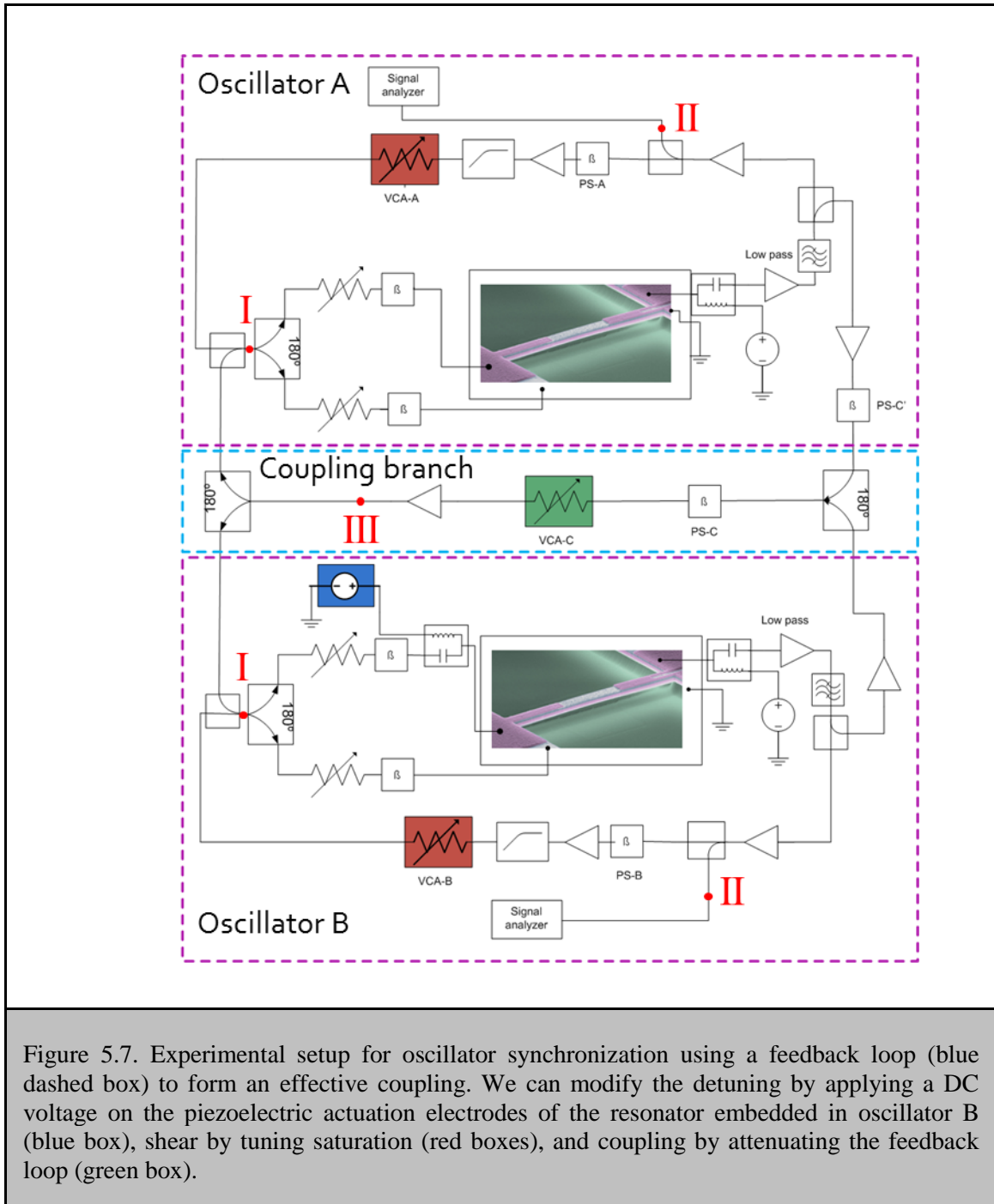


Figure 5.7. Experimental setup for oscillator synchronization using a feedback loop (blue dashed box) to form an effective coupling. We can modify the detuning by applying a DC voltage on the piezoelectric actuation electrodes of the resonator embedded in oscillator B (blue box), shear by tuning saturation (red boxes), and coupling by attenuating the feedback loop (green box).

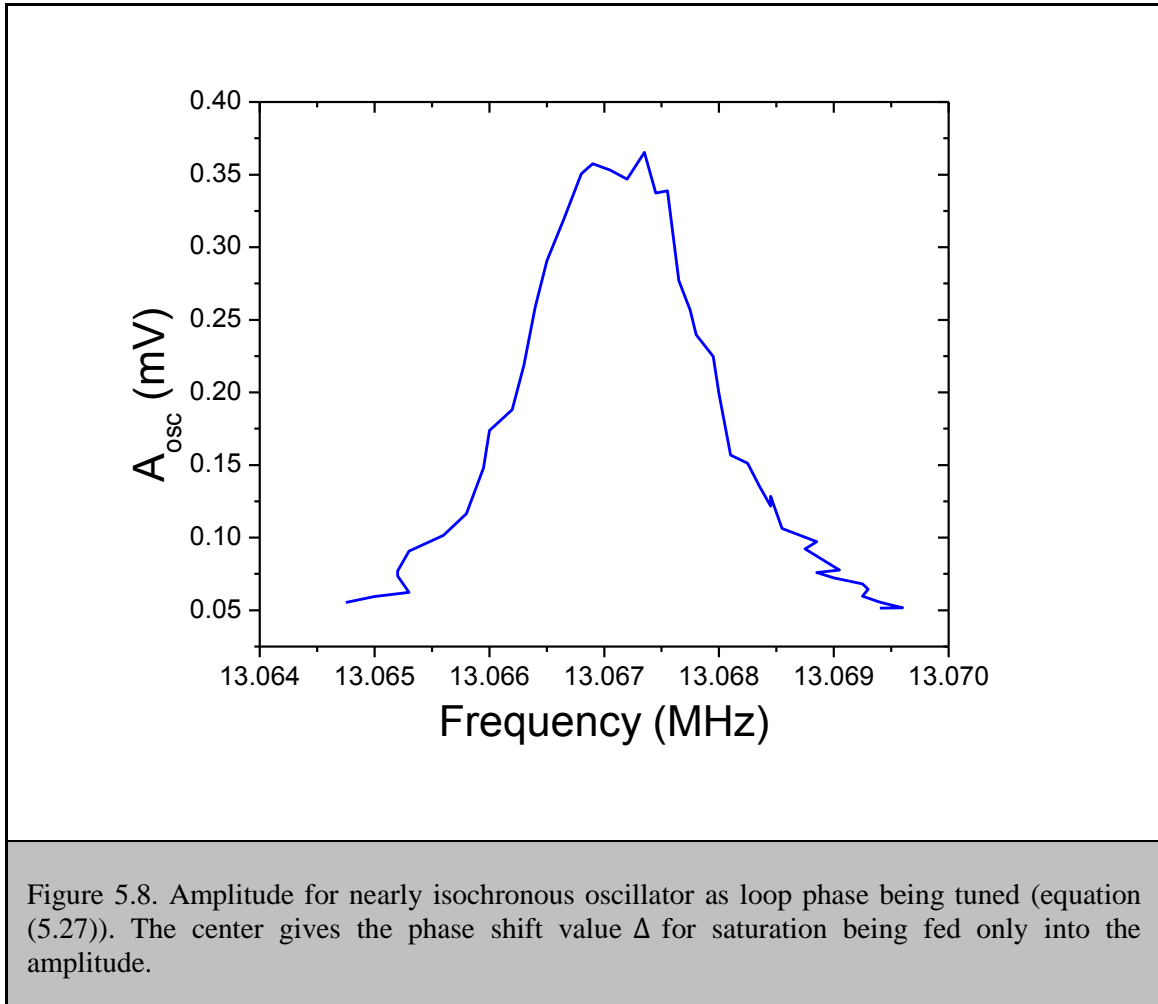
5.8 Calibration of Parameters

Extracting the three parameters which set the dynamics $(\Delta\omega, \alpha, \beta)$ from the setup requires care if we wish to compare theoretical predictions to the experimental results. Before calibrating the parameters, each closed loop oscillator feedback phase was varied using voltage controlled phase shifters PS-A and PS-B so that the loop phase shift was set for maximum oscillation amplitude ($\Delta = \frac{\pi}{2}$ in equation (5.2)). This was done to ensure the feedback loops used to cause oscillation (Figure 5.7, dashed purple boxes) altered only the oscillator amplitude (equations (5.6) and (5.7)), and not oscillator phase (equations (5.8) and (5.9)). Frequency and amplitude of one of the oscillators is shown in Figure 5.8 as the phase shifter PS-A is tuned (which shifts the feedback loop phase Δ in equation (5.1)).

In Figure 5.8 saturation is low, so the curve traced out is Lorentzian. This is predicted to occur in saturated oscillators with no nonlinear stiffness, since the signal fed back into the resonator is constant for any given frequency. Combining equations (4.15) and (4.16) with no nonlinear stiffness (ignoring the s^2 term in the equation (4.16)) gives

$$a^2 = \frac{s^2}{1 + 4\Omega^2}, \quad (5.27)$$

for slow time deviation frequency Ω . When $\Delta = \frac{\pi}{2}, \Omega = 0$, giving the maximum of equation (5.27).



Calibration of the shear is straightforward and is related to the work described in chapters 3 and 4. By tuning the attenuators after the limiter (red in Figure 5.7) we can change the saturation level and gain. Given that the gain is sufficiently high, such that the signal is strongly saturated, the change in gain can be ignored. We can therefore measure the saturation level by measuring the peak output amplitude (when the oscillators are far outside the synchronization regime) and dividing by the quality factor found in open loop resonance. We calibrate the oscillator amplitude, in units of displacement, at point II of Figure 5.7 by the methods outlined in chapters 2 and 3,

whereby we can also calibrate the nonlinear tuning coefficient λ . Recall that the shear is combination of saturation and nonlinear stiffness, i.e., $\alpha = \lambda Qs^2$. Thus, alpha can be tuned either by causing beam deflection, which changes λ (such as in section 3.6), or by simply changing the saturation level s . This parameter α can be understood as the amount of frequency change the oscillator undergoes under unit change in the square amplitude (according to the second term in equations (5.8) and (5.9)). So, for example, $\alpha = 1$ means that if the oscillator doubles in amplitude, the frequency shifts by 4 times the open loop width.

We present two different ways of measuring the detuning $\Delta\omega$ for the experiments below, depending on which parameter is swept.

When the coupling is swept, the difference in frequency is found by simply looking at the frequency difference in the uncoupled case. Since the two oscillators are not interacting, they should be identical in all variables except frequency, which are completely determined by shear and open loop frequency. Since amplitude and shear are the same for both oscillators, the difference in oscillator frequency is the difference in resonator frequency.

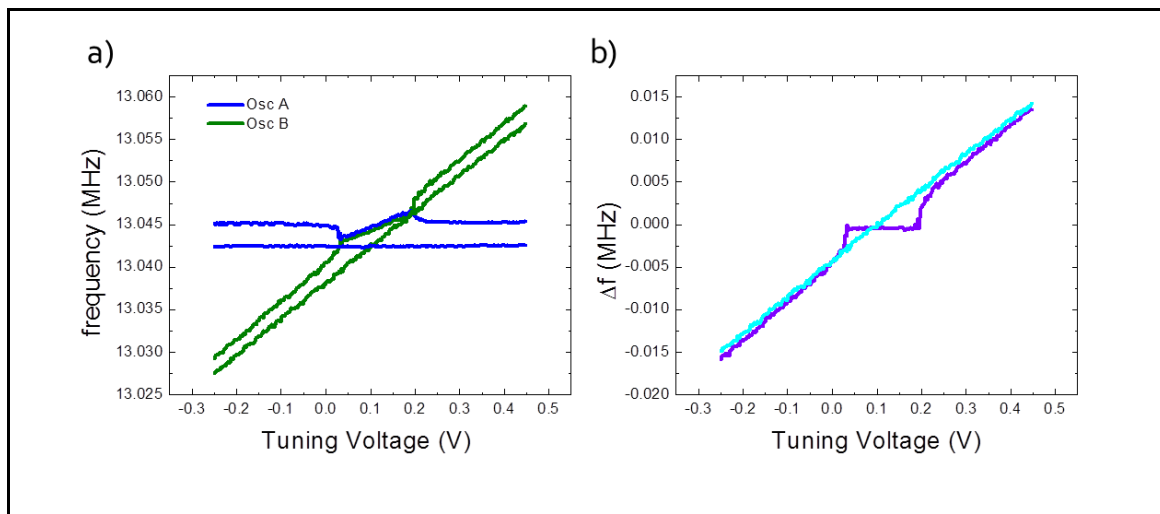


Figure 5.9. (a) Raw data of the two oscillators as one of the oscillators is tuned in frequency, for two different coupling strengths. (b) The same sweeps but plotting the difference frequency. The end of this plot gives a straight line to which detuning can be calibrated.

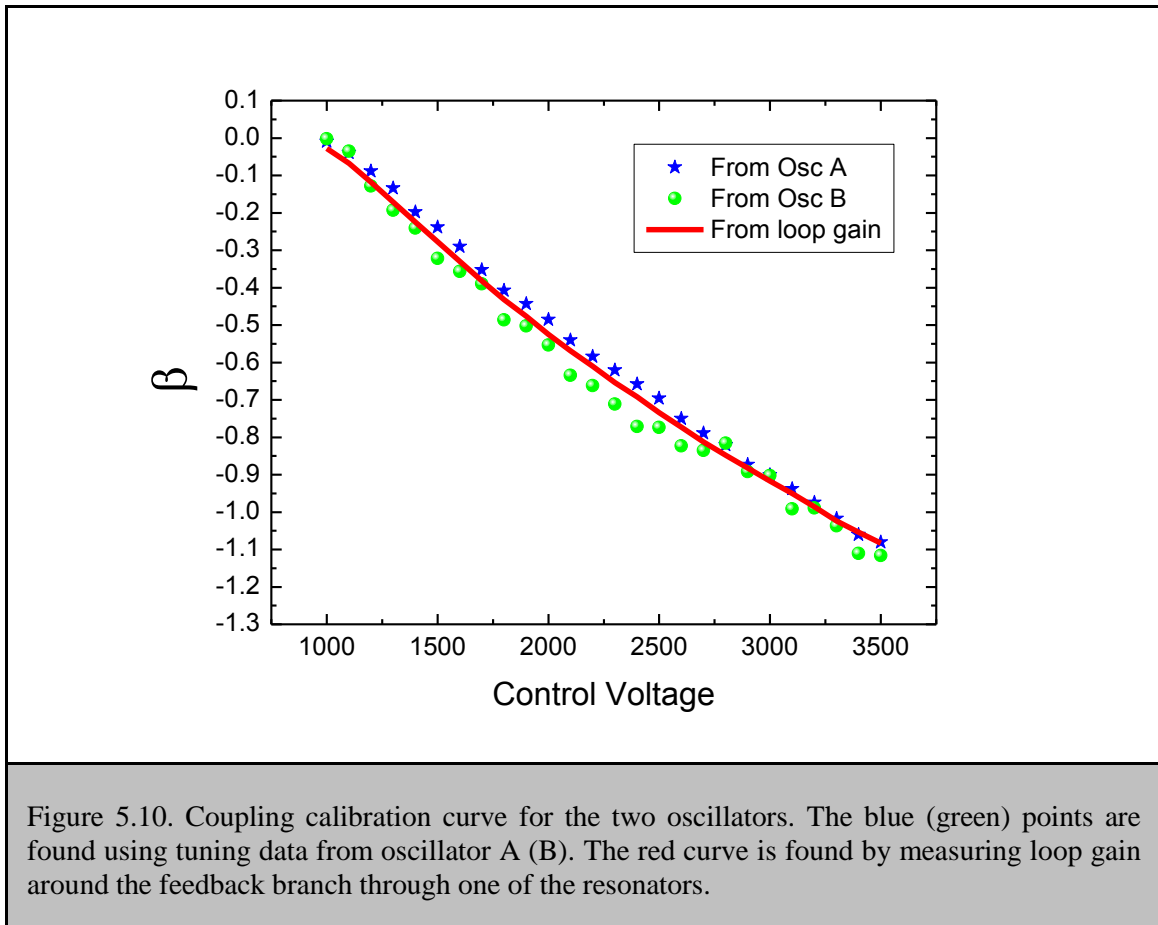
When the frequency difference is swept (through the use of a dc voltage coupled to the input electrode of the resonator embedded in oscillator B in Figure 5.7 (blue box)) we fit the outer 5% of data points of tuning voltage versus ϕ' (at detunings very far from zero) in the sweep to a straight line, since the two oscillators are approximately noninteracting at those points. The resonator frequencies are linear in piezoelectric tuning voltage [14], so we can replace the voltage with the resonator frequency difference. The detuning is the ratio of resonator frequency difference to the width $\Delta\omega = \frac{\Delta f}{f/Q}$. In Figure 5.9 (a), we show the raw data for frequency of the two oscillator from two sweeps with different coupling. The synchronized regime can be seen as the points where the frequency difference is zero. One pair of curves has a very small synchronization regime, due to small coupling; the other pair has a much larger regime since its coupling is larger. Note that near the ends of the data, the frequencies are essentially linear with the tuning voltage. The linear relationship between voltage and resonator frequency difference is given by the slope of the line fitted to the data points far away from the synchronization regime. We can thus scale the x-axis of these plots to give the detuning $\Delta\omega$.

In Figure 5.9 (b), we show the frequency difference of the two sets of curves. Note that for the two curves in (b) the frequency difference is different for the same piezoelectric tuning voltage far outside the synchronization regime. The time between these measurements is on the order of a couple hours, thus allowing frequency drifts to set in. We take the y-axis intercept of the linear fits of the previous paragraph and subtract it from the data.

Finally, we must explain the calibration of the coupling parameter. There are many ways to calibrate this parameter. Here we will show two such methods, and that these measurements agree.

For the first method, by measuring the open loop gain (with $\psi = \pi/2$) of the coupling loop (breaking the circuit at point III in Figure 5.7 and measuring gain ‘round trip’ through the circuit), we can measure this parameter directly. In this method the phase shift in the coupling loop is adjusted before taking data to ensure that the signal acts only as a reactive coupling, and not a dissipative one.

Another way of measuring the coupling which does not break the circuit (which can change the circuit impedances) is to measure oscillator frequency shifts when they are not interacting with each other. With only one oscillator turned on, the oscillator can be modeled by equation (5.2) and exhibits a frequency shift of $-\beta/2$, where d has been substituted by β . By making sure the amplitude does not change (the phase shift is set by tuning PS-C and PS-C’ to yield reactive coupling with the correct sign), we measure the frequency (in units of resonator width) as we change the voltage on the attenuator in the coupling loop. Below, in Figure 5.10 are the results of one such set of measurements.



In Figure 5.10, data from that both methods are within 10%. We choose to use the ‘gain’ method since we have more data points in that sweep. Additionally, the large frequency drifts of the oscillators in closed loop tend to cause larger systematic error in the results for β than what is caused by amplitude drifts in the driven ‘gain’ method.

5.9 Experimental Resonator Parameters

In the experiment, devices were selected such that the parameters were nearly identical. In Table 5.1 we show the experimental parameters of the two resonators. Note that the devices came from the same fabrication run and design.

Parameter	Device "A"	Device "B"
Frequency, f_0	13.073 MHz (@128mV)	13.066 MHz (@124mV)
Q factor	1590	1700
Nonlinear stiffness, λ	$1.55 \times 10^{13} \text{ m}^{-2}$	$1.35 \times 10^{13} \text{ m}^{-2}$
Insertion Loss, S_{21}	-63dB	-66dB

Table 5.1. Relevant properties of the resonators used to make oscillators A and B.

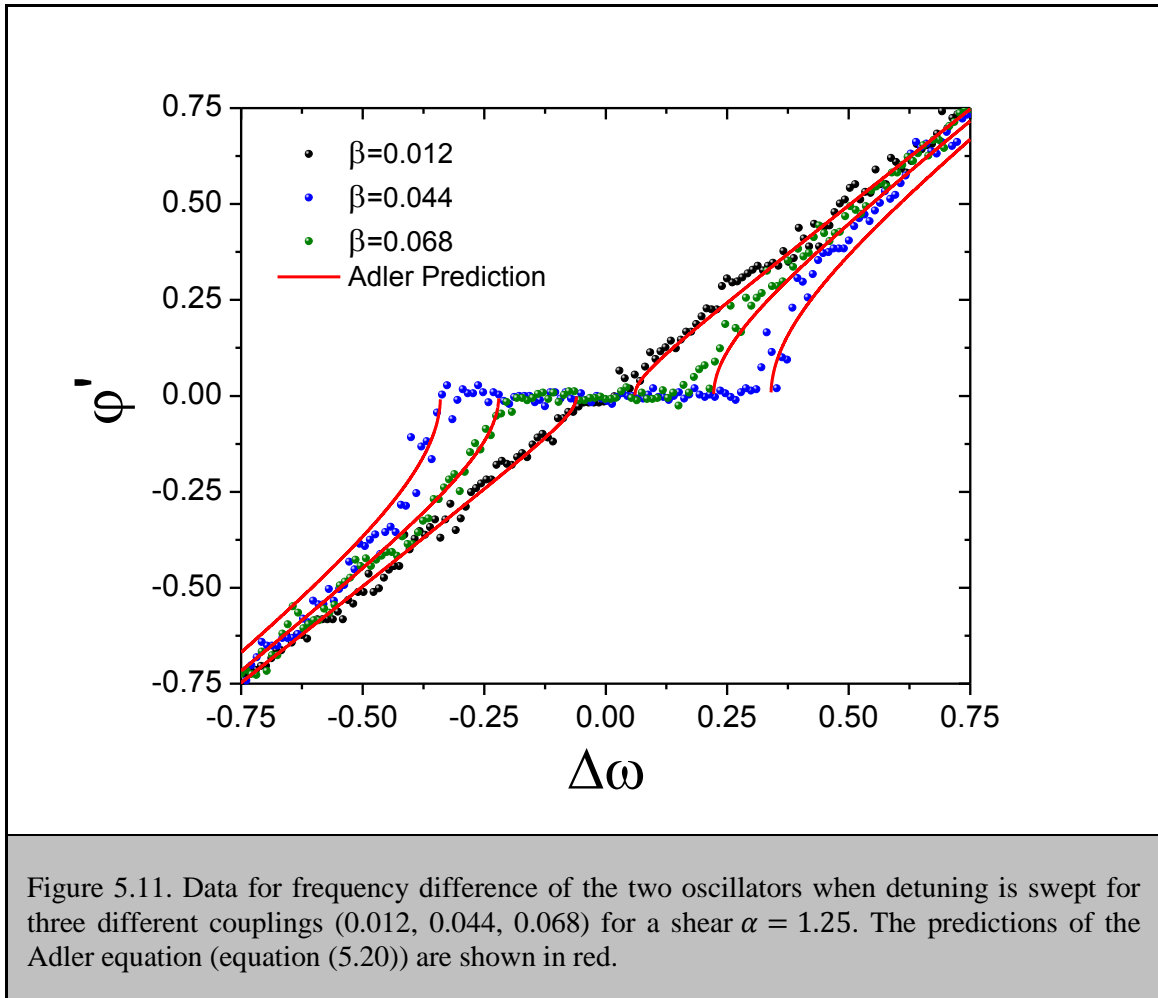
In chapter 4, it was pointed out that loop gain includes insertion loss of the resonator. In our experiment, differences in the insertion loss (as defined in chapter 4) could cause a problem with the synchronization dynamics, since the coupling loop (as opposed to the heavily saturated feedback loops which determine the oscillation amplitude) depends on loop gain. If the insertion loss is different for each oscillator going through the coupling loop, then a symmetric coupling β in equations (5.4) and (5.5) would not be possible. A more general case would have to be examined with a coupling matrix. The matrix would have indices given by β_{ij} which describes the linear feedback due to the coupling loop from resonator i into resonator j (with $i, j = 1, 2$). In order to simplify our analysis and model a system with symmetric coupling, we correct for the difference in insertion loss by attenuating each loop so that the open loop gains from point III back around to point III are the same.

From Table 5.1, we see that the resonator frequencies are extremely close (within 1 open loop spectral line width), and the nonlinear stiffnesses are within 10%. The difference in nonlinear stiffness can be compensated by changing the saturation (since shear α depends both on the saturation and the nonlinear stiffness). The quality factor, however, cannot be tuned, and is critical when looking at the symmetry between negative and positive frequency detuning (as pointed out in section 5.5).

The electronic parts of the two oscillators were built with identical elements (amplifiers, phase shifters, couplers, splitters, attenuators), so that the oscillators would be as similar as possible. The slight differences in attenuation, used to correct for the differences in nonlinear stiffness and insertion losses, were small.

5.10 Frequency Sweeps in the Limit of Weak Coupling

Keeping the coupling low we can test the predictions of the Adler equation (5.20). In Figure 5.11, we plot the frequency difference of the two oscillators as detuning is swept for several small values of β , keeping the saturation fixed at a value giving $\alpha = 1.25$.

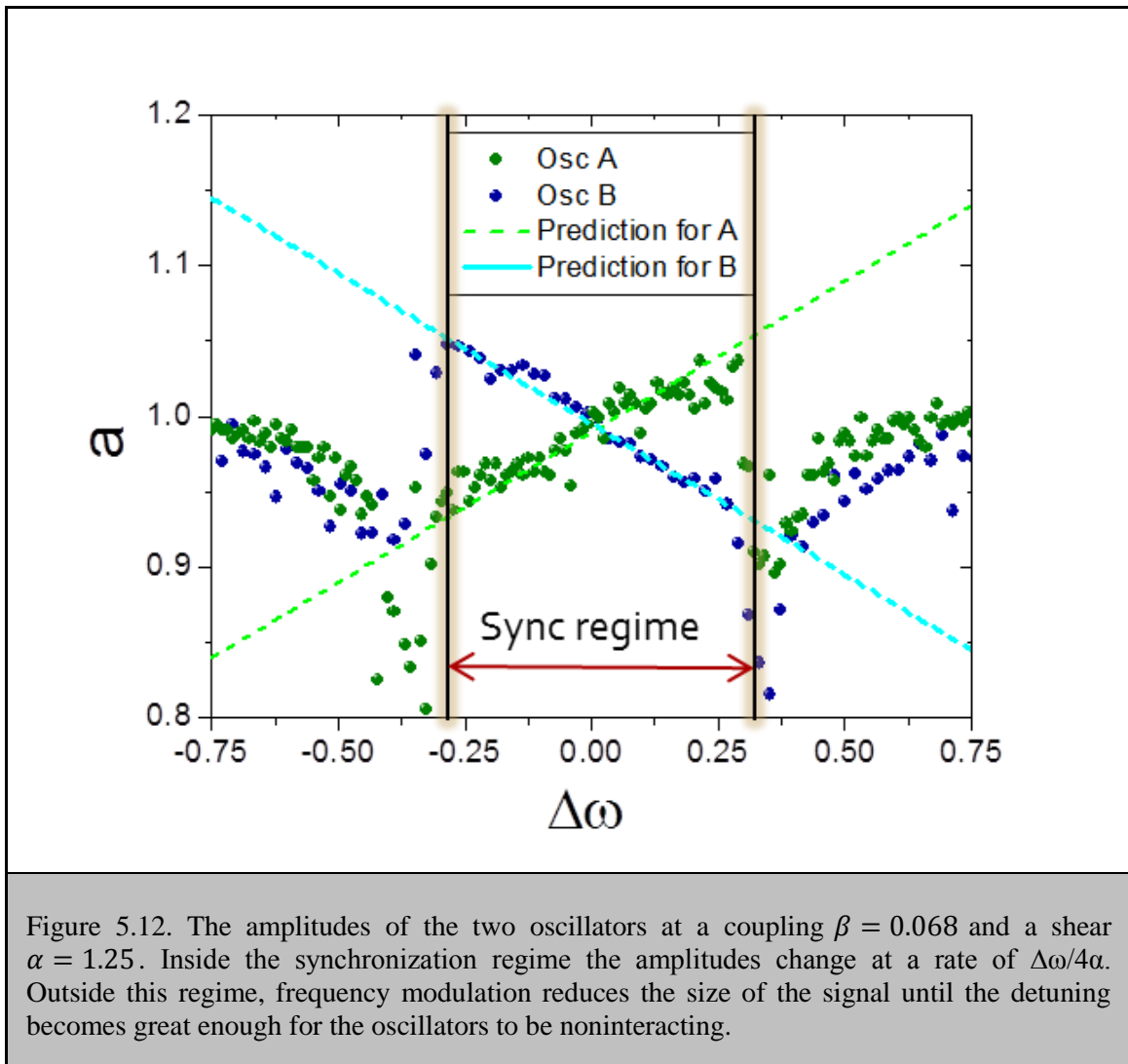


In black is the data, where each point is averaged over 1 second. The data has been shifted (not scaled) so that the synchronization region is symmetric about zero detuning. The values for the coupling parameter β in the experimental data are 0.012, 0.044, and 0.068. The red lines are predictions using the Adler equation (5.20). We see excellent agreement between the predictions and the experimental data, implying that our approximation for low coupling describes the experiment well.

We now look at the oscillator amplitudes. Within the synchronization regime, in the small coupling limit, equation (5.22) makes predictions for the slope of amplitude a versus detuning

$\Delta\omega$, which depends on shear, but not on coupling. In Figure 5.12, we show one sweep at $\beta = 0.068$. The prediction here also agrees well with experiment.

The results presented in Figure 5.11 and Figure 5.12 verify our calibration. The beat frequency in Figure 5.11 is predicted from the detuning, coupling, and shear, while the predictions of slope of the lines in Figure 5.12 need only be predicted from the detuning and shear. If we believe the scaling for the detuning is valid, then the shear must also be correct from Figure 5.12. Then if we trust our values for the detuning and shear, then from Figure 5.11 the value for the coupling must also be correct.



Both the amplitude and beat frequency results are impressive since it is extremely difficult to make *quantitative* predictions that agree so well with experiment in synchronization dynamics. Other studies in reactively coupled oscillators have shown frequency locking [9], but have not been able to so clearly match those to analytical theory. No results have been published on synchronized oscillator amplitudes before this study, and here we have excellent agreement between the quantitative predictions and the experiment.

However, these results encompass only the average or steady state dynamics of the system and not the full behavior for two coupled oscillators in the low coupling limit. Next, we discuss an aspect of the time domain phenomena at the border of synchronization, phase slipping.

5.11 Phase Slipping on the Border of Synchronization

We investigated the phenomena of phase slipping by mixing the oscillator signals through a circuit with calibrated output, which is set so that small deviations of phase give units of 2π , i.e., $Z_{out} = 2\pi \sin[(\omega_1 - \omega_2)t] = 2\pi \sin[\varphi'T]$. In Figure 5.13 (a), we show the mixed signal versus time as the detuning is stepped, with coupling $\beta = 0.068$. From the bottom (dark green) of Figure 5.13 (a), we start at large values of positive detuning, and see an approximately sinusoidal signal. As the detuning is reduced, the frequency starts to decrease. The slips become more aperiodic until the oscillators lock (dark red flat line). As the detuning is taken to negative values, the slips start up again, but switch polarity. In Figure 5.13 (b), we plot the average number of slips per unit time divided by the open loop resonance line width versus detuning.

We can explain this behavior by treating right side of equation (5.16) as a force, so that

$$\varphi' = f(\varphi) = \frac{dV}{d\varphi}, \quad (5.28)$$

with potential V defined by

$$V = \Delta\omega\varphi - 4\alpha\beta\cos\varphi. \quad (5.29)$$

This gives a washboard potential with the average slope defined by the detuning and the trapping component given by the coupling. We diagram equation (5.29) in Figure 5.13 (c). As detuning decreases, we can see that the particle goes from skipping periodically down each well until finally it gets trapped into a potential minimum. If we introduce a noisy force, then the particle has a chance to bounce out of the well, and thus create aperiodic behavior.

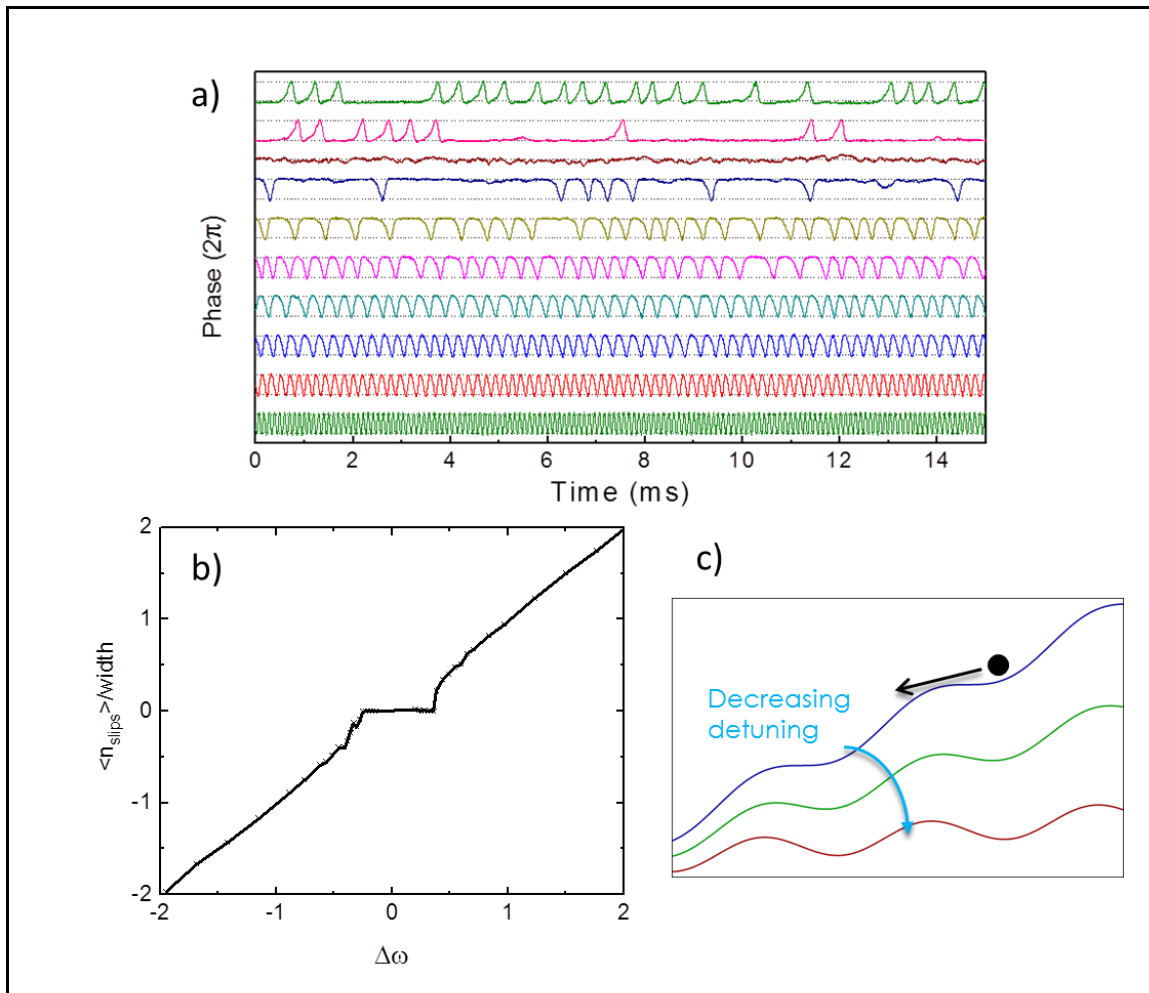
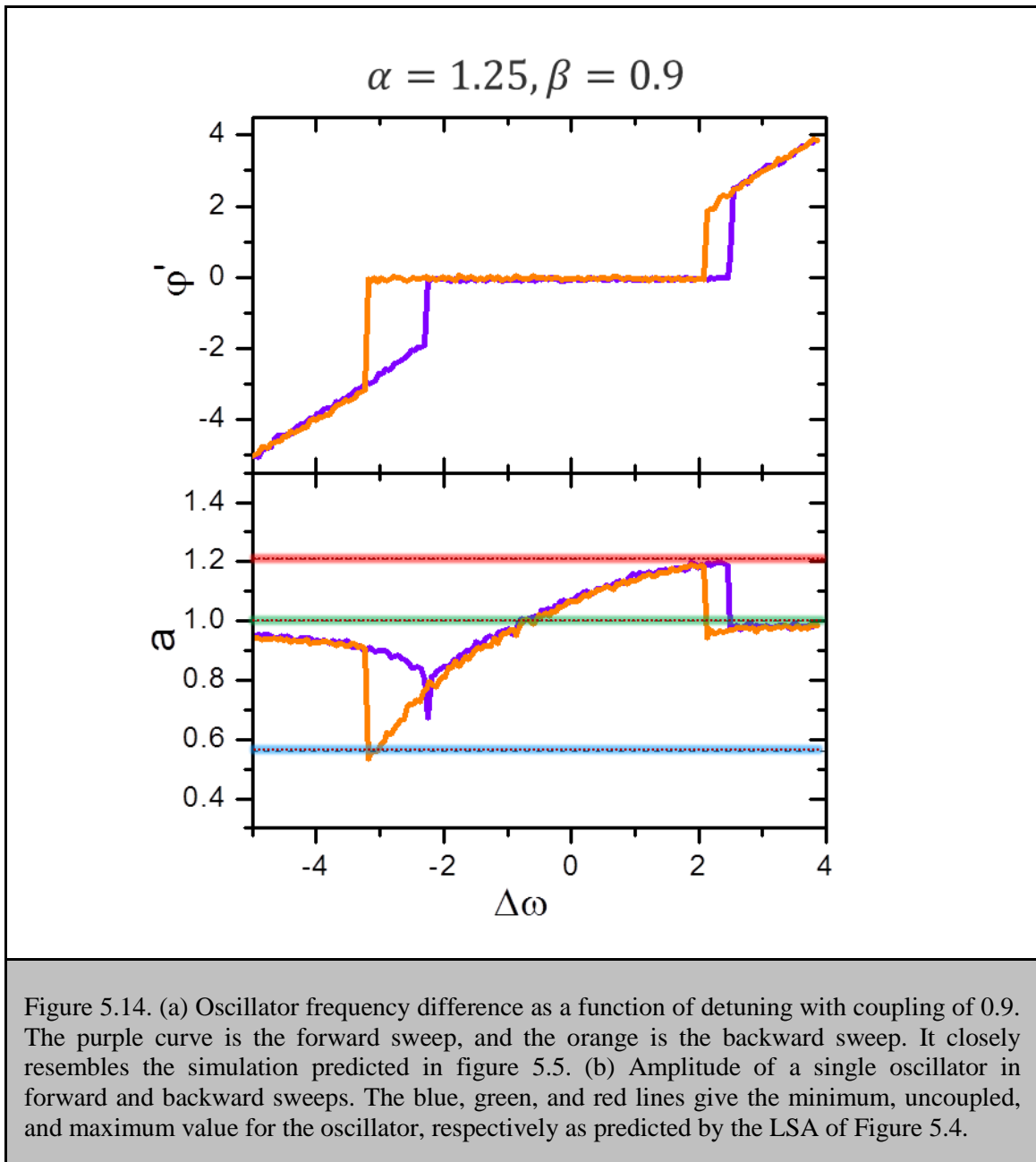


Figure 5.13. (a) Phase slips as a function of time with $\beta = 0.068$ and $\alpha = 1.25$ as before in Figure 5.11. Going up the curves shows the detuning decreasing until aperiodic jumps are seen, after which phase locking is observed (dark red, third line from top). At more negative detuning, the jumps continue with opposite polarity. (b) Curve traced using phase slip data by averaging the number of slips in time and dividing by the open loop spectral resonator width. The overall curve matches well with the Adler prediction in 5.11. (c) Diagram of the system on the washboard potential given by equation (5.29).

5.12 Frequency Sweeps at Larger Coupling

As we increase the coupling, hysteresis sets in (as in the simulation shown in Figure 5.6). In Figure 5.14, we show a frequency sweep at a coupling value of $\beta = 0.9$. The top panel shows the oscillator frequency difference, and the bottom panel shows the amplitude of one of the oscillators in forward and backward sweeps. The red, green, and blue lines represent the values of amplitude $a = 1.21, 1,$ and 0.56 , respectively. As discussed in section 5.4, the LSA (Figure 5.4) predicts that the synchronized oscillators are limited to amplitudes between 0.56 and 1.21 . At these values of amplitude, if the magnitude of detuning increases, no more amplitude difference is available to assist the coupling mechanism (either shear-induced or direct) to stay frequency locked.



Next, we show (Figure 5.15) the synchronization regions as a function of the detuning and coupling parameters $\Delta\omega, \beta$ with a fixed value of shear $\alpha = 1.25$, for both “attractive” and “repulsive” coupling. The data is found by sweeping the detuning forward and backward and recording where the frequency difference is less than 0.1. The blue areas are regions in parameter

space where the oscillators are synchronized for both backwards and forwards sweeps. The green are regions of synchronization going backwards (toward negative detuning), and the red are regions of synchronization going forwards (toward positive detuning). The orange lines are the overlay of experimental data for synchronized states with $\alpha = 0.1$ (low shear). Thus, we can see that nonisochronicity increases the size of the synchronization region. The synchronization region for attractive coupling is smaller than the region for repulsive coupling as predicted by equation (5.13) due to a competition between the direct coupling effect, and the shear induced coupling. Also note that in low coupling ($\beta < 0.25$), there is essentially no hysteresis (red and green regions shrink to zero), and the synchronization region grows linearly with coupling, as predicted by the Adler approximation. The growth of the synchronization region becomes nonlinear in coupling for large $|\beta|$ due to the fact that amplitude differences we described in equation (5.26).

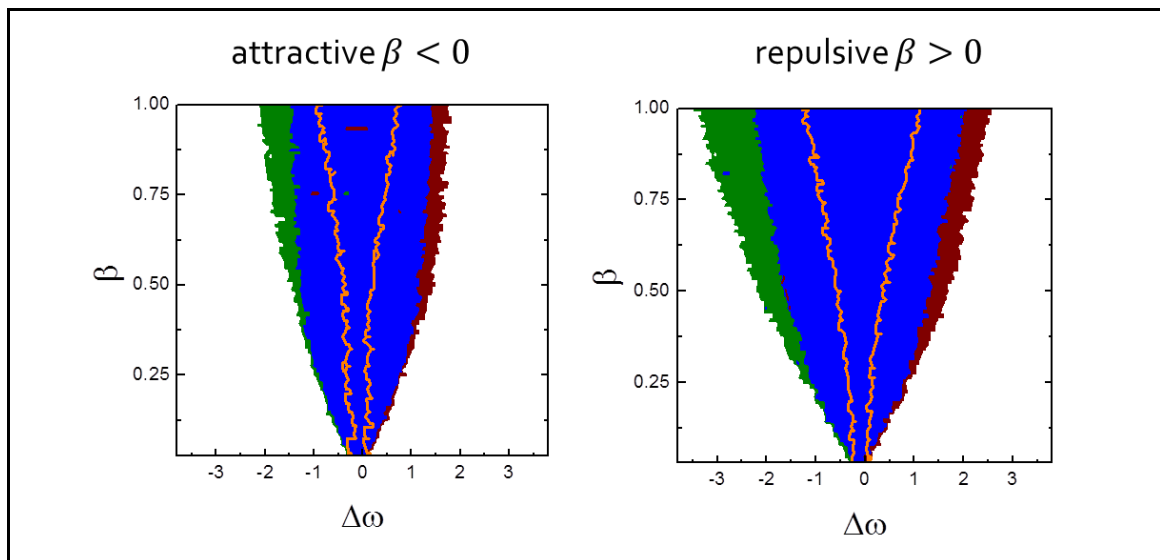
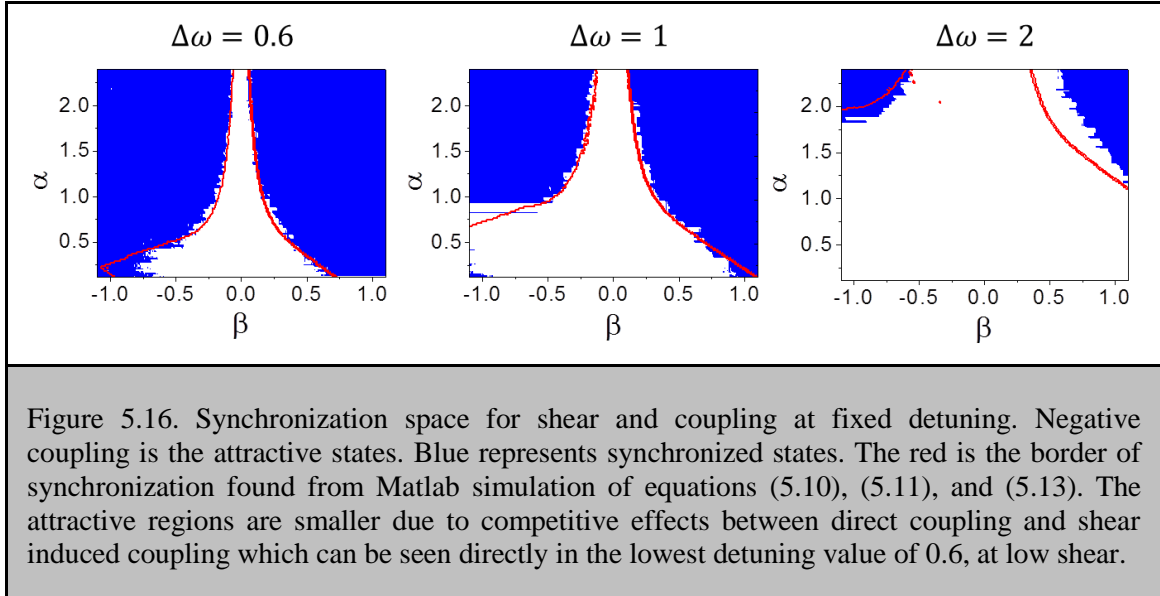


Figure 5.15. Synchronization region for shear 1.25. The white is unsynchronized states. The green is synchronized only in reverse sweeps. The red is synchronized only in forward sweeps. The blue is synchronized in both. The orange line shows the border of the synchronization region at a shear of 0.1. The influence of shear to increase the synchronization region is clear. Also, the attractive region is smaller due to competition between direct coupling and shear induced coupling. The criterion for synchronization was taken to be a frequency difference of less than 0.1: this causes inaccuracy in the size of the region at low coupling. The sizes of the green and red regions are different due to a difference in quality factor and oscillator amplitude.

5.13 Synchronized States at Fixed Detuning

We proceed to show (Figure 5.16) the regions of synchronized states in the $\alpha - \beta$ plane at fixed detuning. In order to do this, we sweep the coupling and step the shear, and correct for frequency drifts between steps by piezoelectrically tuning one of the resonators. This can only be done if the shear of the two oscillators is very similar so that as the saturation is changed, there is no ‘extra’ detuning creeping in due to differing shears. These data are taken from low magnitudes of coupling to higher magnitudes of coupling. Hysteresis appears if we include sweeps from high magnitudes to low magnitudes, but is not presented here. We treat the case of attractive coupling as negative values of the parameter β . The blue regions are regions where the oscillators are synchronized, and the white are unsynchronized states. The red lines are boundaries for the synchronized regions found from simulations of equations (5.10), (5.11), and (5.13) run in Matlab. We see excellent agreement between simulation and experiment at lower values of detuning. At higher values, there is a larger disagreement probably due to the slight differences in quality factor and amplitude that breaks the symmetry of the hysteresis in the data of detuning sweeps (Figure 5.6). At the lowest detuning $\Delta\omega = 0.6$, the simulations predict a ‘kink’ in the boundary of the synchronized region at values of negative coupling. This shows up in the data as

well. This is where the direct coupling term in equation (5.13) crosses the shear induced coupling term.



5.14 Phase Noise in Two Synchronized Oscillators

Finally, we look at the phase noise in synchronized oscillators. First, we start with equation (5.8) and (5.9) and add noise terms

$$\varphi'_1 = \frac{\delta_1}{2} + \alpha a_1^2 + \frac{a_2 \beta}{a_1} \frac{\cos \varphi}{2} + \Xi_1, \quad (5.30)$$

and

$$\varphi'_2 = \frac{\delta_2}{2} + \alpha a_2^2 + \frac{a_1 \beta}{a_2} \frac{\cos \varphi}{2} + \Xi_2, \quad (5.31)$$

where the noise terms Ξ_i are assumed to be uncorrelated white noise. This gives equations in the limit of small coupling,

$$\varphi'_1 = \frac{\delta_1}{2} + \alpha(1 + 2\beta \sin\varphi) + \Xi_1, \quad (5.32)$$

and

$$\varphi'_2 = \frac{\delta_2}{2} + \alpha(1 - 2\beta \sin\varphi) + \Xi_2, \quad (5.33)$$

where the approximate amplitude changes have been made as before. The difference of phases will give the Adler equation (5.16) with noise.

However, since the sum of the phases yields

$$\frac{\psi'}{2} = \frac{\delta_1}{4} + \frac{\delta_2}{4} + \alpha + \frac{\Xi_1 + \Xi_2}{2}. \quad (5.34)$$

We can compare the noise induced perturbations of this quantity (noting that it is equivalent to the perturbations of a single oscillator when there is a phase locked solution, $\varphi' = 0$),

$$\delta \frac{\psi'}{2} = \delta \varphi'_{i,s} = \frac{\Xi_1 + \Xi_2}{2}, \quad (5.35)$$

to the perturbations from equations (5.32) and (5.33) for unsynchronized oscillators,

$$\delta \varphi'_{i,u} = \Xi_i. \quad (5.36)$$

The variance of equation (5.35) is given by

$$\langle (\delta\varphi'_{i,s})^2 \rangle = \left\langle \left(\frac{\Xi_1 + \Xi_2}{2} \right)^2 \right\rangle = \frac{\langle \Xi_1^2 \rangle + \langle \Xi_2^2 \rangle}{4}, \quad (5.37)$$

with the last equality true only when the two noise terms are uncorrelated. If the noise terms have equal intensity we can drop the subscript

$$\langle (\delta\varphi'_{i,s})^2 \rangle = \frac{\langle \Xi^2 \rangle}{2} = \frac{\langle (\delta\varphi'_{i,u})^2 \rangle}{2}. \quad (5.38)$$

This phenomenon can be understood another way if we look at the total phase diffusion mapped onto the torus, where the outer ring radius describes the phase difference, and the tube radius describes the sum phase. In Figure 5.17, we show a random walk of both oscillators as a single variable on this torus. Figure 5.17 (a) shows an unsynchronized walk, while Figure 5.17 (b) shows the walk when synchronized. Essentially, the noise decreases since the diffusion is constrained to one dimension, and the random walk of both oscillators decreases due to a single diffusion variable.

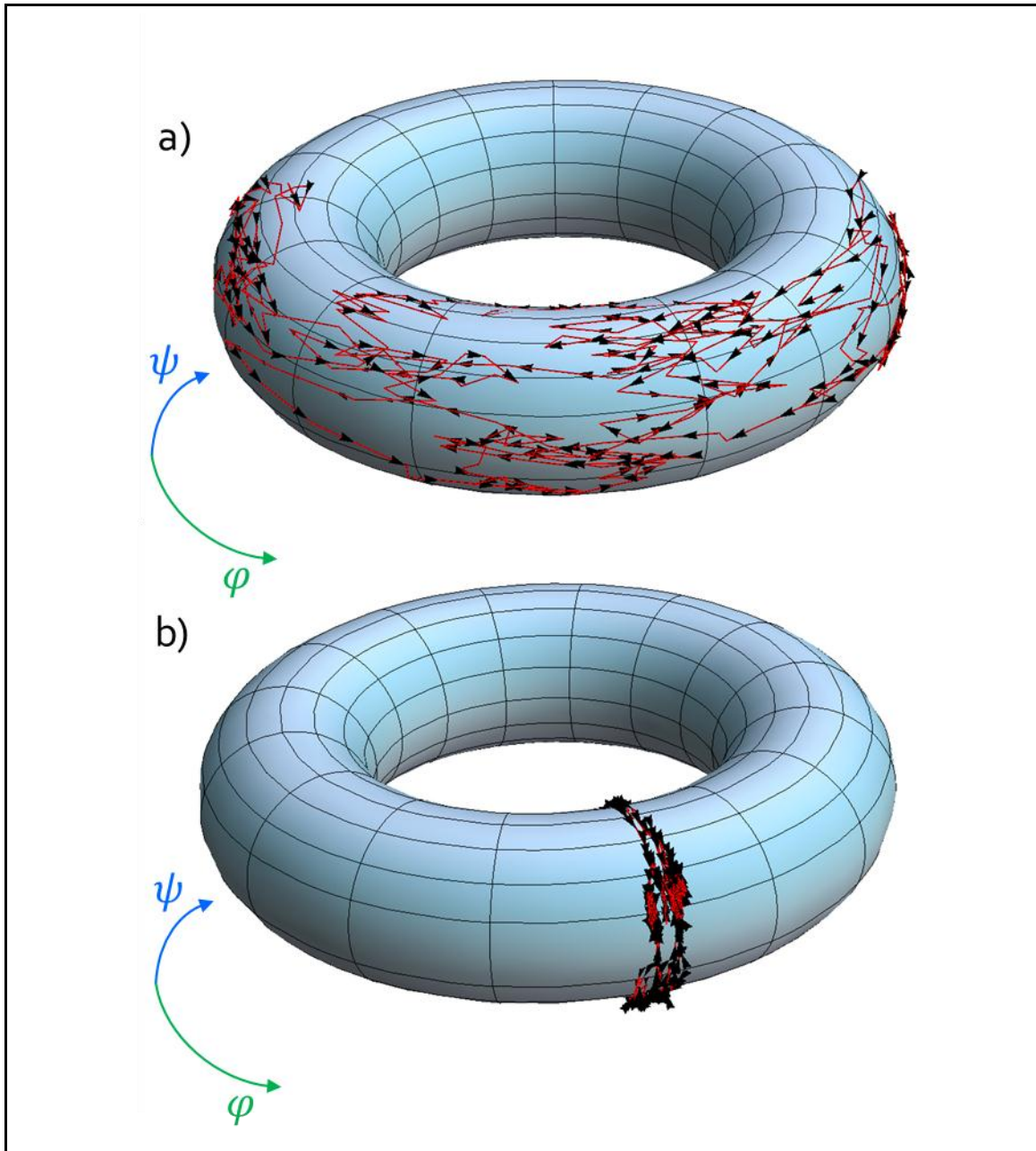
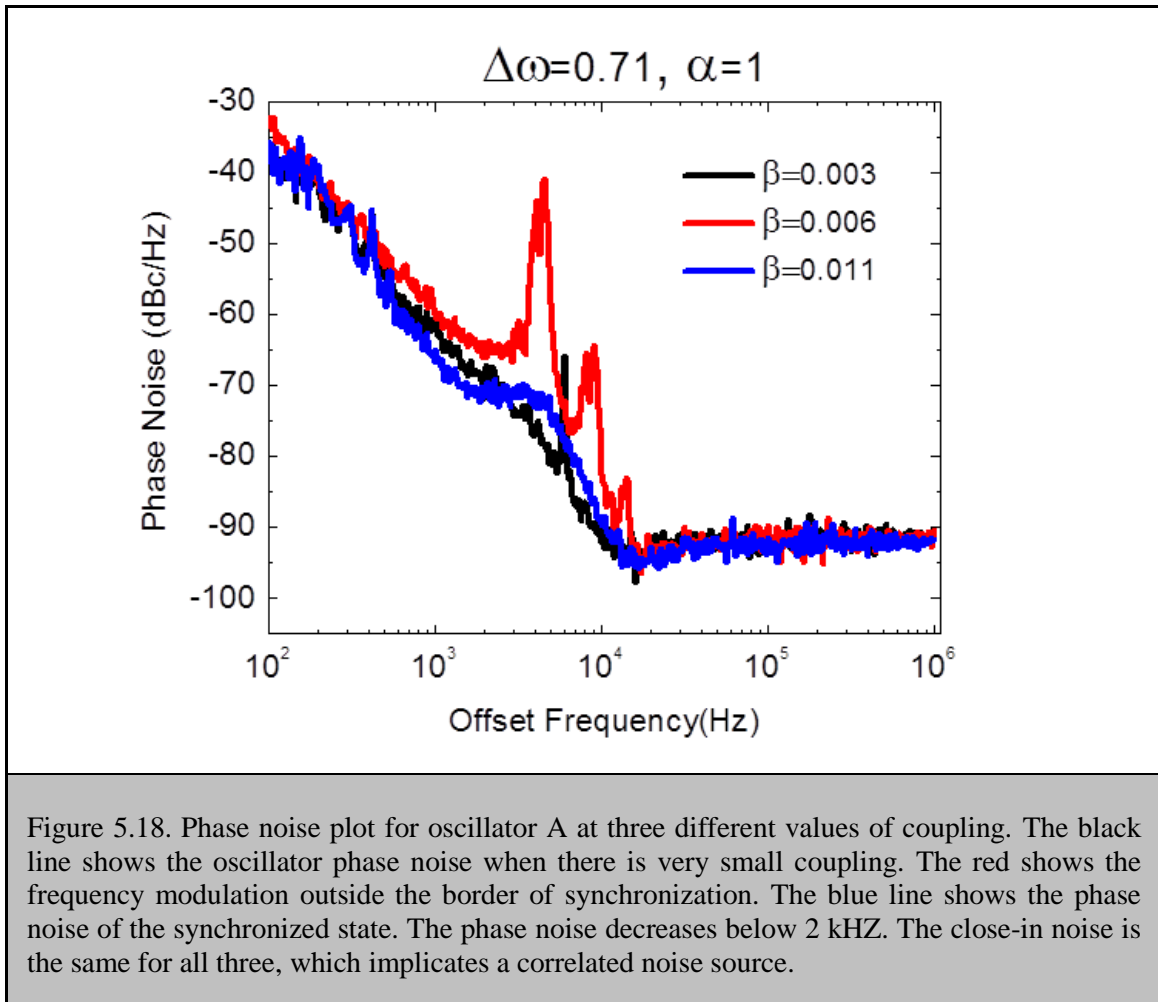


Figure 5.17. Topology for the phase variables of the two oscillators. Tube angle is the sum phase, ψ , and ring angle is difference phase, ϕ . The red path represents the oscillator sum and difference phase in the rotating frame (rotating in both). When the oscillators are unsynchronized (a) the phase diffuses in both phase dimensions. When synchronized (b) the oscillator only diffuses in the sum phase dimension, reducing the dimension of the random walk.

Experimentally, we can explore this phenomenon by measuring the phase noise of each oscillator as we change coupling. The data is taken using a phase noise module in the spectrum analyzer. This phase noise measurement system has been validated using known frequency sources. In Figure 5.18, we show phase noise for the oscillator at three different couplings.



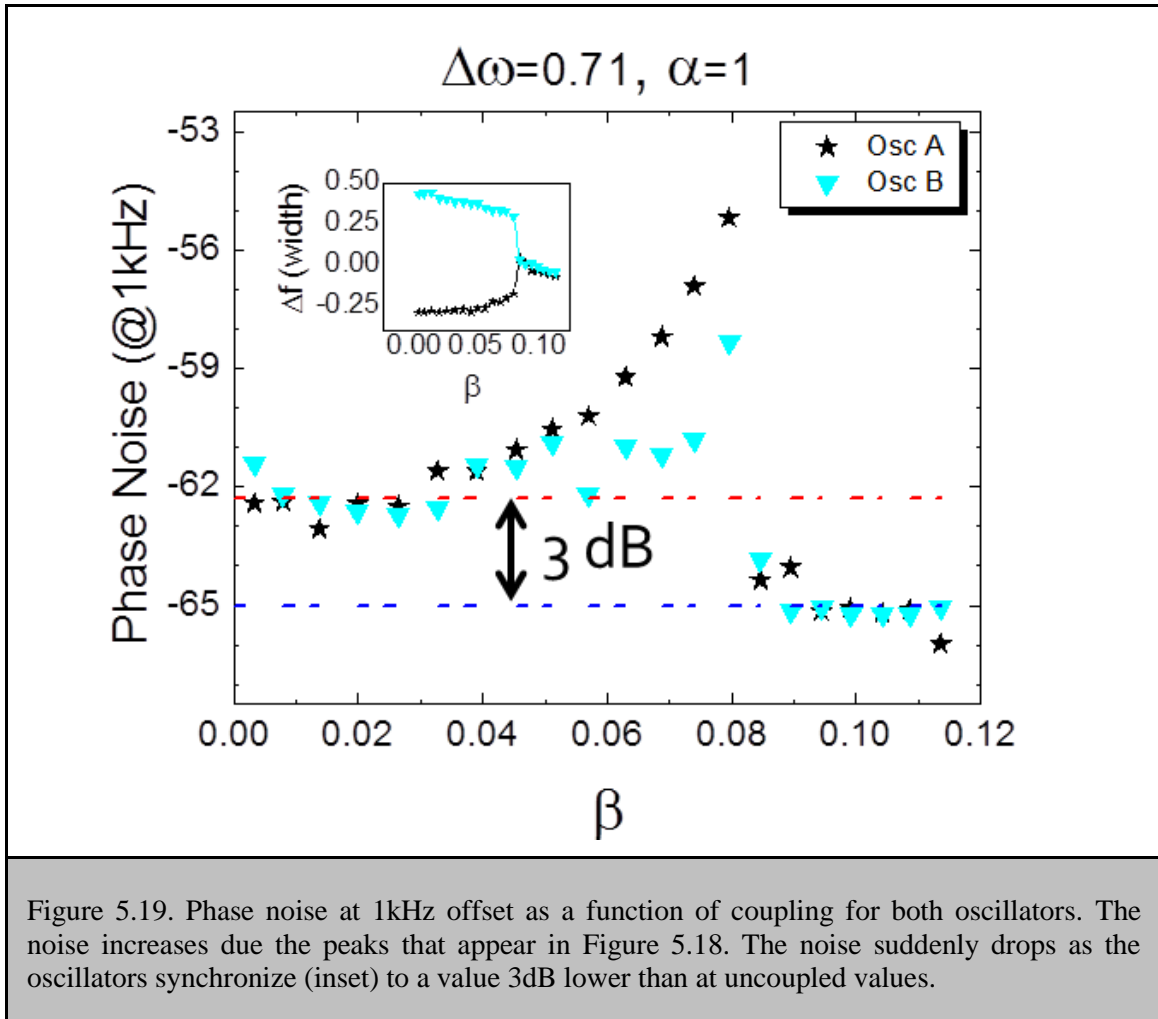
The highest coupling (blue line) is when the oscillators are locked and shows a reduced phase noise for offset frequencies smaller than 2 kHz. The 2 kHz limit is possibly due to the loop bandwidth. In order to see the effects of synchronization on the phase noise we chose an offset of

1kHz, which is a region where the phase noise is significantly reduced. Also, phase noise at 1kHz offset is a key figure of merit in MEMS oscillators[27].

Note that the phase noise increases when approaching the synchronization regime due to the appearance of the peaks in Figure 5.18 (red line). These peaks are a signature of frequency modulation caused by interaction between the two oscillators (as noted by reference [7]).

There does not seem to be a difference in phase noise below 500 Hz offset between the synchronized and unsynchronized states, which would be consistent with correlated noise sources between the two oscillators. Recall that equation (5.38) depends on uncorrelated sources of noise, so that the variance of phase for the sum of the two oscillators could be separated into the variances coming from the two noise sources. To account for correlated noise, cross-terms would have to be included in equation (5.38).

We plot the noise at 1kHz as a function of coupling in Figure 5.19 with $\Delta\omega = 0.71$ and $\alpha = 1$. The noise starts off at -62dB for both oscillators and initially increases with the coupling, before suddenly jumping to a value of -65dB , indicating a 3dB noise improvement, or about a 2x decrease in phase noise intensity, as indicated by equation (5.35). The inset shows the frequencies of the two oscillators as a function of the coupling parameter. The synchronization occurs at $\beta \cong 0.08$ according to the frequency difference data.



5.15 Future Work

This work explored the simplest case of synchronization between reactively coupled nonisochronous oscillators. Obviously, more complex systems can be imagined with large arrays of feedback oscillators. By coupling them through a local mechanism (e.g., through the substrate), 1-dimensional arrays with either a nearest neighbor interaction or a power law interaction are possible. This type of coupling could also be used to make 2-dimensional arrays with different configurations of coupling, depending on how many connections are made to nearest neighbors.

If coupling through feedback loops, then arrays of arbitrary dimension can be constructed. Rich dynamics can be explored in these arrays.

To construct oscillator arrays that are modeled by reference [28], a feedback loop is required for each NEMS resonator. This would require integration between NEMS and CMOS for large arrays. NEMS-CMOS integration has been demonstrated [29], clearing the way for implementing coupled NEMS arrays with CMOS circuitry.

There are obvious applications for making frequency sources out of synchronized oscillator arrays. Here, we used the shear to help synchronize two oscillators. However, we know from chapter 4 that, in general, nonzero shear increases phase noise. Therefore, when making frequency sources from synchronized oscillator arrays, the shear must be kept to a minimum so that the phase noise (arising from AM-PM conversion) for each oscillator is likewise kept to a minimum.

Finally, NEMS oscillator arrays could improve the performance of sensing technology. In the study by Li, et. al. [30], chemical vapors were detected using NEMS resonators with an accuracy of ~ 0.6 ppb. If, instead of one resonator embedded in a phase locked loop, many resonators embedded in an oscillator array are used, then phase noise would decrease for uncorrelated noise sources by the number of oscillators (as indicated by equation (5.38)). If equal parts of a chemical vapor are absorbed into each resonator in an oscillator array, then the single array frequency would shift by the same amount as the single device. Hence, with lower phase noise (leading to lower frequency noise), and the same frequency shift (being our signal of interest), then the overall signal-to-noise ratio for the gas absorption would improve by the number of oscillators used in the array.

Bibliography

1. S.H. Strogatz, *Sync : the emerging science of spontaneous order*. 1st ed. 2003, New York: Hyperion. viii, 338 p.
2. ***Complex dynamics and phase synchronization in spatially extended ecological systems***
B. Blasius, A. Huppert and L. Stone
Nature, 1999, 399(6734), 354-359.
3. ***A Self-Organized Vortex Array of Hydrodynamically Entrained Sperm Cells***
I.H. Riedel
Science, 2005, 309(5732), 300-303.
4. ***Model of Transient Oscillatory Synchronization in the Locust Antennal Lobe***
M. Bazhenov, M. Stopfer, M. Rabinovich, R. Huerta, H.D.I. Abarbanel, T.J. Sejnowski and G. Laurent
Neuron, 2001, 30(2), 553-567.
5. ***Synchronization Transitions in a Disordered Josephson Series Array***
K. Wiesenfeld, P. Colet and S.H. Strogatz
Physical Review Letters, 1996, 76(3), 404-407.
6. Y. Kuramoto, *Chemical oscillations, waves, and turbulence*. Dover ed. 2003, Mineola, N.Y.: Dover Publications. vi, 156 p.
7. A. Pikovsky, M. Rosenblum and J. Kurths, *Synchronization : a universal concept in nonlinear sciences*. The Cambridge nonlinear science series. 2001, Cambridge: Cambridge University Press. xix, 411 p.
8. ***Generation Linewidth of an Auto-Oscillator with a Nonlinear Frequency Shift: Spin-Torque Nano-Oscillator***
J.-V. Kim, V. Tiberkevich and A. Slavin
Physical Review Letters, 2008, 100(1).
9. ***Mutual phase-locking of microwave spin torque nano-oscillators***
S. Kaka, M.R. Pufall, W.H. Rippard, T.J. Silva, S.E. Russek and J.A. Katine
Nature, 2005, 437(7057), 389-392.
10. ***Phase-locking of magnetic vortices mediated by antivortices***
RuotoloA, CrosV, GeorgesB, DussauxA, GrollierJ, DeranlotC, GuillemetR, BouzheouaneK, FusilS and FertA
Nat Nano, 2009, 4(8), 528-532.
11. ***Microwave sources: Spin-torque oscillators get in phase***
A. Slavin
Nat Nano, 2009, 4(8), 479-480.

12. R. Lifshitz and M.C. Cross, *Nonlinear Dynamics of Nanomechanical and Micromechanical Resonators*. Reviews of Nonlinear Dynamics and Complexity. 2009: Wiley-VCH Verlag GmbH & Co. KGaA. 1-52.
13. *A self-sustaining ultrahigh-frequency nanoelectromechanical oscillator*
X.L. Feng, C.J. White, A. Hajimiri and M.L. Roukes
Nature Nanotechnology, 2008, **3(6)**, 342-346.
14. R. Karabalin, *Nonlinear, coupled, and parametric nanoelectromechanical systems*. 2008, California Institute of Technology.
15. *Efficient and Sensitive Capacitive Readout of Nanomechanical Resonator Arrays*
P.A. Truitt, J.B. Hertzberg, C.C. Huang, K.L. Ekinici and K.C. Schwab
Nano Letters, 2006, **7(1)**, 120-126.
16. *Tuning nonlinearity, dynamic range, and frequency of nanomechanical resonators*
I. Kozinsky, H.W.C. Postma, I. Bargatin and M.L. Roukes
Applied Physics Letters, 2006, **88(25)**, 253101.
17. *Efficient electrothermal actuation of multiple modes of high-frequency nanoelectromechanical resonators*
I. Bargatin
Applied Physics Letters, 2007, **90(9)**, 093116.
18. *Multifunctional Nanomechanical Systems via Tunably Coupled Piezoelectric Actuation*
S.C. Masmanidis, R.B. Karabalin, I. De Vlaminck, G. Borghs, M.R. Freeman and M.L. Roukes
Science, 2007, **317(5839)**, 780-783.
19. *A Nanoscale Parametric Feedback Oscillator*
L.G. Villanueva, R.B. Karabalin, M.H. Matheny, E. Kenig, M.C. Cross and M.L. Roukes
Nano Letters, 2011, **11(11)**, 5054-5059.
20. S.T. Thornton and J.B. Marion, *Classical dynamics of particles and systems*. 5th ed. 2004, Belmont, CA: Brooks/Cole. xvi, 656 p.
21. *Nonlinear dynamics and chaos in two coupled nanomechanical resonators*
R.B. Karabalin, M.C. Cross and M.L. Roukes
Physical Review B, 2009, **79(16)**, 165309.
22. *Synchronization by nonlinear frequency pulling*
M.C. Cross, A. Zumdieck, R. Lifshitz and J.L. Rogers
Physical Review Letters, 2004, **93(22)**, -.
23. M. Grau, *Theory and Numerics of Two Synchronized Oscillators*, in *Physics*. 2009, California Institute of Technology: Pasadena. p. 27.
24. *A Study of Locking Phenomena in Oscillators*
R. Adler
Proceedings of the IRE, 1946, **34(6)**, 351-357.

25. S.H. Strogatz, *Nonlinear dynamics and Chaos : with applications to physics, biology, chemistry, and engineering*. Studies in nonlinearity. 1994, Reading, Mass.: Addison-Wesley Pub. xi, 498 p.
26. ***Signal Amplification by Sensitive Control of Bifurcation Topology***
R.B. Karabalin, R. Lifshitz, M.C. Cross, M.H. Matheny, S.C. Masmanidis and M.L. Roukes
Physical Review Letters, 2011, 106(9), 094102.
27. ***A review of MEMS oscillators for frequency reference and timing applications***
J.T.M.v. Beek and R. Puers
Journal of Micromechanics and Microengineering, 2012, 22(1), 013001.
28. ***Synchronization by reactive coupling and nonlinear frequency pulling***
M.C. Cross, R. Lifshitz and A. Zumdieck
Physical Review E, 2006, 73(3).
29. ***A Compact and Low-Power CMOS Circuit for Fully Integrated NEMS Resonators***
J. Arcamone, B. Misischi, F. Serra-Graells, M.A.F. van den Boogaart, J. Brugger, F. Torres, G. Abadal, N. Barniol and F. Perez-Murano
Circuits and Systems II: Express Briefs, IEEE Transactions on, 2007, 54(5), 377-381.
30. ***Nanoelectromechanical Resonator Arrays for Ultrafast, Gas-Phase Chromatographic Chemical Analysis***
M. Li, E.B. Myers, H.X. Tang, S.J. Aldridge, H.C. McCaig, J.J. Whiting, R.J. Simonson, N.S. Lewis and M.L. Roukes
Nano Letters, 2010, 10(10), 3899-3903.

Appendix I -

Secular Perturbation Theory

We begin using a typical example of secular perturbation theory and explain the method as we go along. We begin with the equation of motion for a simple damped spring-mass system with nonlinear spring stiffness and nonlinear damping. We will assume symmetry in the displacement, i.e. that the spring potential is an even function of the displacement. We will also assume symmetry in the damping so that the equation of motion for this system becomes

$$m\ddot{x} = F_{con}(x, x^3, x^5, \dots) - \gamma_1\dot{x} - \gamma_3x^2\dot{x}, \quad (\text{A-I.1})$$

where all the intrinsic forces in the system to the conservative forces have been lumped together. For now, it is easier to assume the first order corrections to the linear problem

$$m\ddot{x} = -k_1x - k_3x^3 - \gamma_1\dot{x} - \gamma_3x^2\dot{x}, \quad (\text{A-I.2})$$

with the stiffness coefficients k_n , and damping coefficients γ_n . At this point, the only stable fixed point for this system is at zero displacement and velocity, so we add a gain term to the system,

$$\ddot{x} + \omega_m^2 (1 + \tilde{\delta}) x + \tilde{\alpha} x^3 + Q^{-1} \omega_m \dot{x} + \tilde{\eta} x^2 \dot{x} = \frac{\tilde{g}}{m} \dot{x}, \quad (\text{A-I.3})$$

where we have divided through by the mass in order to put the equation in terms of the acceleration. We represent the resonant frequency of the device as slightly offset from another ‘close’ frequency. Although this seems awkward to introduce this other frequency, it helps to put multiple oscillations in separate resonators on the same timescale. Note that this is the van der Pol equation and that the quality factor has been substituted for the linear damping as this is the quantity usually measured. To make the equation easier to understand, we typically scale out the frequency by setting $\tilde{t} = \omega_m t$ and then return to the original notation which gives

$$\omega_m^2 \ddot{x} + \omega_m^2 (1 + \tilde{\delta}) x + \tilde{\alpha} x^3 + \left(Q^{-1} \omega_m^2 - \frac{\tilde{g} \omega_m}{m} \right) \dot{x} + \omega_m \tilde{\eta} x^2 \dot{x} = 0. \quad (\text{A-I.4})$$

Now at this point, the particular scaling used for the amplitude is up to preference. For the driven Duffing system presented here, the frequency is divided out, and the other coefficients are renormalized

$$\ddot{x} + (1 + \tilde{\delta}) x + \tilde{\alpha} x^3 - \tilde{g} \dot{x} + \tilde{\eta} x^2 \dot{x} = 0. \quad (\text{A-I.5})$$

In order to solve this equation we proceed to use secular perturbation theory.

The procedure starts with making the assumption that there exists multiple timescales. For weakly nonlinear systems two timescales are assumed: one for the motion of the spring mass system’s instantaneous displacement and velocity, and one for the slow change of the overall

amplitude of the system. For weakly nonlinear systems, the steady state dynamics occurs at the slow timescale. We quantify this by stating

$$x(t) = \epsilon^{\frac{1}{2}}x_0(t) + \epsilon^{\frac{3}{2}}x_1(t) + \epsilon^{\frac{5}{2}}x_2(t) + \dots = \frac{1}{2}\epsilon^{\frac{1}{2}}(\tilde{A}(T)e^{-it} + c.c.) + \epsilon^{\frac{3}{2}}x_1(t) + \dots, \quad (\text{A-I.6})$$

$$T = \epsilon t,$$

where ϵ is a small number, and \tilde{A} is in general complex. Also, since the nonlinear terms are small, and the quality factor is typically larger than 1000 for NEMS, we let this small number be the inverse quality factor. We note that the frequency shift δ is on the order of the quality factor. Thus the EOM becomes

$$\ddot{x} + (1 + \epsilon\bar{\delta})x + \tilde{\alpha}x^3 - \epsilon\bar{g}\dot{x} + \tilde{\eta}x^2\dot{x} = 0. \quad (\text{A-I.7})$$

The derivatives of equation I.6 are

$$\dot{x}(t) = \frac{\epsilon^{\frac{1}{2}}}{2}([\epsilon\tilde{A}' - i\tilde{A}]e^{-it} + c.c.) + \epsilon^{\frac{3}{2}}\dot{x}_1(t) + \mathcal{O}\left(\epsilon^{\frac{5}{2}}\right), \quad (\text{A-I.8})$$

and

$$\ddot{x}(t) = \frac{\epsilon^{\frac{1}{2}}}{2}([\epsilon^2\tilde{A}'' - 2\epsilon i\tilde{A}' - \tilde{A}]e^{-it} + c.c.) + \epsilon^{\frac{3}{2}}\ddot{x}_1(t) + \mathcal{O}\left(\epsilon^{\frac{5}{2}}\right). \quad (\text{A-I.9})$$

Thus, using these derivatives and writing out equation I.7, we get

$$\begin{aligned}
& \frac{\epsilon^{\frac{1}{2}}}{2} \left([\epsilon^2 \tilde{A}'' - 2\epsilon i \tilde{A}' - \tilde{A}] e^{-it} + c.c. \right) + \epsilon^{\frac{3}{2}} \dot{x}_1(t) \\
& + (1 + \epsilon \bar{\delta}) \left(\frac{\epsilon^{\frac{1}{2}}}{2} (\tilde{A} e^{-it} + c.c.) + \epsilon^{\frac{3}{2}} x_1(t) \right) \\
& + \frac{\epsilon^{\frac{3}{2}}}{8} \tilde{\alpha} \left(\tilde{A}^3 e^{-3it} + 3|\tilde{A}|^2 \tilde{A} e^{-it} + c.c. \right) \\
& + \frac{\epsilon^{\frac{3}{2}}}{2} \tilde{g} \left([\epsilon \tilde{A}' - i \tilde{A}] e^{-it} + c.c. \right) \\
& + \frac{\epsilon^{\frac{3}{2}}}{8} \tilde{\eta} \left((\epsilon \tilde{A}^2 \tilde{A}' - i \tilde{A}^3) e^{-3it} + i |\tilde{A}|^2 \tilde{A} e^{-it} + c.c. \right) \\
& + \mathcal{O}\left(\epsilon^{\frac{5}{2}}\right).
\end{aligned} \tag{A-I.10}$$

Collecting in powers of ϵ we get,

$$\epsilon^{1/2}: \quad \ddot{x}_0(t) + x_0(t) = \frac{1}{2} (-\tilde{A} + \tilde{A}) e^{-it} + c.c., \tag{A-I.11}$$

$$\begin{aligned}
\epsilon^{\frac{3}{2}}: \quad \ddot{x}_1(t) + x_1(t) &= \left(\left(i\tilde{A}' + \frac{\delta\tilde{A}}{2} + \frac{3\tilde{\alpha}}{8} |\tilde{A}|^2 \tilde{A} - i\frac{\tilde{g}}{2} \tilde{A} + i\frac{\tilde{\eta}}{8} |\tilde{A}|^2 \tilde{A} \right) e^{-it} \right. \\
&\quad \left. + (\dots)e^{-3it} \right) + c.c.. \tag{A-I.12}
\end{aligned}$$

⋮

Now, the terms proportional to e^{-it} are called the *secular* terms. These terms must be null, otherwise this first order perturbation would diverge at long times (and thus not be a periodic solution for the l.h.s.). This is trivial to see for the zeroth order solution. For the first order solution this gives the so-called *amplitude equation*

$$A' - i(\delta + \alpha|A|^2)A + g(1 - |A|^2)A = 0, \quad A = \sqrt{\eta}\tilde{A}, \tag{A-I.13}$$

where we have rescaled the frequency shift, nonlinear stiffness, gain, and amplitude. We can further reduce this equation, by resetting the timescale by the gain or the frequency splitting.

Appendix II -

Fabrication Methods

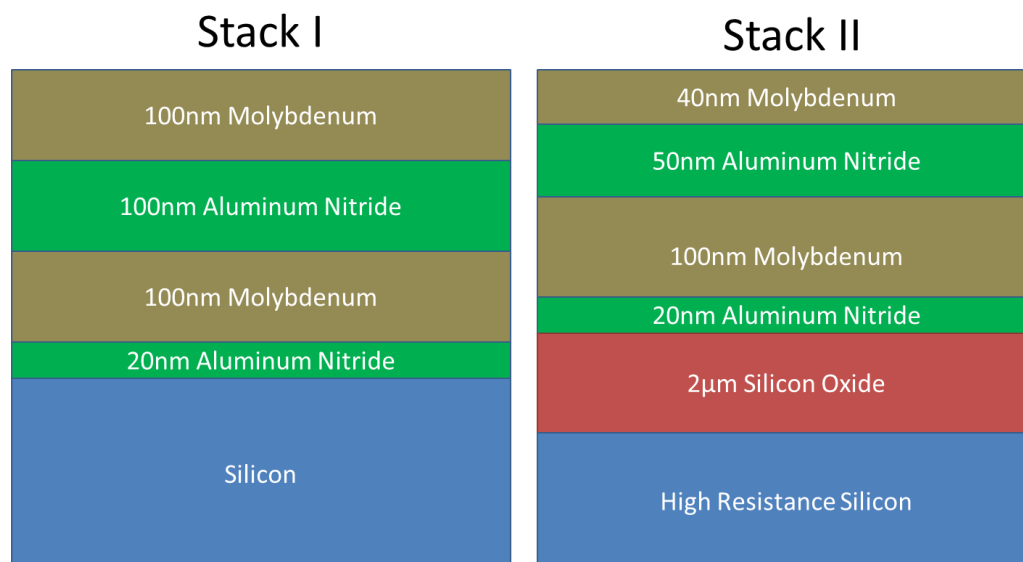
AI.1 Introduction

A key part to this thesis work was the ability to fabricate mechanical devices out of a relatively new material for the group, piezoelectric aluminum nitride (AlN). It turns out that to be able to achieve strong actuation and low feedthrough with all electrical signals, an island of aluminum nitride must be cut out of the bare wafer in order to reduce parasitic capacitance. Also, having all-electrical transduction requires more electrical leads on the die. We make low resistance contacts between the bondpads made from gold and the electrodes of the devices made of molybdenum (Mo).

AI.2 Piezoelectric Wafer Stacks

Two major wafer stacks were explored in this thesis. The first (Stack I) consisted of 100nm Mo/100nm AlN/ 100nm Mo/ 20nm Aluminum Nitride/ Bulk Silicon wafer. The second was made to improve transduction efficiency through offsetting the central AlN layer. This stack

(Stack II) consisted of 40nm Mo/ 50nm AlN/ 100nm Mo/ 20nm AlN/ 2 μ m SiO₂/ High Resistance Silicon wafer.



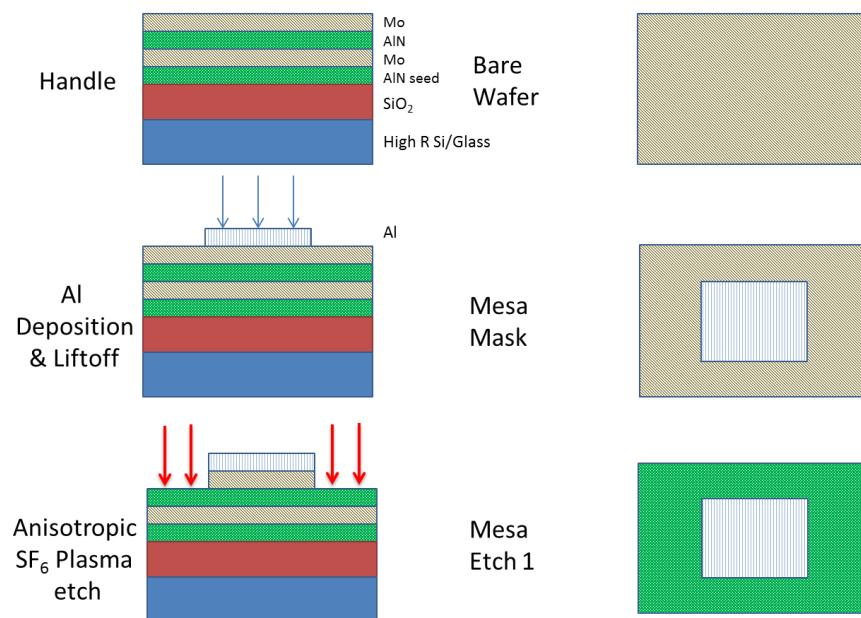
AI.3 Fabrication of Piezoelectric AlN

Developing a fabrication process for aluminum nitride required a more complex fabrication process than is typically found in NEMS. The wafers tested typically have the same primary stacking. First, on thermally grown SiO₂ on Si, a ‘seed’ AlN nitride layer was deposited to properly align crystal orientation in the subsequent layers. This, according to our collaborators, was always necessary to achieve good thin film piezoelectrics. This was not necessarily bad, since offset of both the piezoelectric and piezoresistive layers are crucial for transduction. The seed material also has very high sonic velocity, thus keeping the average sonic velocity for the mechanical structures tested high. Next, a Mo layer was deposited to serve as a ground plane for the piezoelectric AlN layer. Next, the piezoelectric AlN layer is deposited under an applied external field so as to orient the polycrystalline material perpendicular to the wafer.

Finally, a top Mo layer was deposited to serve as a layer to both actuate the piezoelectric material and as a piezoresistive material. There are very few metals that adhere well to AlN, with aluminum, platinum, and molybdenum reported.

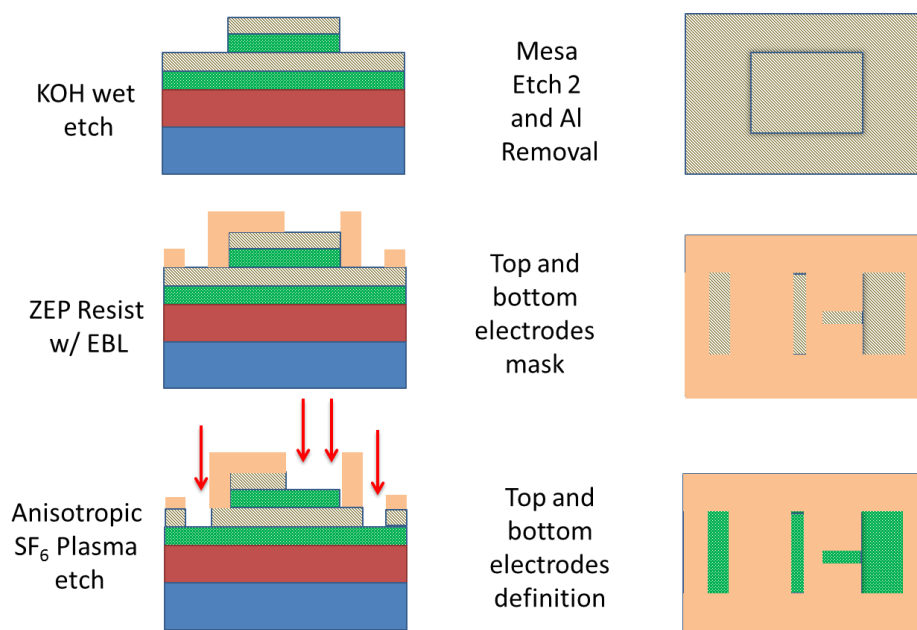
Molybdenum is quite suitable since it has a very large Young's modulus, and serves well as a piezoresistive material. Platinum and aluminum will both work, but aluminum is not that 'orthogonal' in etch processes. In other words, most of the things that etch AlN etch Al as well, with the bare exception that we know of being hydrofluoric acid, which is incompatible with the SiO₂ underneath. Platinum is not easily etched chemically, and is in general frowned upon in industrial processes. Also, platinum has a low sonic velocity. Molybdenum etches well in fluorine plasmas (NF₃, SF₆), but does not etch (or more accurately etches much more slowly than the other materials) in HF and HCl. Note that these fluorine plasmas will etch AlN very slowly, thus serving as effective 'etch stop'.

So the fabrication process is as follows.

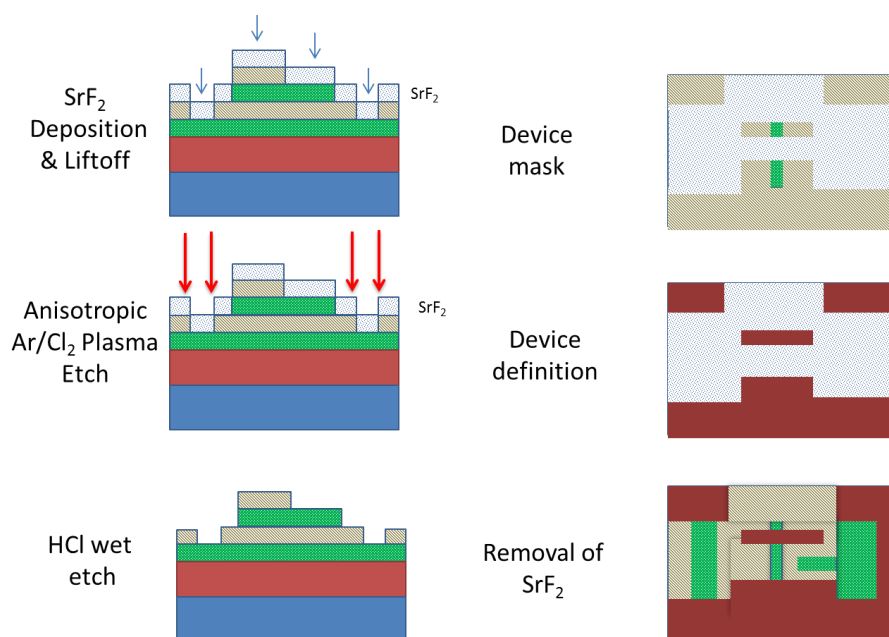


The bare wafer consists, as outline above, of four layers deposited on a thermally grown oxide layer. First, a liftoff process is used to define what we call the *mesa*. The mechanical device will be located in the mesa area, and the bondpads and leads will sit outside the mesa so that parasitic capacitances are significantly reduced. The active piezoelectric layer should be as thin as possible, for both reasons of size and actuation efficiency, which means the capacitance is as very large per unit area. This mesa comes at a cost. We must 'bridge' the leads over the bottom molybdenum layer in order to isolate the top and bottom electrodes, which is outlined later.

Continuing, we next etch the top molybdenum in all areas not inside the mesa using a fluorine plasma. The next step requires removal of the piezoelectric aluminum nitride not inside the mesa, and is done with KOH, which conveniently removes both the Al and AlN. It is seen that the AlN etches anisotropically in the KOH due to the inherent average perpendicular crystal orientation. Next, a ZEP mask is written using EBL to cut away parts of the top and bottom electrodes. The top electrode on the mesa is cut in order to define both the piezoresistive loop and isolate actuation and detection from each other. The Mo is then cut using the same fluorine plasma as before. The bottom electrode is cut in order to isolate different parts of the Mo bottom electrode. It was found that the bondpads stick better with the Mo still underneath, so it is used in conjunction with a thermally evaporated gold layer.



After the ZEP is removed, a SrF_2 layer is deposited using a PMMA bilayer liftoff process. This defines the mechanical device and protects the electrodes from the chlorine plasma of the next step. SrF_2 acts as very good mask for the chlorine plasma etch. Other masks for this step were tried. Hydrogen silsesquioxane (HSQ) was also shown to work in our processes, but did not turn out to be as robust as the SrF_2 mask. HSQ, however, can be removed easily in HF, while residue of SrF_2 remains in all of the wet etch processes found. The HSQ process was therefore much cleaner, and was deposited in the last step. Since weeks could be wasted if the HSQ mask failed, SrF_2 was almost always chosen. The most efficient method for etching AlN anisotropically was found to be an Ar/Cl_2 plasma. KOH, as noted, will also etch it, but unfortunately sidewall profiles are typically rougher when etched with KOH, since crystal grains become apparent. With the chlorine plasma, we can etch both AlN and Mo, which is done to reach the oxide underneath. This removes undesirable parts of the molybdenum bottom layer loitering outside the mesa area.



After the SrF₂ is removed in hydrochloric acid, an isolation layer is deposited covering the bottom electrode so that an electrical lead can step or bridge onto the mesa. The isolation layer used was also SrF₂, since it was the only available insulator easily deposited and not etched in hydrofluoric acid. The bondpads and bridge are deposited simultaneously in order to avoid additionally contact resistance. Finally, with no more masks to be written, the device is suspended using hydrofluoric acid.

